An anisotropic flexural isostasy method for investigating the Martian lithosphere

J. Mussini

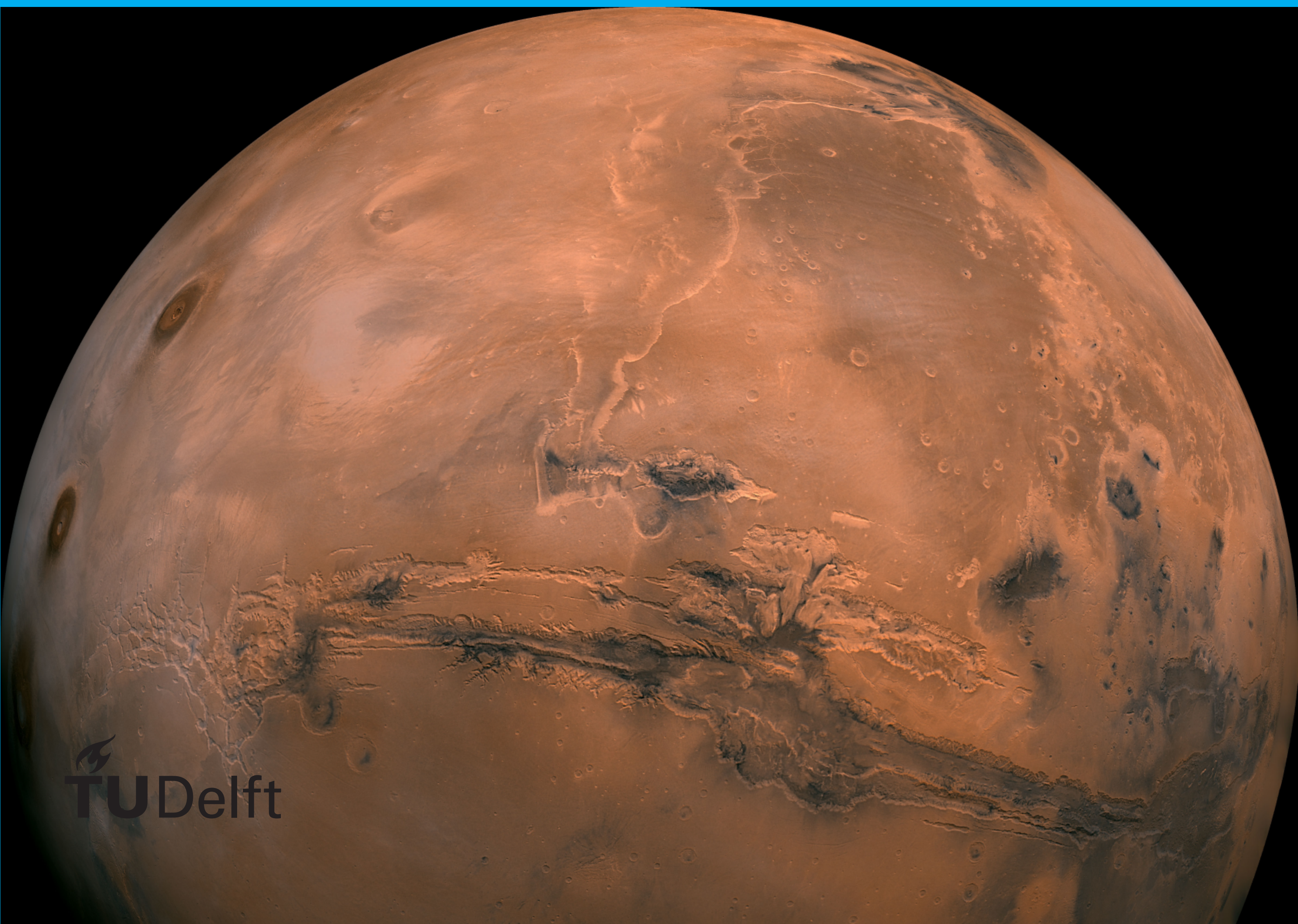

An anisotropic flexural isostasy method for investigating the Martian lithosphere

by

J. Mussini

to obtain the degree of Master of Science
at the Delft University of Technology,
to be defended publicly on Wednesday August 19, 2020 at 10:00 AM.

Student number:	4204875	
Project duration:	May 1, 2019 – August 19, 2020	
Thesis committee:	Dr. ir. B.C. Root,	TU Delft, supervisor
	Dr. ir. W. van der Wal,	TU Delft
	Dr. R. Riva,	TU Delft

TU Delft

Contents

Preface

This document is my MSc thesis graduation project at the faculty of Aerospace Engineering at the Technical University of Delft. I am very grateful to have the opportunity to graduate on a topic in the field of planetary science, and even more so on the planet Mars. This thesis studies new methods of using the topography and gravity of the planet Mars in order to learn more about its subsurface.

This thesis would not have been possible without my supervisor Bart Root, who's dedication to and patience with his students allows us to learn very much in a short amount of time and receive loads of good advice from an experienced researcher in the field we study. I would also like to thank Wouter van der Wal and Riccardo Riva for their time and effort during the defence of this thesis.

Abstract

The subsurface of Mars is impossible to measure directly, yet it has been the subject of many studies. An understanding of the subsurface of Mars would yield large amounts of information on the history of the planet. Two of the tools available to indirectly interact with the Martian subsurface, in particular the lithosphere, are the gravity and topography signals of the planet. These two datasets can be combined using a variety of geological theories in order to investigate the subsurface. In this study, an isostatic model (Airy-type) and two flexural isostatic models (an infinite plate model and a thin shell model) will be the methods of choice. A distinction is made between isotropic or global models, which use one set of physical parameters for the entire planet, and anisotropic or multi-region models which allow for regional variation in physical parameters. The goal of this study is to investigate the performance of the novel thin shell model as compared to the older infinite plate model.

To investigate this, the theory behind each model is explained, after which the models are validated using results from literature. Several regions of interest are defined, mostly among large geological formations or gravity anomalies. Two parameters are chiefly investigated: the average thickness of the lithosphere and the lithospheric elastic thickness, which is a measure of the strength of the lithosphere. Each model is run globally for a variety of these two parameters, and the best fitting parameters are identified. After this, the planet is split into different regions with their own physical parameters. The first study is a dichotomy study which splits the planet into a northern and southern hemisphere, aimed at characterizing the disparity between the Martian north and south. After this, each region is assigned its best fitting physical parameters and the regions are combined into a 'global' regional model. A best fitting multi-region model is obtained via manual observation of the results and adjustment of the inputs until a visual best fit is achieved.

The results are then discussed. A key takeaway is that better methods of judging the performance of models without human visual inspection of their results is necessary in order to realize the full potential of the flexural isostasy models presented in this study. The lack of suitable methods leads to a manifold of best fitting solutions for many of the problems modelled in this study, hindering firm conclusions about the subsurface of Mars. Having said this, global average lithospheric values of about 200 km combined with very low effective lithospheric elastic thickness values of 0 to 40 km are the best fits found in this study. Literature values are typically lower, but this can partially be explained by differences between the flexural isostasy models in this study and the models from literature. Regionally there are large variations, with some features (Hellas basin, Alba mons) being isostatically compensated, others being supported by locally strong lithospheres (much of the Tharsis region), and others resting on buried mass anomalies that cannot be explained with the models in this study (Isidis planitia, Argyre basin). In a dichotomy study, the best fitting values were found for a northern lithosphere zero to ten kilometers thinner than the southern lithosphere. In general, the thin shell model is more sensitive to nonzero lithospheric elastic thickness values, providing very strong lithospheres at low elastic thicknesses. This is due to its aggressive flexural response function's filtering of higher spherical harmonic degree signals. The thin shell models yields higher residuals in the global analyses, but lower residuals in the multi-region studies. At the same time, 80% of the error in all models can be attributed to spherical harmonic degrees between 1 and 10. These signals are likely not caused by flexural isostasy, and require models incorporating more physics (mantle plumes, mass anomalies, etc) to be explained.

1
Introduction

Mars is a terrestrial planet roughly 50% farther from the Sun and 50% smaller (diameter-wise) than the Earth. Mars has a similar internal structure and comparable composition to the Earth and shares many geological features such as volcanoes, ice caps, erosion features, and canyons. A notable difference is that the geological features on Mars are much larger than their counterparts on Earth. Due to this, they are suspected to have been created by slightly different processes. The key differences affecting geological features between the Earth and Mars are Mars's lack of plate tectonics (O'Neill et al. (2007)), lack of a dense atmosphere, significantly lower temperature, lower gravity, and its smaller radius which leads to a more curved planet. Many of these factors have also varied significantly throughout the history of Mars (McCollom (2006)), making analysis difficult.

The topography of Mars is one of the best data sources available to a scientist attempting to understand why and how these features formed. This is partially due to it being one of the only complete, high quality data sources, but mainly due to its high resolution and the wealth of topographical features on the planet, from ancient rivers and lakes to volcanos and canyons. Several notable topographical features can be identified on the surface of Mars, even to the untrained observer. Figure 1.1 (NASA/JPL/USGS (2000)) shows the topography of Mars with some notable features labelled. One unlabelled feature is the Tharsis bulge, which comprises nearly the entire red region on the right side of Figure 1.1. This region is a gigantic high plateau dotted with extremely large mountains and a very large canyon.

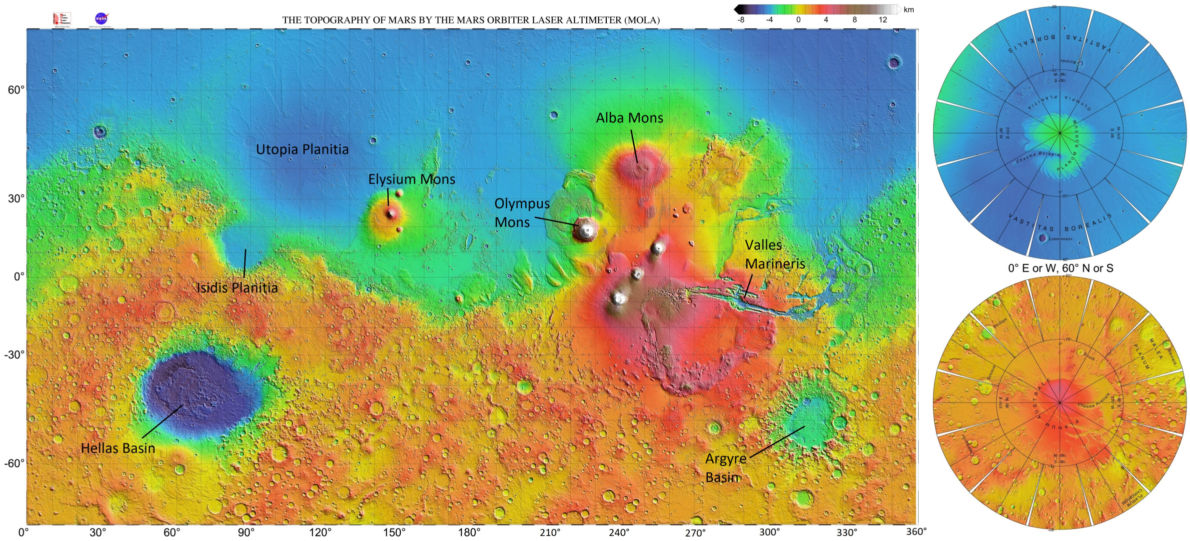

Figure 1.1: Topographical map of Mars from MOLA data, adapted from NASA/JPL/USGS (2000)

On a planetary scale, the topography of Mars is dominated by two geological features: the so-called Martian dichotomy and the Tharsis bulge. The Martian dichotomy is the name given to the elevation difference between the northern and southern hemispheres of Mars, clearly visible in Figure 1.1. The difference in elevation is several kilometers on average. There is much speculation as to why this dichotomy exists, but the origin of this feature is uncertain.

The northern hemisphere consists of low plains with small impact craters. These regions are relatively flat with no large topographical features. Along the dichotomy boundary the terrain becomes chaotic and both Elysium Mons and the northern edge of Tharsis can be found. The southern hemisphere consists of high plateaus with large impact basins, scattered smaller impacts, and the Tharsis province. Unlike the north, the south is relatively hilly and contains most of the large topographical features on Mars.

The Tharsis bulge is an equatorial elevated volcanic plateau which dominates the western hemisphere. It is essentially a continent-sized plateau of basalt formed by intense volcanic activity. Accordingly, three large shield volcanoes are found here (the Tharsis Montes), with the largest volcano on Mars (Olympus Mons) being found just off the western edge of the province. The plateau is up to 7 km above the Martian datum, with the shield volcanoes rising far higher.

In order to understand the topography of Mars it is useful to look at the gravity field of Mars. At first glance the gravity field of Mars appears constant across its surface but, just as on Earth, if one looks closely there are some important variations. At the same time gravity is caused by mass, and so it is logical that there should be more gravity near mountains and less gravity in craters. Combining these two pieces of information yields Figure 1.2, which shows the gravity field of Mars minus the non-spatially varying component, minus the gravity signal of the topography. Red areas are regions with more gravity than the topography suggests, while blue areas have less. If the spatially variable component of the gravity field of Mars was due solely to the gravity signal of the topography, Figure 1.2 would be zero everywhere. This is not the case, meaning that there is another source of spatially varying gravity signal on Mars. This necessarily must come from the subsurface, although it cannot be easily said how deep the mass responsible for the signal comes from.

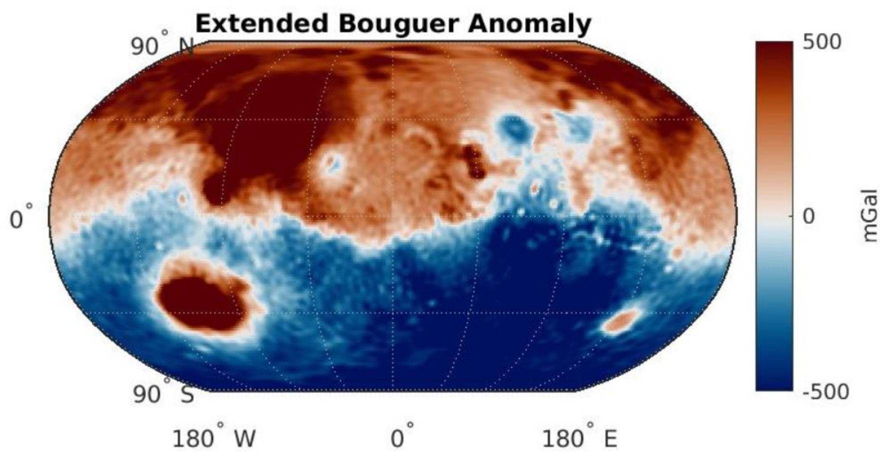

Figure 1.2: The extended Bouguer anomaly of Mars, using spherical harmonic degrees 1 to 90 and with $C_{2,0} = 0$. See Chapter 3 for more information. This can be understood as the gravity field of Mars minus the non-spatially varying component and minus the gravity signal of the topography. 1 mGal = $10^{-5} m/s^{-2}$.

In Figure 1.2 it is immediately clear that the dichotomy we observed in the topography is not present in the gravity field (if it were, the topography would not be visible in this plot, as the topography signal has been subtracted). Hellas basin has far more gravity than the topography suggests, as does Utopia planitia. Meanwhile many large volcanos in the Tharsis region are barely visible. This shows that there are large variations in the subsurface of Mars which only leads to more questions. Why is there extra mass under Utopia planitia? Why is there a lack of mass under Alba mons? To answer these questions some geological theories are needed.

The topography of the Earth is inseparable from its subsurface, for example, volcanic eruptions are caused by subsurface activity and mountain ranges are created by plate tectonics. There are some differences between the two planets, such as how mountains are formed by volcanism instead of plate tectonics, but in general the many similarities between the Earth and Mars lead researchers to believe that the topography and subsurface are similarly linked. Figure 1.3 shows the subsurface structure of the upper layers of the Earth. The topography of Mars is part of the crust, which rests on the mantle, which is itself divided into the upper and lower mantle. The depth at which the crust ends is called the Mohorovičić discontinuity or the Moho and is where there is a sudden shift in the rock composition. A different way of dividing the upper layers is with the lithosphere and the asthenosphere. The boundary between the two marks the shift from a rigid rock layer to a fluid one.

In this study, the terms 'mantle' and 'lithosphere-mantle boundary' are often used to refer to the non-rigid rock layer and to the boundary between the lithosphere and the non-rigid rock layer. Strictly speaking the non-rigid rock layer is the asthenosphere and not the mantle, as part of the lithoshpere also lies within the mantle. Similarly, the term 'moho' is sometimes used to describe the lithosphere-asthenosphere boundary.

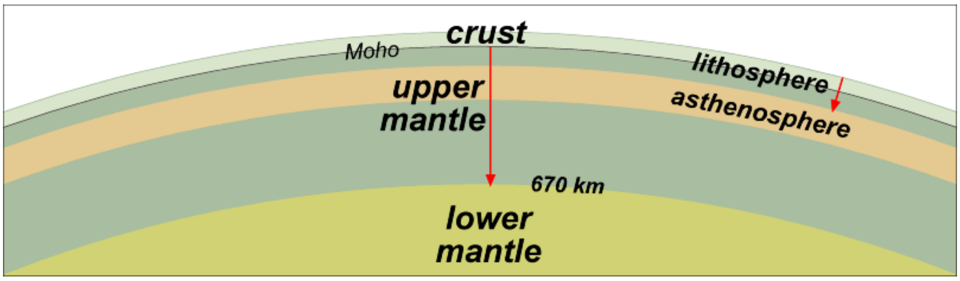

Figure 1.3: The internal structure of the upper layers of the Earth (DiVenere (2017)), with an estimation of the depth of the lower mantle. It is widely assumed that the subsurface structure of Mars is the same but with different layer thicknesses and densities (Wieczorek and Zuber (2004)). The crust rests on the lower mantle. The depth at which the crust ends is called the Mohorovičić discontinuity or the moho and is where there is a sudden shift in the rock density. The upper mantle rests on the lower mantle. A different way of splitting the upper layers of the planet is by the lithosphere and the asthenosphere. The boundary between the two marks the shift from a rigid rock layer to a fluid one.

There are several ways in which topography and the subsurface are related. One important relation is via the theory of isostasy. Isostasy refers to a model of the upper layers of a planet where a lithosphere composed of rigid material floats on a viscous mantle. The buoyancy forces cause changes in the lithospheric density and the depth of the lithosphere-mantle boundary. On Earth, the crust is divided into several rigid plates, but on Mars it is argued that a better model is that of a single spherical crustal plate floating over the mantle (Breuer and Spohn (2003), Mangold et al. (2000)).

There are many kinds isostatic models in use today for planetary subsurface studies, ranging from older models that only take bulk densities and moho depth as input to more modern models that incorporate seismic data and gravity anomalies (Watts (2001), Kaban et al. (2016)). Many of these newer models have been developed for use on Earth, where plate tectonics significantly impact the lithosphere and where seismic data is available. These differences make them difficult to apply to Mars. As the choice of isostatic model has a significant effect on the resulting lithosphere structure (Wild and Heck (2005)), it is essential to choose the correct model for an isostasy problem. Isostatic studies of Mars have returned results for the thickness, density, and composition of the lithosphere as well as various theories of how those parameters relate to the topography on the surface (Wieczorek and Zuber (2004)). The most significant parameters for an isostasy problem are the thickness of the lithosphere and the density of the lithosphere and the mantle. An accurate global map of these parameters would be a huge advancement for our understanding of the history of the topography of Mars. There is less variation in the estimates for the density of the lithosphere and mantle than for the lithospheric thickness (Neumann et al. (2004), meaning that better knowledge of the thickness is of particular interest.

A second theory that significantly affects the relationship between topography and the subsurface is flexure theory. Flexure theory states that the lithosphere can flex in order to support the load of its overlying topography Watts (2001). In a purely isostatic lithosphere, each discrete section of lithosphere compensates the topography directly above it. In reality however, the lithosphere is a rigid rock layer and each discrete element cannot move or exist independently of its neighbors. Flexure theory aims to model the support each discrete column receives from its neighbors, on a local, regional, and global level. Many flexure models exist, with most of them operating in the frequency domain in place of the spatial domain. The combination of an isostatic and a flexural model is a very powerful tool when modelling topography-lithosphere interactions.

Various studies have had differing results with these models. The thickness of the Martian lithosphere varies across the planet, ranging from 4 km to 125 km (Neumann et al. (2004)). This is determined by a nonlinear inversion of topography and gravity data from the Mars Global Surveyor (MGS) mission, after topography and crustal density anomalies (major volcanoes and the poles) are accounted for. Several density values (lithosphere, mantle, volcanic, etc) are estimated in order to perform this calculation, and the result is heavily dependent on these densities. The value of 4 to 125 km is obtained by performing the calculation with unusually high and unusually low densities, and thus encompasses the results from a wide range of density assumptions. Due to the dichotomy, the lithosphere in the Northern hemisphere is about 15 km thinner than in the Southern hemisphere (Neumann et al. (2004)). Additionally, the lithosphere under Tharsis is in general thicker than on other regions.

Wieczorek and Zuber (2004) use geoid to topography ratios (GTRs) as an input for an Airy isostasy model. The result is a distribution of crustal thicknesses across Mars. The results of other models are compared to the results of this paper's, showing a general consensus for long-wavelength features (Belleguic et al. (2005), Kieffer and Zent (1992), McGovern et al. (2004)), but the short wavelength features differ substantially.

Veldhuizen (2019) uses a combination of Airy isostasy and an infinite plate flexure model to calculate lithospheric thickness and lithospheric elastic thickness across the planet. The infinite plate flexure model models the topography as resting on an infinite plate (the lithosphere) which itself floats on the asthenosphere. This is done using a flexural response function instead of finite element analysis. This is a somewhat novel approach, making the results particularly interesting. Some topographical features are modelled very well by this method, while others require density variations or mantle gravity signals in order to be explained. The average values for the lithospheric thickness and lithospheric elastic thickness are found to be 55 km and 50 km respectively, which generally agrees with other studies. He concludes that flexural isostasy plays a large role in spherical harmonic degrees higher than 6 in the gravity signal and that this method works particularly well between degrees 25 and 52. The study is very positive about the results of this method of flexural isostasy.

Thor (2016) uses a different method based on statistical analysis to investigate the lithospheric elastic thickness of Mars. This method is completely different than that of Veldhuizen (2019), but the flexural model used is a thin shell flexure model. This kind of model is an extension of the infinite plate model used by Veldhuizen (2019). It differs from the infinite plate model by modelling the lithosphere not as an infinite plate but as a rigid shell encapsulating (yet still floating on) the asthenosphere. This model takes into account the curvature of the planet.

One of the disadvantages of analytical models as compared to finite element models is that they do not allow for regionally varying parameters. If the lithospheric thickness and density are both allowed to vary across the planet then it is impossible to solve the flexural isostasy problem analytically. A method to allow lithospheric parameters to vary in a flexural isostasy model is thus desirable. Wieczorek and Meschede (2018) provide a python package based on the mathematics of Wieczorek and Simons (2005) and Wieczorek and Simons (2007) which allows for the creation and manipulation of localized frequency domain functions that can be converted to and from the spatial domain. This provides exactly the tools needed to enable a flexural isostasy model that allows for regionally different lithospheric parameters.

This leaves a clear gap in the literature: a flexural isostasy study based on flexural response functions using both the infinite plate and thin shell model that allows for regionally different lithospheric parameters. Based on this goal and the results of previous studies it is possible to define a research question:

- *What is the impact of allowing for an anisotropic thin-shell, compared to a simpler infinite plate, in a topography loaded flexural isostatic model of Mars?*

This question sets the main research areas of this thesis: introducing a thin-shell model and an anisotropic thin shell model.

2

Data

2.1. Topography data

The topography dataset is the MOLA dataset. The Mars Global Surveyor (MGS) mission contained the Mars Orbital Laser Altimeter (MOLA) instrument. This istrument used laser ranging over several years of orbits to map the topography of Mars in resolutions of 128 pixels per degree (450 m/pixel at the equator). This instrument began its acquisition in 1997 and finished mapping in 2001. The dataset is the latest and highest resolution topography dataset for Mars and has been extensively used in studies of the planet (NASA/JPL/USGS (2020)).

The MOLA topography dataset used in this study is of a lower resolution than what is available. This is because the gravity data is at a far lower resolution than the topography data, and since both are used in this study the lowest resolution dataset is limiting. The gravity data is around one pixel per degree resolution, and so the topography must be converted to the same resolution. This is done by beginning with the lowest available resolution of topography (4 pixels/degree) and scaling it down using the $scatteredinterpolant$ function in MATLAB.

The results of this are shown in Figure 2.1. The figure shows the full range of the data, with the highest point being Mons Olympus and the lowest point being in Hellas Basin. The features in Tharsis are much higher than the rest of the topography, making the plot appear very uniform. Figure 2.2 shows the same data with a fixed colorbar of -6 to 6 kilometers. This figure exposes much more detail. Large features such as the dichotomy, the tharsis volvanos and large impact basins are visible. Some of these features will be explored in more detail in this study.

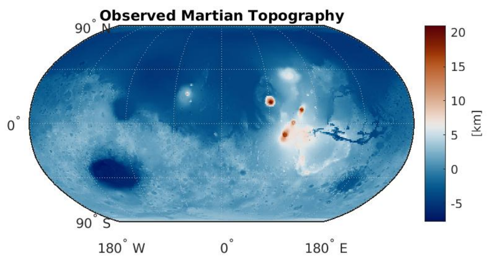

Figure 2.1: Observed topography of Mars. This dataset is taken from an instrument on a NASA satellite: the MOLA instrument NASA/JPL/USGS (2019).

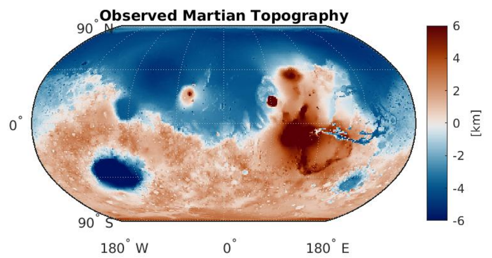

Figure 2.2: Observed topography of Mars with a limited colormap of 6 to -6km. The dataset is the same the one in Figure 3.1, with the data coming from the MOLA instrument NASA/JPL/USGS (2019).

2.2. Gravity data

The gravity dataset used in this study is the GMM-3 gravity model created by Genova et al. (2016). This is the most recent gravity model of Mars and was created by observing the trajectories of three spacecraft: the Mars Global Surveyor (MGS), Mars Odyssey, and Mars Reconnaissance Orbiter (MRO). It is provided in spherical harmonics, going up to degree 120. Eleven years of data were used to estimate the seasonal variations in the gravity field. The contribution of the mass of the atmosphere was also taken into account. These two factors and an improved modelling of the trajectory of the three satellites are what makes this model more accurate than previous models.

The data is provided in spherical harmonics format. This is a set of coefficients from which the gravity field can be generated using Equation 2.1, where $U(\mathbf{r})$ is the gravitational potential at position $\mathbf{r}$, l is the spherical harmonic degree, m is the spherical harmonic order, Y_{lm} are the standard spherical harmonics, and the position $\mathbf{r}$ is made up of the three spherical components $\mathbf{r}, \theta, \lambda$ (or equivalently the coordinates $\mathbf{r}, \Omega$).

$$U(\mathbf{r}) = \frac{GM}{R} \sum_{l=0}^{\infty} \sum_{m=-l}^{l} \left(\frac{R}{r}\right)^{l+1} C_{lm} Y_{lm}(\Omega) \tag{2.1}$$

The satellite tracking data used to create the gravity model leads to a higher resolution on some parts of the planet than on others. Figure 2.3 shows the maximum degree strength across the surface of Mars. The maximum degree strength ranges from a maximum around the poles to a minimum around the northern plains. This latitude dependence is due to the highly elliptical orbits of the orbiting satellites. The lowest degree strength is around 85 on the northern plains, while the rest of the planet is at around 90 or higher. As most of the topographical features on the planet are in the southern hemisphere, these degrees will be used for the analyses in this study.

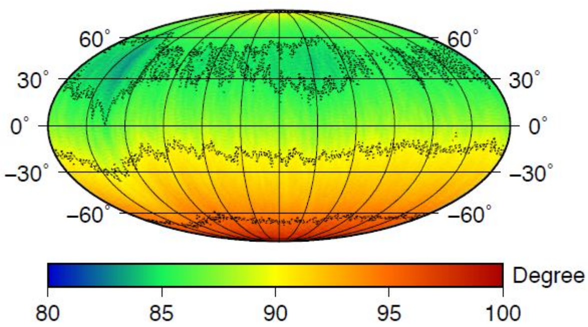

Figure 2.3: GMM-3 maximum degree strength across Mars (Genova et al. (2016)). Due to the satellite tracking data, some regions of the gravity field are mapped in higher resolution than others. The large latitude dependency is due to the highly elliptical orbits of the satellites.

Figure 2.4 shows the free air gravity anomaly of the GMM-3 model expanded at each point only up to the maximum degree strength at that point. This means that each region shows to the maximum degree shown in Figure 2.3. The free air anomaly is the gravity signal at the surface of the planet with the central terms removed: see Chapter 3 for more information. The observations used in this study will be created directly from the spherical harmonic coefficients up to degree 90, and will not use the free-air signal in Figure 2.4. Instead, the free air gravity shown here will be used as verification data for the free air gravity computed in this study.

2.3. Other data used

There are various estimates for the density of the Martian lithosphere. The commonly cited bulk value is 2900 kg/m^3, obtained from satellite gravity measurements (Neumann et al. (2004), Belleguic et al. (2005), Wieczorek and Zuber (2004)). The local density of the crust at any point can vary significantly, ranging from 2350 to 3350 kg/m^3. It is also known that the shield volcanoes are denser than the surrounding crust (Beuthe et al. (2006), Beuthe et al. (2012)). These observations match what is found on volcanoes and local crusts on

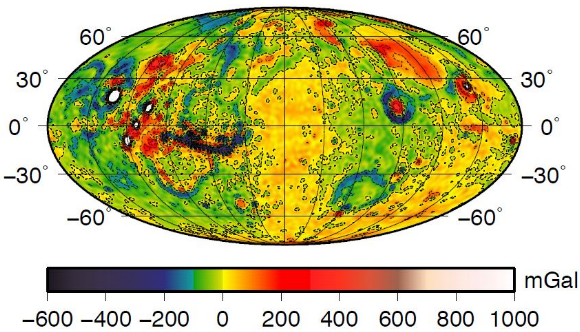

Figure 2.4: GMM-3 free air anomaly (Genova et al. (2016)), expanded up to the maximum degree at each point (see Figure 2.3).

Earth.

The mantle density ranges from 3100 kg/m^3 (at the crust boundary) to 4100 kg/m^3 (at the core boundary) (Breuer and Spohn (2006)), with 3500 kg/m^3 being the mean density (Neumann et al. (2004)). Note that the density of the mantle depends on how deep the crust and core boundaries are assumed to be. A thin lithosphere means that the mantle begins closer to the surface and is under less pressure, and so will result in a lower mantle density. Likewise, a thick lithosphere means that the mantle will begin deeper and thus be denser. Additionally, the composition of the mantle has a large influence on its density. Neumann et al. (2004) states that the Martian mantle is more iron-rich than that of the Earth, meaning its density must be higher than that of the Earth's. Therefore, the composition of the Martian mantle is determined by chemical modelling or fitting a bulk density to gravity data. The accuracy of both of these methods is unknown, as the density of the Martian mantle has not been directly observed nor measured through seismographs, but they both agree on a range of possible densities for the mantle. These methods provide the best estimate for Martian mantle thicknesses as provided by Breuer and Spohn (2006) and Neumann et al. (2004).

The selected value of the parameters used in this study are summarized in Table 2.1.

Parameter	**Value**	**Unit**
Young's modulus	$1e11$	Pa
Crustal density	2900	kg/m^3
Mantle density	3500	kg/m^3
Poisson's ratio	0.25	–
Planetary radius	3396200	m
Standard gravitational parameter	$4.2621e13$	m^3/s^2
Surface gravity	3.711	m/s^2

Table 2.1: Input parameters used in this study (Wieczorek and Zuber (2004), Belleguic et al. (2005), Beuthe et al. (2012), Neumann et al. (2004), Neumann et al. (2004), Breuer and Spohn (2006), Beuthe et al. (2006)).

3
Theory

3.1. Gravity reductions

A gravity reduction is the subtraction of a known gravity signal from a planetary gravity field. This is done in order to better observe the remaining gravity field, and to judge the accuracy of the subtracted gravity signal. In this study several gravity reductions will be performed, with the subtracted signal being generated from topography data.

Topography can be measured at high resolution by orbiting satellites. As this data is very valuable to geo-scientists, several missions have observed the Martian surface over the decades, with the most recent and complete topography dataset being the MOLA dataset. The Mars Orbiter Laser Altimeter (MOLA) was an instrument on NASA's Mars Global Surveyor (MGS) mission which stopped acquiring data in 2001 (NASA/JPL/USGS (2019)).

Figure 3.1 shows the observed topography of Mars (MOLA Dataset), using spherical harmonic degrees 0 to 90. This is the dataset that will be used in this thesis. In the figure, the large volcanoes in the Tharsis region stand out as far larger in magnitude than any other feature. Figure 3.2 shows the same topography dataset with a limited colorbar. The dichotomy is clearly visible, as is Hellas Basin, the Tharsis bulge, and Elysium Mons. These large topographic signals likely have a corresponding subsurface disturbance associated with them. Both these figures are very similar to Figures 2.1 and 2.2: the only difference is that terms above 90 were not used in the figures presented in this chapter. The effect of these high degrees cannot be seen in the figures because their effect is very small compared to degrees 0 to 90.

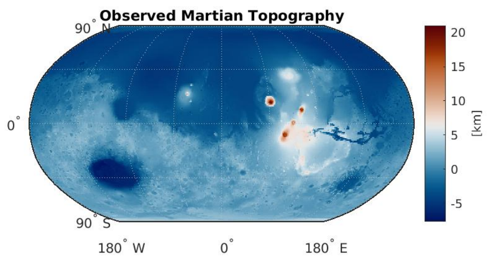

Figure 3.1: Observed topography of Mars. This dataset is taken from an instrument on a NASA satellite: the MOLA instrument NASA/JPL/USGS (2019).

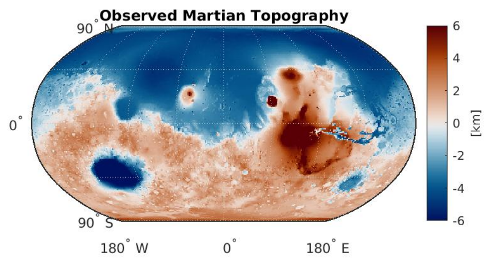

Figure 3.2: Observed topography of Mars with a limited colormap of 6 to -6km. The dataset is the same the one in Figure 3.1, with the data coming from the MOLA instrument NASA/JPL/USGS (2019).

Figure 3.3 shows the observed gravity field of Mars, using spherical harmonic degrees 0 to 90. The magnitude is about 3.7m/s^2, with what at first glance seem like minor variations (less than 0.1 m/s^2) across the planet. The clearest gravity signal is that of the equatorial flattening, as happens with Earth. This results in a slightly higher gravity at the equator than at the poles. Also visible are the volcanos in the Tharsis region, with a strong positive gravity signal.

The gravity reductions used in this study differ from the classical approach, due to the use of spherical harmonics. The spherical harmonics coefficients allow for the selective splicing of the gravity field according to the size of the mass causing the gravity signal. Setting the terms of a spherical harmonic degree to zero immediately removes the signal of that degree from the gravity field, while leaving the rest of the signal unaffected. The first reduction to be done is removing the central terms of the gravity field. This is the largest signal, and comes from the bulk mass of the planet. In spherical harmonics this is very easy: the degree 0 and 1 terms are set to zero.

Figure 3.4 shows the gravity field with the central terms (degrees 0 and 1) removed. For background on spectral analysis of gravity fields, see Chapter 3. While the figure looks the same as the full gravity field, the magnitude is far smaller. The most significant feature is still the equatorial flattening, which corresponds to the spherical harmonic term C(2,0). Thus the next gravity reduction to be performed addresses this feature.

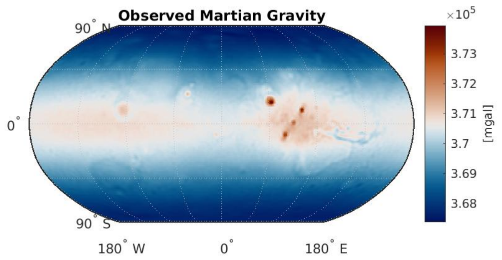

Figure 3.3: Observed gravity of Mars. The dataset is from the GMM-3 model Genova et al. (2016)

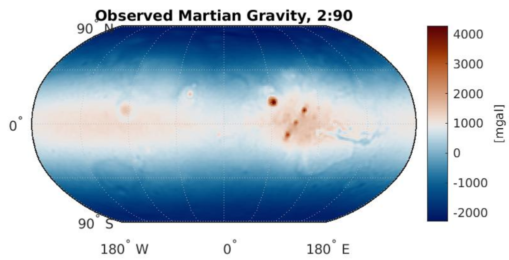

Figure 3.4: The observed gravity of Mars with central degree 1 spherical harmonic terms removed (terms 2:90 remain).

Figure 3.5 shows the Martian gravity field with the central terms removed and C(2,0) set to zero. After these reductions, this gravity signal is known as the free air anomaly, and will be referred to as such for the rest of this thesis. There is little detail visible in the figure, as the gravity signals of the Tharsis volcanos are far larger than the rest of the planet. This makes it difficult to interpret. Figure 3.6 shows the same figure as Figure 3.5, but with a limited colorbar. The Tharsis volcanos are now saturated, as is Valles Marineris, Elysium Mons, and Isidis Planitia. Far more detail is visible in the rest of the planet. Several noteworthy features which can be seen in this figure will be discussed below.

The free air anomaly of Mars does not correlate very strongly with the topography of Mars (as shown in Figure 3.2). The dichotomy signal has been removed by removing the central terms, but other large features such as Hellas Basin and Argyre Basin are not prominent. Conversely, Isidis Planitia and Utopia Planitia are clearly visible in the free air anomaly, but do not have a corresponding topographic signal. As gravity is produced by mass, an extra positive mass should result in an extra positive gravity signal, but this does not seem to be the case.

Some positive gravity signals have a ring of negative signal around them. This is visible on the Tharsis bulge, where half the planet forms a negative gravity signal ring around it. It is also visible at Isidis Planitia on a much smaller scale. In the case of Tharsis the positive gravity signal comes from the massive Tharsis bulge, but in the case of Isidis Planitia there is no corresponding topographic signal. Yet both areas show a negative ring surrounding their positive signal, while there is no corresponding topography for the ring.

The northern hemisphere is Mars is nearly devoid of topography, but this is not the case in the gravity signal. The free air anomaly shows geographically large positive and negative signals, as well as smaller patches of positive and negative signal. The origin of these signals is unclear.

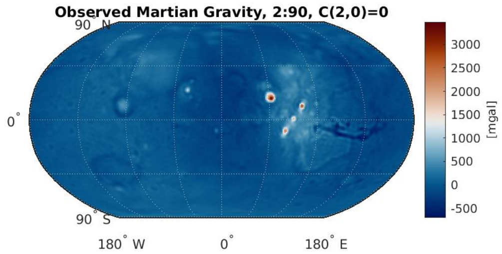

Figure 3.5: The observed gravity of Mars with central terms removed (2:90 remain) and C(2,0) set to zero.

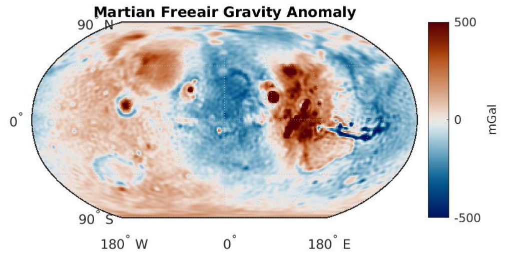

Figure 3.6: Free air gravity anomaly of Mars, using spherical harmonics degrees 2:90, with C(2,0) set to zero.

Having observed this, the next reduction can be applied. Although they are related, gravity and topography signals do not always correlate, making analysis difficult. The relation between gravity and mass is well known, and since a topography dataset is a mass distribution, the topography dataset can be used to calculate a gravity signal. This is the gravity signal of only the topography, known as the Bouguer reduction. When subtracted from the free air gravity signal a new gravity signal is obtained, called the (extended) Bouguer anomaly (Watts (2001)). If the free air anomaly consisted of only the gravity signal of the topography, the Bouguer anomaly would be zero. A non-zero Bouguer anomaly indicates that there is another, non-topographic source of gravity signal. The extended Bouguer correction is typically calculated as shown in Equation 3.1 (Fowler (1993)), with δT being a terrain correction which compensates the Bouguer correction from being applied to a planetary surface instead of an infinite horizontal plane. However, in this study the gravity signal of the topography is calculated directly using the GSH software (see Chapter 4) instead of with an equation.

$$\delta B_{ext} = -2\pi G \rho h + \delta T \tag{3.1}$$

Figure 3.7 shows the Bouguer anomaly of Mars. There are many positive and negative signals, which, once again, do not fully correspond to topography. The gravity signals in this anomaly must come from somewhere else than topography, which for a planet can only be sub-surface mass anomalies. This mass anomaly can take many forms, including but not limited to a density anomaly, subsurface volcanism, or the remains of a large impact or other large event (Watts (2001)).

Figure 3.8 shows the Bouguer anomaly of Mars when the spherical harmonic degree 1 is included. This re-introduces the dichotomy signal, again making it difficult to clearly see many other features. However, the dichotomy does exist, meaning it should be included in global analyses if the results are to be meaningful. Some later analyses in this thesis will include the dichotomy.

The Bouguer anomaly shows the gravity signal that is left when terrain, measurement conditions, and central gravity terms are removed. A positive anomaly thus indicates that, locally, there is more mass than expected either on or underneath the surface. A negative anomaly indicates the opposite. The large volcanoes of the Tharsis region had a free-air anomaly of around 900mGal, yet their Bouguer anomalies are nearly zero, and even slightly below zero. Conversely, Hellas Basin has a very large positive Bouguer anomaly, while only its rim had a significant non-zero (and negative) free-air anomaly. These observations give clues about the subsurface and formation of those features. Hellas Basin's extra mass could be explained by a very thin lithosphere in the crater, meaning that the denser mantle is very near to the surface. The opposite is implied for the Tharsis volcanoes and the negative-anomaly region surrounding them: a very thick crust means that the Moho depth is higher and that the denser mantle is farther from the surface. The principle tool used to investigate the results of the Bouguer anomaly in terms of subsurface structure is isostasy, which is discussed in the following section.

The Bouguer reduction incorporates the gravity signal of the topography into the gravity signal. However, there is more information in the topography signal that can be used to further reduce the gravity signal. This is done via geological models which use topography information to generate information about the subsurface. Some of these geological models will be explored in this study.

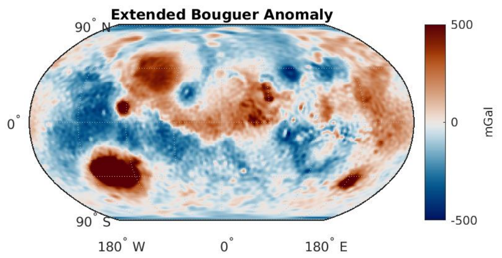

Figure 3.7: The extended Bouguer anomaly of Mars, using spherical harmonic degrees 2 to 90 and with $C_{2,0} = 0$.

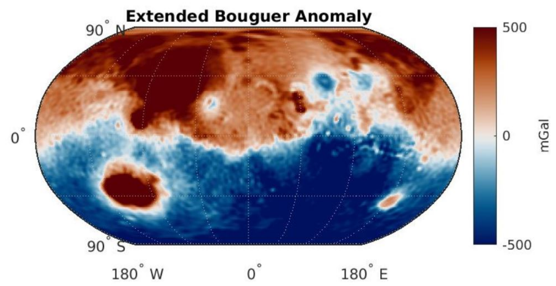

Figure 3.8: The extended Bouguer anomaly of Mars, using spherical harmonic degrees 1 to 90 and with $C_{2,0} = 0$.

3.2. Isostasy

The Airy isostatic model is one of the oldest and simplest formulations of isostasy (Watts (2001)). Despite this, it is still used in modern studies (Wieczorek and Zuber (2004)). Airy isostasy models the lithosphere as discrete columns composed of topography, crust, and mantle material. The average crustal thickness and the topography height are the inputs to the model. Each column's topography causes a change in the depth of the crust-mantle boundary (a 'root') in the column from the average depth of the crust-mantle boundary in the model. The change in depth is given by Equation 3.2, where the root r (positive downwards) is related to the height of the topography h and the crustal and mantle densities ρ_c and ρ_m. Columns with positive topography have a deeper crust-mantle boundary and vice versa. This is shown graphically in Figure 3.9. Note that the root is added to the average crustal thickness: it is a modification of the average. The average crustal thickness must be provided to the model, it cannot calculate it.

$$r = \frac{h\rho_c}{\rho_m - \rho_c} \tag{3.2}$$

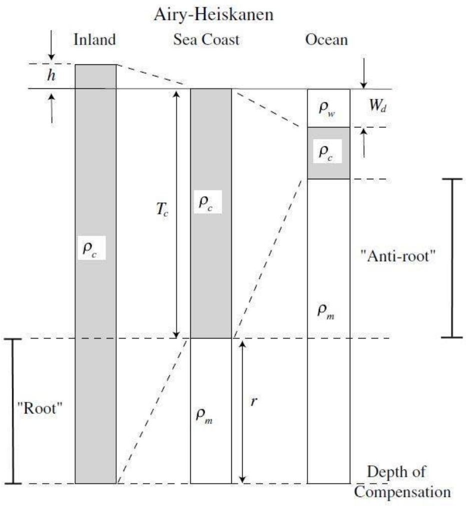

Figure 3.9: A diagram of the Airy or Airy-Heiskanen isostasy model (Watts (2001)). A topographic load causes a change in the crust-mantle boundary (a 'root' r) in a subsurface with a crust and an underlying mantle with densities of ρ_c and ρ_m respectively. Positive topography (h), such as a mountain or continental shelf, causes a positive (deeper) root, while negative topography'(W_d), such as an impact crater or an empty oceanic basin, causes a negative (shallower) root. The depth of compensation is equal to the depth of the deepest root, and is the depth at which the weight the overlying material in each column is equal.

The Moho depth profile generated by the Airy model is an upside down version of the input topography profile. Due to this, the subsurface has less mass beneath positive topography and more mass beneath negative topography. This results in a gravity signal of the topography and subsurface that is much smoother than the gravity signal of the topography alone, as the subsurface at least partially cancels out the topography. This gravity signal can then be compared to the observed gravity signal at the topography: if they match, then the subsurface likely looks as predicted by the Airy model. The structure of the subsurface under individual topographical features, such as voclanos and craters, can be investigated in this way. The Airy model is thus a method for turning topography data into subsurface structure information.

3.3. Flexure Theory

The first model is taken from Watts (2001) and is referred to as the infinite plate model in this study. It models the lithosphere an infinite plate supporting a distributed topographical load (Watts (2001)) floating over a viscous mantle. This is shown graphically in Figure 3.10. Structural engineering formulas can be applied to model the deflection of the lithosphere, and the equilibrium state of the lithosphere under load can be calculated. This model operates in the spherical harmonics domain, meaning the topography dataset (which is acquired in the spatial domain) must be converted to spherical harmonics before use. A disadvantage of this model is that because a planet is spherical, an infinite plate is not an ideal representation of the lithosphere. An advantage of this model is that it was previously applied to Mars by Veldhuizen (2019), providing a good source to verify the results of this study.

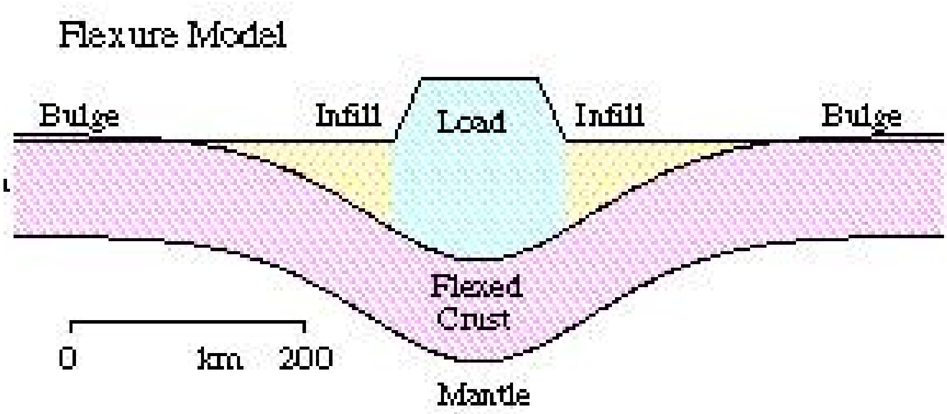

Figure 3.10: Infinite plate flexure model representation (Watts (2001)). A large topographical load causes the underlying crust to deflect downwards into the mantle. Over time, sediment and other material (infill) can accumulate around the load, increasing the load on the lithosphere. Farther from the load, the flexing of the crust causes a small upwards movement of the crust.

This study will focus on the flexural response functions of the selected flexure models. The flexural response function is defined as the output (deflection or flexure) of the lithosphere divided by the input (the load). For the Airy model, the flexural response function is equal to one, as there is essentially infinite flexure. The deflection of an infinite elastic plate that overlies a weak fluid substratum to a periodic load A$\cos kx$, where A = $(\rho_c - \rho_m)$gh, is given by Equation 3.3 (Watts (2001)). This equation is taken from structural mechanics.

$$D\frac{\delta^4 y}{\delta x^4} + (\rho_m - \rho_{infill})yg = (\rho_c - \rho_w)gh\cos(kx) \tag{3.3}$$

Where y and x are the vertical and horizontal coordinates, g is the gravitational acceleration, and the flexural parameter D is as defined in Equation 3.4.

$$D = \frac{ET_e^3}{12\left(1-\nu^2\right)} \tag{3.4}$$

The parameters E and ν are the modulus of elasticity and the Poisson's ratio of the subsurface, respectively. As mentioned in Chapter 2, typical values for Mars are E = 1e11 and ν = 0.25. The parameter T_e is known as the effective elastic thickness of the lithosphere. This is the thickness of an elastic plate needed to reproduce the same deformation as seen in the lithosphere, and is a useful mathematical parameter. It is effectively a measure of the resistance to flexure of the lithosphere, with higher a T_e indicating a stronger lithosphere. The solution to Equation 3.3 yields the deflection of the lithosphere in response to the load. This can be divided by the input load, yielding a of the output deflection to the input load. This is called the flexural function, which for this model is shown in Equation 3.5.

$$\Phi_e(k) = \left(\frac{Dk^4}{(\rho_m - \rho_{infill})g} + 1\right)^{-1} \tag{3.5}$$

Equation 3.5 shows the flexural response function in terms of the wavenumber k, but it is mathematically convenient to works instead with the spherical harmonic degree n. Using the relation in Equation 3.6 Watts and Moore (n.d.), the flexural response function becomes Equation 3.7.

$$k = \frac{2n+1}{2R} \tag{3.6}$$

$$\Phi(n) = \left(1 + \frac{D}{(\rho_m - \rho_c)g}\left(\frac{2n+1}{2R}\right)^4\right)^{-1} \tag{3.7}$$

This response function can be multiplied with an Airy type lithosphere in spherical harmonics format in order to obtain the output, flexed lithosphere in spherical harmonics format.

A second model models the lithosphere as a thin shell of material floating on a viscous spherical mantle. The thin shell model used in this study is taken from Beuthe (2008). The equations derived by the author are very general, must be solved numerically, and can include a shell of varying thickness or varying Young's modulus. A limit case is derived for the case of a shell of constant Young's modulus who's thickness is small enough that the bending stresses inside it can be neglected. The author calculates that the lithosphere of Mars is thin enough to make this assumption valid. For this limit case an analytical solution exists in the frequency domain, making implementation possible in this study. Figure 3.11 (Thor (2016)) shows a diagram of a cross section of a planet where the limit case applies.

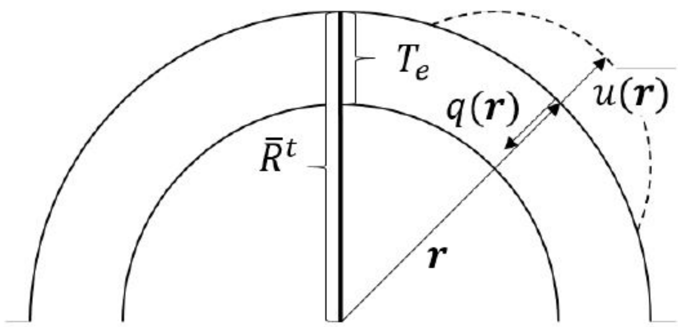

Figure 3.11: Thin shell flexure model diagram for the limit case described in Beuthe (2008), created by Thor (2016). A planet with a thin shell lithosphere floating over a viscous interior. A radial position-dependent load $q(r)$ causes a radially varying displacement $u(r)$ of the thin shell.

The main equation in the limit case is not written in spherical harmonics, which is the form needed for this study. The spherical harmonics form of the equation is provided by Thor (2016) and is shown in Equation 3.8.

$$\left(\frac{ET_e^3}{12\left(1-\upsilon^2\right)}\left(-n^3(n+1)^3 + 4n^2(n+1)^2 - 4n(n+1)\right) + \bar{R^t}^2 ET_e(-n(n+1)+2)\right) u_{lm} = -\bar{R^t}^4(-n(n+1)+1-\upsilon)\, q_{lm} \tag{3.8}$$

In Equation 3.8, $\bar{R^t}$ is the radial distance from the center of the planet at position **r**, u_{lm} is the spherical harmonics coefficients of the deflection (positive upwards) of the shell while q_{lm} is the spherical harmonic coefficients of the loading pressure (positive downwards). It can be seen in Equation 3.8 that the signal of the deflection, or the output (u_{lm}) is present, along with the signal of the load, or input (q_{lm}). The equation can be rearranged in the form of a flexural response function, as shown in Equation 3.9.

$$\frac{u_{lm}}{q_{lm}} = \Phi(n) = \frac{-\bar{R^t}^4(-n(n+1)+1-\upsilon)}{\frac{ET_e^3}{12(1-\upsilon^2)}\left(-n^3(n+1)^3 + 4n^2(n+1)^2 - 4n(n+1)\right) + \bar{R^t}^2 ET_e(-n(n+1)+2)} \tag{3.9}$$

It is useful for the flexural response function of this model to be expressed in the same form as those of the Airy and infinite plate models. Rewriting Equation 3.9 by inverting the fraction, substituting the parameter D from Equation 3.4, and collecting like terms yields the final form of the flexural response function for the thin-shell model, shown in Equation 3.10.

$$\Phi(n) = \left(1 + \frac{D}{(\rho_m - \rho_i)g}\frac{1}{T_e}\left(\left(\frac{2n+1}{2R}\right)^4 \frac{-4.5n^2 - 4.5n + 4 - \frac{1}{16}}{1 - \frac{1-\nu}{n(n+1)}} + \frac{12(1-\nu^2)}{T_e^2 R^6}\frac{1 - \frac{2}{n(n+1)}}{1 - \frac{1-\nu}{n(n+1)}}\right)\right)^{-1} \tag{3.10}$$

There are several benefits of deriving flexural response functions for the models in this study. Firstly, they are very useful computationally as a Moho profile can be easily multiplied by such a function in order to obtain its deflection. Second, the functions of the three models are of the same form, allowing for easy comparison of the selected models. Finally, they reduce the flexure problem to one simple formula that is dependent only on the physical characteristics of the lithosphere, the size of the planet, and the strength of the planet's gravity field.

A comparison of the flexural response functions of the three models shows some similarities. Table 3.1 shows a comparison of the response functions of the three models. The three functions have the same form, with each successive model adding extra terms to the base function. This is to be expected as the infinite plate model adds flexure to the Airy model, and the thin-shell model adds the curvature of the lithosphere to the infinite plate model. The addition of more physics to a model results in more terms in it's response function, and overall a more complex model.

Model	**Response function format**
Airy	$\Phi(n) = (1)^{-1}$
Infinite plate	$\Phi(n) = (1 + \mathbf{AB})^{-1}$
Thin shell	$\Phi(n) = (1 + \mathbf{A}(\mathbf{BC} + \mathbf{D}))^{-1}$

Table 3.1: A comparison of the flexural response functions of the three models used in this study. The three functions have the same form, with extra terms being added with each successive model. The parameters **A**, **B**, **C**, and **D** are placeholders for terms in the flexural response functions and are meant to show the similarities between the equations.

A flexural response function Φ(n) can be multiplied with an Airy Moho depth profile A_{lm}n spherical harmonics format in order to obtain a new Moho depth profile M_{lm} as shown in Equation 3.11. The multiplication is performed by multiplying all orders (m) of each degree (l) of the Moho depth profile with each degree (n) of the flexural response function.

$$M_{lm} = A_{lm}\Phi(n) \tag{3.11}$$

Flexural response functions are the main method of this study. They are the mechanism that incorporates flexure into a lithosphere profile. In order to investigate them further, the flexural response functions of the infinite plate and thin shell models are plotted for a variety of T_e values in Figure 3.12. The figure shows three response functions per model with T_e values of 40, 120, and 400km. These plots are in the frequency domain, and show how much attenuation each degree receives from the flexural response function. The response function of the Airy model is not plotted as it is one for all spherical harmonic degrees.

The response functions of both models show a similar pattern. Higher Te's lead to a less permissive response function, which is further left in the plot. The function allows only the first few degrees to pass, attenuates the next 5-10, and blocks the rest. A lower Te leads to the opposite effect: the response function shifts right, and allows tens of Te's to pass with very little attenuation. Only the lowest degrees are blocked.

For identical values of Te, the thin shell model attenuates significantly more, and earlier. Fewer degrees are allowed to pass with no attenuation, and the attenuation increases very rapidly. For a very high Te it acts more like a binary filter, meaning that some degrees are allowed to pass unmodified while all others are blocked completely.

The reason that flexure models were run for degrees 2:90, 2:20, and 2:10 can also be seen in these plots. For all but the lowest T_e models, degrees 2:20 capture all of the degrees which are attenuated by flexure. Degrees outside of this range are either fully passed, or fully blocked. The 2:10 range captures all to none of the attenuated degrees, depending on the model and T_e used. This property makes it useful when the spatial domain implications are considered. A range of 2:20 captures all the effects of flexure, while a range of 2:10 captures the response the flexure model to only the largest spatial features.

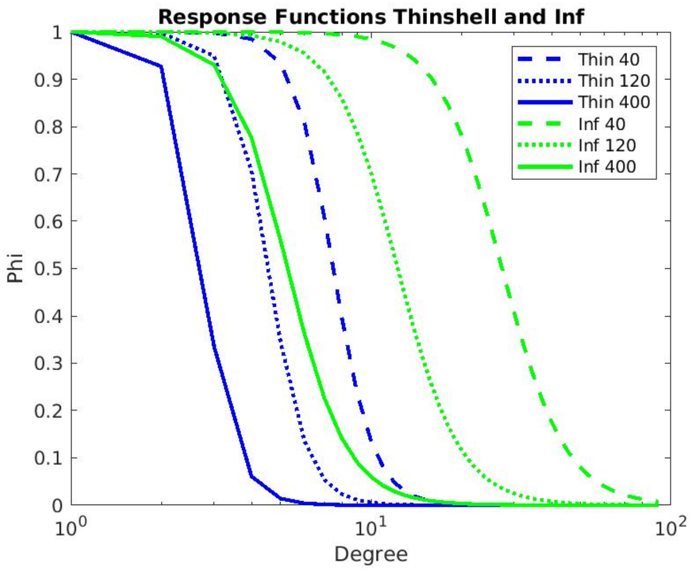

Figure 3.12: Plots of the flexural response functions of the infinite plate and thin shell models are plotted for a variety of T_e values. Three response functions per model are shown with T_e values of 40, 120, and 400km. This plot is in the frequency domain, meaning the lines show how much attenuation each degree receives from the flexural response function. The response function of the Airy model is not plotted as it is one for all spherical harmonic degrees.

3.4. 3D analysis

A flexural response function is multiplied with a series of spherical harmonic coefficients. This means that it is applied over the entire planet: all of the spatial domain. Some of the analyses is this study rely on treating different areas in the spatial domain as having different properties, such as lithospheric thickness or crustal density. This is not possible using a single flexural response function, as the response function is determined by these physical characteristics. The solution to this problem is the use of localization windows, which have been implemented into a python package (pyshtools) by Wieczorek and Meschede (2018).

A localization window allows for the spatial localization of a frequency domain function via spherical localization caps, which are frequency domain analogues to the Cartesian Slepian functions (Wieczorek and Simons (2005), Wieczorek and Simons (2007)). Using the pyshtools package it is possible to 'cut' a sphere into arbitrarily shaped pieces (windows), multiply each window with a different function, and then re-combine all the windows back into one sphere. This software package was used by Broquet and Wieczorek (2019) to investigate individual volcanos. Mathematically this is performed as shown in Equation 3.12 (Broquet and Wieczorek (2019)). In this equation, G is the localized function, g is the global function, and h is the localization window. In this study, the global function g is equivalent to the term M_{lm} in Equation 3.11.

$$G(\theta,\phi) = g(\theta,\phi)h(\theta,\phi) \tag{3.12}$$

While Equation 3.12 is in the spherical harmonics domain, for ease of visualization an example will be shown in the spatial domain, although the mathematical treatment is still in the spherical harmonics domain. Figure 3.13 shows a global signal of an intermediate product from a model in this study. This signal exists as an instance of the pyshtools class object SHGrid, which is a class for global gridded data that can be converted into spherical harmonic domain with one command. Figure 3.14 shows a SHGrid instance generated with the pyshtools package. This signal is generated by creating a SHGrid.cap object of radius 15 degrees, a (lat, lon) position (23, 147), and a maximum spherical harmonic degree of 89. This results in a binary spatial domain signal which is zero everywhere except within a 15 degree radius circle of the given (lat, lon) position. These coordinates correspond to the volcano Elysium Mons.

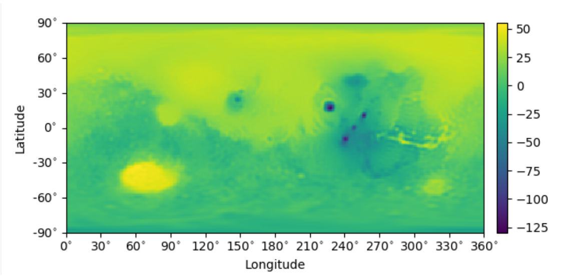

Figure 3.13: A plot of an example SHGrid object from pyshtools containing a global signal of an intermediate product of one of the models in this study.

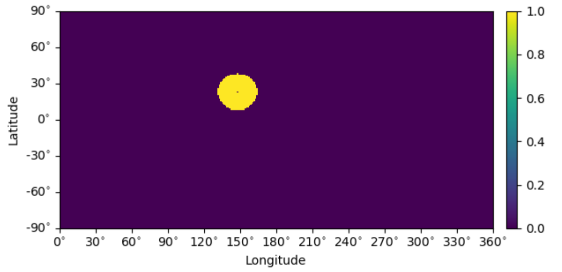

Figure 3.14: A plot of an example SHGrid.cap object centered around the volcano Elysium Mons. This was generated with a radius of 15 degrees, a (lat, lon) position (23, 147), and a maximum spherical harmonic degree of 89. This results in a binary spatial domain signal which is zero everywhere except within a 15 degree radius circle of the given (lat, lon) position.

Figure 3.15 shows a plot of the SHGrid object resulting from the multiplication of the SHGrid objects in Figures 3.13 and 3.14. The signal shows only the area covered by the cap in Figure 3.14. Using a command in the pyshtools package it is possible to pass this signal to spherical harmonics form and back at any time, which is how the regional analyses are performed in this study. This process could be repeated with a cap covering a different volcano with the same results. Additionally, those two resulting plots could be added together using pyshtools in order to obtain a signal with strength zero everywhere except at the two chosen regions. This is how the multi-region analyses are performed.

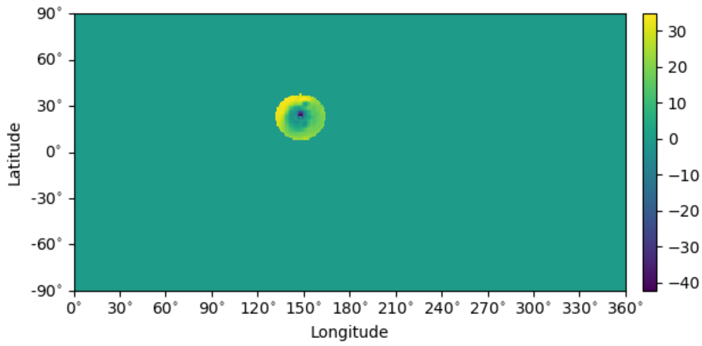

Figure 3.15: A plot of the SHGrid object resulting from the multiplication of the SHGrid objects from Figures 3.13 and 3.14. In a way this is still a global signal, but most of the signal consists of zeros. Using a command in the pyshtools package it is possible to pass this signal to spherical harmonics form and back at any time.

The manipulation of signals with pystools introduces some numerical error with each transformation from spatial to spherical harmonic domain. This error is only significant, however, when there is a mismatch in the spatial and frequency domain of a window. If a very spatially small SHGrid.cap object is created with a very low maximum spherical harmonic degree there will be significant errors, as those low degrees cannot resolve such a spatially small area. Note that this problem is not unique to Slepian functions, it is a result of the formulation of spherical harmonics. When the maximum spherical harmonic degree of a region is high enough to resolve the area without significant errors the remaining numerical error is no greater than that of a regular spatial domain to spherical harmonics domain transformation (Broquet and Wieczorek (2019)).

3.5. Residuals and RMS

Up to now the theory has covered the models used in this study. The goal, of course, is to create a model that approximates reality in order to learn about the subsurface of Mars. In order to do this it is necessary to compare the results of the model to the observations of reality. There are several methods of comparing model results to observations, each with their own advantages and disadvantages. Several tools will be used in tandem to judge the performance of the models in this study.

The first (and perhaps most obvious) tool being used in this study is a visual human inspection of the observation, modelled, and residual gravity signals. This method has the advantage of being very thorough as it uses the full knowledge of the human performing the inspection, but is less useful when large numbers of models need to be assessed. In this study a large amount of models will be generated, and it is not feasible to interpret the results of each model by visual inspection. For example, if we consider a region being modelled by a model with two parameters with 6 values per parameter, then the search space is already 36 models. It is then clear that a faster method of judging the performance of a model is required. That said, this method is the best method to interpret the results of models when time allows, due to the speculative nature of this field. The visual inspection method will be used extensively in this study, with the other methods acting as indicators of which models are worth inspecting.

A method used by previous students is that of calculating the global RMS value of the results (Veldhuizen (2019), de Bakker (2016)). This is done as shown in Equation 3.13, with N being the number of pixels, obs is the observations per pixel, and $calc$ is the model results per pixel.

$$RMS = \sqrt{\frac{\sum_{i=1}^{N} (obs_i - calc_i)^2}{N}} \tag{3.13}$$

This equation is very fast to compute and returns one number from two gravity signals, making it extremely useful. The equation compares the two signals on a pixel per pixel basis: each pixel in one signal is compared with the corresponding pixel in the other signal. For data on a fixed grid (such as the surface of Mars) this is quite useful as the spatial position of the data does not change between the two signals. Caution must be taken when this is not the case: if one signal is identical to the other except for a shift of 1 pixel in any direction the resulting RMS will be large while the real difference between the signals is very small. Additionally, since the RMS is computed over the entire signal, a low RMS value could mean most of the signal is the same but one region shows stark differences or that the entire signal differs by some uniform amount. For these reasons the global RMS, while being a very useful indicator, should not be used as the only judgement of a model's performance.

A supplement to the global RMS is the central point residual. This is simply the value of the residual at the geometric center pixel of the spatial domain being investigated. This is shown in Equation 3.14, where x and y are the horizontal and vertical coordinates of the residual array res.

$$res_{centralpoint} = res\left(\frac{x_{min} + x_{max}}{2}, \frac{y_{min} + y_{max}}{2}\right) \tag{3.14}$$

This is also an easy calculation that yields one number to judge the quality of a model. Due to the nature of choosing a single point, it is not useful at all when comparing large areas with various topographical features in them. The residual value of a point between two mountains says little about how well the model fits the mountains, for example. However, this is very useful in regional analyses, when a smaller area which is focused on one geographic feature is being studied. For example, a model fitting an area defined as a 40km radius circle around one volcano might be better judged by the central point residual than by the RMS of the entire area as the former takes only the center of the volcano into account. Due to this the central point residual, as with the global RMS, should not be used as the sole judge of a model.

3.6. Degree variance

When dealing with functions in spherical harmonic form it is useful to examing their degree variance. This is a measure of the strength of the signal per spherical harmonic degreee. The equation for the degree variance is given by Equation 3.15 (Wieczorek and Simons (2007)), where C_{nm} and S_{nm} are the spherical harmonics coefficients as seen in Chapter 2. A comparison of the degree variance of two signals can lead to insights into what degrees (and thus what spatial domain feature sizes) are more strongly modelled in each signal.

$$\sigma(n) = \sum_m C_{nm}^2 + S_{nm}^2 \tag{3.15}$$

4

Methods & Validation

In order to investigate the research question the results of a large amount of models will be compared with the observed gravity field on Mars. This is done via a software algorithm. Additionally, some of the models use localization windows in order to allow lithospheric parameters to vary. The regions created The working and validation of the software algorithm will be presented here.

4.1. Localization windows

Based on the discussions of the topography and Bouguer plots in previous chapters it is possible to identify several areas of interest on Mars. These are areas are either large topographic features or gravity anomalies in the Bouguer signal. It is likely that the subsurface in these regions differs from that on the rest of the planet, meaning they may be best modelled with different lithospheric parameters than the rest of the planet. The areas selected for analysis are shown on Figure 4.1 and listed below:

- **The dichotomy halves** are the largest feature of Mars. Both halves have their own clear gravity anomalies, pointing towards two different global subsurface structures or mass distributions.
- **A: Hellas Basin** is an extremely large positive anomaly. There is far more gravity here than topography can account for, giving evidence for a positive subsurface mass anomaly.
- **B: Argyre Basin**, for the same reason as Hellas Basin.
- **C: Isidis Planitia** also shows a large positive mass anomaly, but unlike the large basins has no corresponding topography, meaning that the mass anomaly is fully underground.
- **D: Utopia Planitia**, for the same reason as Isidis Planitia.
- **E: Elysium Mons** has a negative gravity anomaly but a positive topography, meaning there is less gravity than the volcano can account for.
- **F: Olympus Mons** is an extremely large volcano with a significant positive gravity anomaly. Due to its size it will be included as an area of interest.
- **G: Alba Mons** is a strong negative signal in the Bouguer anomaly, despite being a large volcano.
- **H: The Tharsis bulge** as a whole does not have a clear signal, but due to its size and many large features will be included as an area of interest.
- **I: Valles Marineris** is a very long but relatively narrow feature, which is strongly visible in the Bouguer anomaly.

These areas include all of the large features on Mars. Figure 4.1 shows where these areas are located. Positive, negative, and zero topography areas are all included in the selection. Some of the selected regions overlap, which is an issue when they are used together in a model. This is dealt with by treating the larger region as the background and placing the smaller region inside it. A window can be any arbitrary shape, but Wieczorek and Simons (2007) state that circular shapes are associated with the lowest error. All windows in this study with the exception of the dichotomy are circles, although as regions are overlayed onto each other non-circular regions appear. Due to this, some features fit their regions much better than others: a volcano fits nicely in a circle, but Valles Marineris does not. This will be taken into account when performing the visual inspection and discussion of the results of the regional analyses.

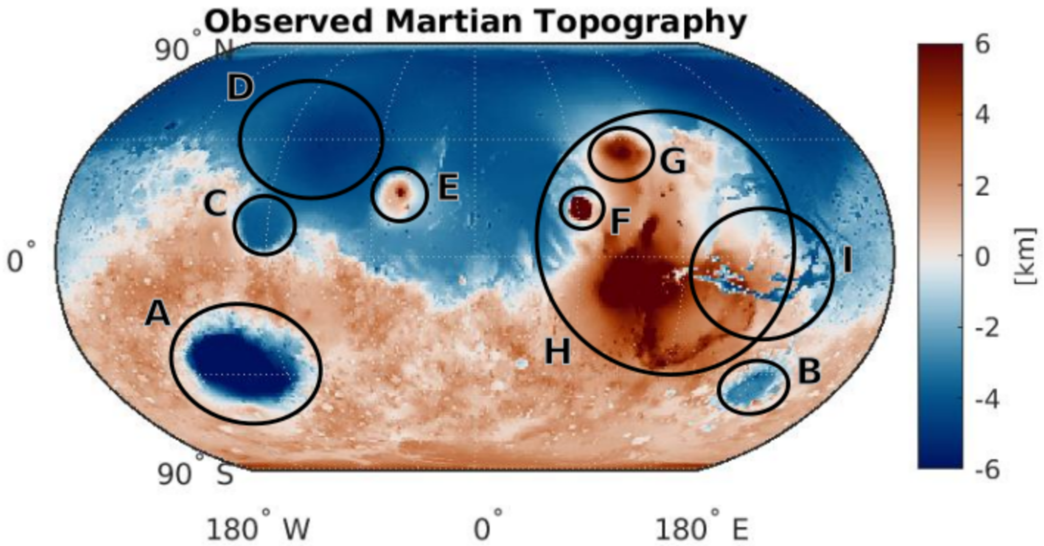

Figure 4.1: Locations of the selected areas of interest on Mars. Each area will get a window function that isolates it for regional analysis.

A plot of the window of each region along with information on how they are created can be found in Appendix A. The dichotomy windows will be treated in this here as they are more difficult to create. This is because the dichotomy boundary is both not precisely defined and decidedly non-circular. The dichotomy window is created by selecting all pixels in the topography signal that are greater than zero and then adding many small window functions to the signal until the desired shape has been created. The result of this is shown (in the spatial domain) in Figure 4.2. The figure is a plot of the final mask, where each pixel is binary. The mask for the one half of the dichotomy is created by inverting the mask of the other half.

Figures 4.3 and 4.4 show the results of the northern and southern masks being applied to an arbitrary Airy lithosphere-asthenosphere boundary depth profile. The resulting signal, for both figures, is unchanged in their respective half of the dichotomy and zero in the other half. The boundary of the masks are not smooth, and in many places follow local topography very closely. This goes against the findings of Wieczorek and Simons (2007) who states that circular caps introduce the lowest error into the signal. Despite this, validation testing presented in this chapter showed that the error introduced by this dichotomy mask is negligible, and so the boundary was left as it is.

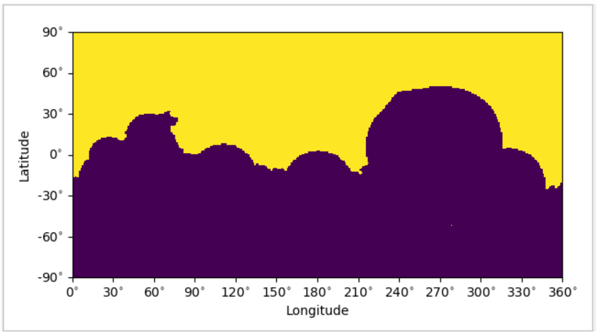

Figure 4.2: A plot of the northern dichotomy mask in the spatial domain. This mask was created by taking all points where the topography is positive and adding several small windows to the resulting signal until the desired shape is achieved. A mask is a binary signal, so the southern mask is an inversion of the northern mask.

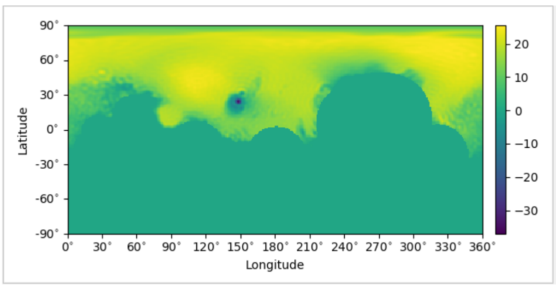

Figure 4.3: The northern dichotomy mask applied to an arbitrary Airy lithospheric thickness profile. The signal is untouched in the northern half of the dichotomy, while the southern half is zero.

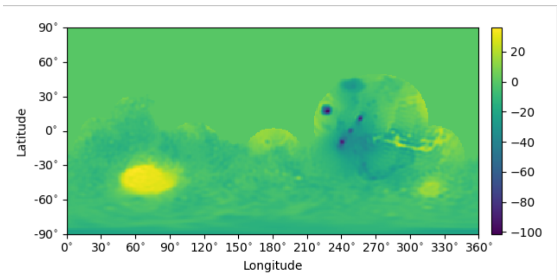

Figure 4.4: The southern dichotomy mask applied to an arbitrary Airy lithospheric thickness profile. The signal is untouched in the southern half of the dichotomy, while the northern half is zero.

4.2. Software algorithm

A software algorithm for creating and testing models was created. The algorithm is mainly in Matlab, but a part of it is written in Python. A diagram of the algorithm can be seen in Figure 4.5. Each box in the figure corresponds to a file in the software algorithm.

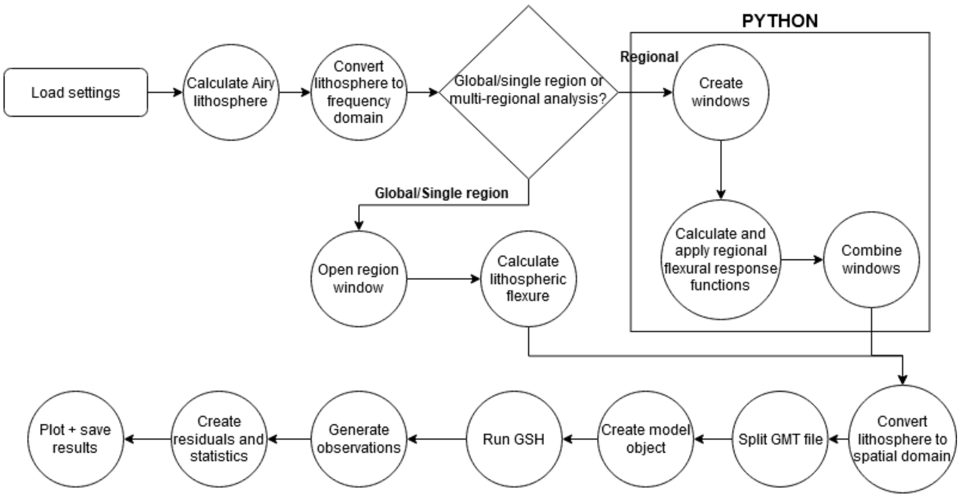

Figure 4.5: The software algorithm used in this study in order to investigate the flexure models shown in Chapter 3.

The algorithm begins with an array containing the topography of Mars as discussed in Chapter 2. This array will be used to generate a a lithosphere profile via the Airy isostatic model. The lithosphere profile will be modified by a flexure model. The gravity signal of the profile will then be calculated using the Global Spherical Harmonic (GSH) software and compared with the Bouguer anomaly of Mars. A residual will be taken and some values will be saved, after which all the results will be plotted and saved.

The GHS software is a software tool that calculates the gravity signal of a given geological layer profile (Root et al. (2016)). It is an extensive tool that forms the basis of this study. Any number of layers can be specified and each can be given a different density. Figure 4.6 (Root et al. (2016)) shows a flowchart of the GSH algorithm. For detailed information on how the GSH software works, please see Root et al. (2016). In this study there are two uses for this software. The first use is to calculate the gravity signal of a lithosphere profile. The second use is to generate the gravity signal of topography, which is done by creating a profile with the topography as the sole layer and inputting it into the GSH.

The algorithm begins by loading a settings file which contains constants and lithospheric properties (see Chapter 2). This file allows for a central location for the overview and modification of the input parameters (for the global analysis, the regional analysis has more inputs in the python environment). The file also contains run-dependent parameters such as the desired SH degrees to be used, the lithospheric elastic thickness T_e to be used, the average lithospheric thickness t_{avg} to be used, and the crustal and mantle densities ρ_c and ρ_m to be used. These parameters are carried through the algorithm and used when needed.

The Airy lithosphere is then calculated. The root is calculated using Equation 3.2, after which the average lithospheric thickness is added. This is shown in Equation 4.1, with M_{airy} being the depth of the lithosphere-asthenosphere boundary as calculated by the Airy model.

$$M_{airy} = t_{avg} + \frac{h\rho_c}{\rho_m - \rho_c} \tag{4.1}$$

The next step is the conversion of the lithosphere from spatial to spherical harmonics domain. This results in an array of coefficients fully representing the lithosphere profile. This is done exactly the same as with gravity: any spherical dataset can be transformed into spherical harmonics, gravity is just one example.

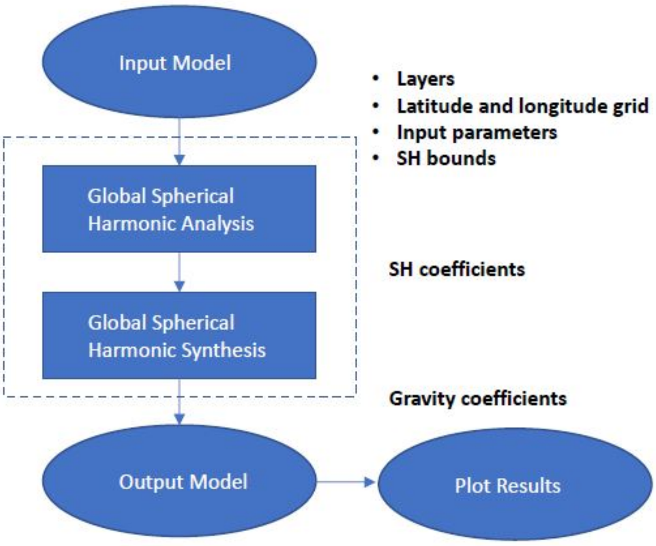

Figure 4.6: Diagram of the GSH software created by Root et al. (2016)

After this, there are two paths the algorithm can take. One is for global analyses or analyses of a single region, and the other is for multi-regional analyses. This is because the multi-regional analyses must be done using the pyshtools package in Python, while the rest of the algorithm is in Matlab. If the analysis is global or for a single region, then the next step is to load the corresponding window. This is done based on the name of the run in the settings: each region has a corresponding name. For a full list of regions, see Appendix A. The window is then multiplied with the spherical harmonic form of the lithosphere profile. This modified lithosphere profile is then multiplied with the flexural response function of the flexural model being applied (see Equations 3.7 and 3.10). Which model is being used in this run is also in the settings.

For multi-regional analyses the settings parameters and the spherical harmonics form of the lithosphere profile are passed to the Python segment of the code. There are two multi-region analyses available: a dichotomy analysis with two regions, and a 'global' regional analysis with all regions combined. Once again, which analysis is being done is determined by the settings file. For each analysis the regional parameters (T_e, t_{avg}, etc) are stored in the python environment: modifying them requires editing the python code. The corresponding regions for the analysis are created and each one is multiplied with the spherical harmonic form of the lithosphere profile. Each profile is then multiplied by its flexural response function, after which all the regions are recombined. The recombined lithosphere profile is then passed to the Python environment.

After this, the algorithm is the same for all analyses. The lithosphere profile is converted back to the spatial domain. This lithosphere profile is complete: all models have been applied to it. Some steps have to be taken before the GSH can be run, however.

The first of these steps is to split the lithosphere profile into several layers. This is needed as the way the GSH processes the profile means that layers of over 25km thickness cause significant errors to be introduced into the resulting gravity signal. The solution is to transform the lithosphere profile from one layer (from the surface to the lithosphere-mantle boundary) into a series of 25km thick layers of equal density. Physically the two are identical, but computationally several smaller layers are necessary.

The second of these steps is to create a 'model' object in matlab. This object is used by the GSH during its calculations, much like the 'settings' object is used in this algorithm. Some information in this object includes physical parameters of Mars (radius, gravitational parameter, etc) as well as a list of all the layers in the lithosphere profile along with the corresponding densities. Each layer is specified as a filepath in this object, meaning the newly split layers must all be saved.

With the 'model' object and the completed lithosphere profile the GSH can now be run. The inputs to it are the 'model' object and the lithosphere profile. The outputs are the gravity signal of the lithosphere profile, both in spherical harmonic and in spatial domain form. These outputs are the calculated gravity signal of the subsurface, which must now be compared with the observed gravity signal of the subsurface of Mars.

The observed gravity signal of the subsurface of Mars is taken as the Bouguer anomaly (see Chaper 3). This is not strictly true, as the Bouguer anomaly is the observed gravity, minus the central terms, minus the signal of the topography. What is left is assumed to be the signal of the subsurface, but also includes signal from the upper mantle and other structures not included in this lithosphere profile. Further discussion on this can be found in Chapter 6.

The next step is then to generate the Bouguer anomaly of Mars. This is done as outlined in Chapter 3 using the parameters given in the settings. An outline of the settings file is shown in Appendix C. This is done fully in the spatial domain, as there is no need for spherical harmonics in this process. After this, the observed and calculated signal can be directly compared. This is done as shown in Chapter 3 via a residual, the calculation of a global RMS value, and, for some regions, a central point RMS value. However, one of the more important judgement of the quality of the results is the visual inspection. This leads to the last step in the algorithm.

The final step is the plotting and saving of the calculated signal, the observed signal, and the residuals. All statistical parameters are also saved. The calculated and observed signals themselves are also saved along with the plots. This concludes the running of the algorithm.

The software algorithm in Figure 4.5 is capable of creating a flexural isostasy model for any combination of the input parameters seen in Chapter 2. Additionally, the user can choose between a global or regional analysis, with any combination of regions being possible in the regional analysis. The spherical harmonics bounds can also be set by the user. This is very useful as the degree 1 terms include the dichotomy signal, meaning that it can be included or excluded. Additionally, it is known that flexure acts mainly on large scale features as smaller topographic features are usually not a heavy enough load to affect the subsurface (Wieczorek and Zuber (2004)). To investigate the effects of flexure it is thus desirable to investigate the lower degrees of the gravity signal. Due to these reasons the following spherical harmonic bounds will be investigated in this study: 1:90, 2:90, 1:10, 2:10, 1:20, and 2:20.

Having said this, the regional models will always be run using the degree 1 terms, meaning that only half the runs are required in total. The opposite is true for the global models: they will always be run excluding the degree 1 terms. This means that the global models will be run with three sets of bounds 2:90, 2:10, and 2:20 while the regional models will be run with the three sets of bounds 1:90, 1:10, and 1:20. This is because the degree 1 terms are the dichotomy signal, which affect different parts of the planet differently. Global models use one set of lithosphere parameters for the entire planet, meaning that it is impossible to incorporate the regionality of the dichotomy signal into the model. Additionally, the signal of the dichotomy will be very strong as it is not fit well, and will likely overpower and obscure the signal of the topographic features we are examining. Models examining one region or a group of regions do not have this problem, and so removing the dichotomy signal in these models would only be removing information for no gain in performance or model accuracy.

The average lithospheric thickness t_{avg} and the elastic lithospheric thickness T_e (as described in Chapter 3) are the two inputs to the models that will be investigated in this study. These parameters also the focus of most subsurface studies in literature (Wieczorek (2015)). The three models in this study (Airy, infinite plate, and thin shell) will be presented with a range of t_{avg} and T_e values in order to find the best fits. Many studies have estimated these values for various regions on Mars, but there is no clear consensus as to their value (Wieczorek (2015)). The ranges used in this study are:

- T_e (km): 0, 10, 20, 40, 80, 120, 160, 200, 300, 400
- t_{avg} (km): 40, 80, 120, 160, 200, 300, 400

For the T_e values, a starting value of zero was chosen as this is the lowest possible value. Remembering the flexural response functions described in Chapter 3, a T_e of zero reduces both flexure models to an Airy model. The spacing between the chosen T_e values is not uniform. This was done because the effects of raising T_e diminish as its value increases due to the flexural response function being the reciprocal of the value calculated with the T_e. Thus a higher resolution at low T_e values and a lower resolution at high T_e values will effectively search the entire space.

The t_{avg} values begin at 40km and not at zero. Initial tests with the Airy model showed that this is the smallest average lithospheric thickness for which no part of the Lithosphere has a negative thickness after the Airy calculation. The flexure models allow for a slightly lower average thickness but, unless extremely high T_e values are used, never lower than 35km. The spacing between t_{avg} values is even up to 200km, at which the spacing becomes much sparser. This is because the a thicker t_{avg} results in a deeper lithosphere-asthenosphere boundary. As the gravity signal of mass is based on the distance of the mass squared, a doubling of the depth of the boundary leads to four times less gravity signal from the boundary. This leads to the same situation as with the T_e values, where a coarse spacing is acceptable for higher values.

4.3. Software Validation

The validation of the methods used in this study consists of validating four intermediate products: the Bouguer anomaly, the infinite plate model, the thin shell model, and the localization functions. For each of these products a result from literature is compared to an equivalent result from this study.

The Bouguer anomaly as calculated by Genova et al. (2016) is shown in Figure 4.7. The Bouguer anomaly computed in this study is shown in Figure 4.8. The two plots are created with a colorbar ranging from -600 to 1000 mGal. It was not possible to use the same colorbar as Genova et al. (2016) due to the custom colorbar used by the author. Despite this, careful inspection of the two figures shows that they are identical. This is relatively easy to see in the large features such as Hellas and Argyre basins and Isidis and Utopoa planitia. However, a look at smaller features reveals matches around the tharsis bulge, in the northern plains, and around Elysium mons. I suspect that the colorbar of Genova et al. (2016) was chosen to maximize the visbility of small gravity signals, as values between -100 and 100 mGal go through three colors, while the values -600 to -100 and 100 to 500 have the same color.

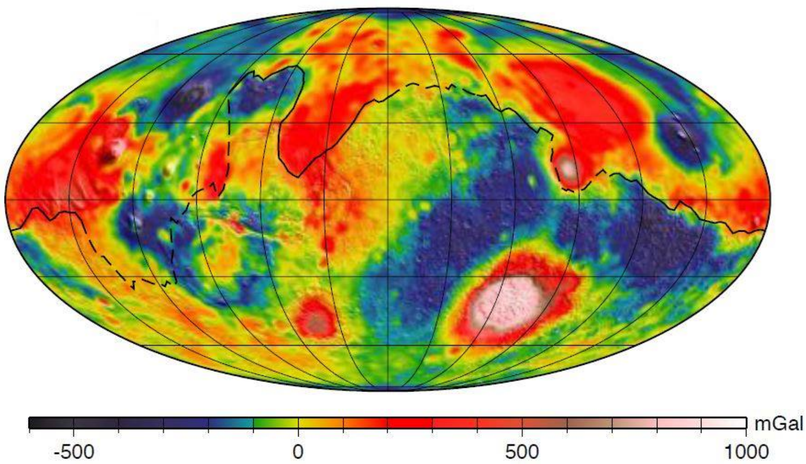

Figure 4.7: Global Bouguer anomaly (Genova et al. (2016)).

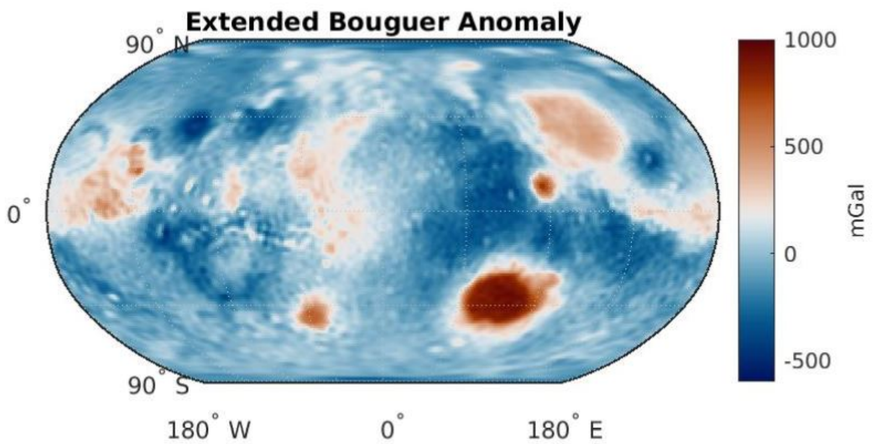

Figure 4.8: The extended Bouguer anomaly of Mars, using spherical harmonic degrees 2 to 90 and with $C_{2,0} = 0$. This figure is equivalent to Figure 4.7 but has been created in this study. The colorbars do not match due to the custom colorbar used by Genova et al. (2016).

Verification of the infinite plate model is done by comparing the results of models in this study to the reusults of the models in Veldhuizen (2019). Figure 4.9 shows the global RMS value of the residual of the Bouguer anomaly minus the calculated gravity signal of a family of infinite plate models for spherical harmonic degrees 6 to 110. The models consist of three groups of varying t_{avg}: 45km (blue), 50km (red), and 55km (yellow). Each group contains models who's T_e ranges from 40km to 100km. Figure 4.10 is a reproduction of the results of Veldhuizen (2019) using models generated in this study.

A comparison of the two figures shows that although the two are extremely similar, some small differences exist between the RMS of the models of Veldhuizen (2019) and those of this report. There is an offset of 3mGal between the two plots and the position of the three lines relative to eachother are very slightly different. There are two causes of these differences. The first is that Veldhuizen (2019) uses a slightly different layering of the topography as input to the GSH when calculating the extended Bouguer anomaly. It has been my experience in this study that the GSH is relatively sensitive to the layering of the input lithosphere. Information on why can be found in Root et al. (2016). Secondly, Veldhuizen (2019) used spherical harmonic degrees up to 110 in his study, while this study generally uses up to degree 90. While an exception was made for this comparison and the maximum degree was raised to 110, it is likely that the scaling down of the MOLA topography data by Veldhuizen (2019) was done up the spatial equivalent of degree 110, while in this study it was done to the spatial equivalent of degree 90. This results in a slightly higher topography resolution in the study of Veldhuizen (2019), which is inputted into the GSH as a lithosphere profile.

Due to this, further validation of the infinite plate model will be done using plots of the results of individual models.

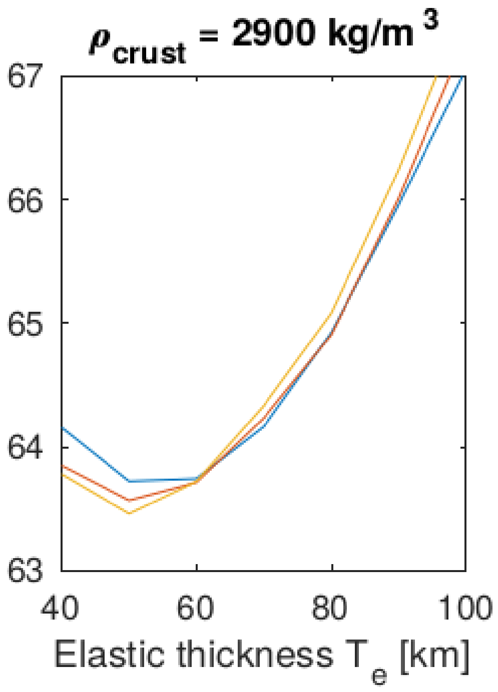

Figure 4.9: The global RMS value of the residual of the Bouguer anomaly minus the calculated gravity signal of a family of infinite plate models for spherical harmonic degrees 6 to 110. The figure is taken from Veldhuizen (2019). The models consist of three groups of varying t_{avg}: 45km (blue), 50km (red), and 55km (yellow). Each group contains models who's T_e ranges from 40km to 100km.

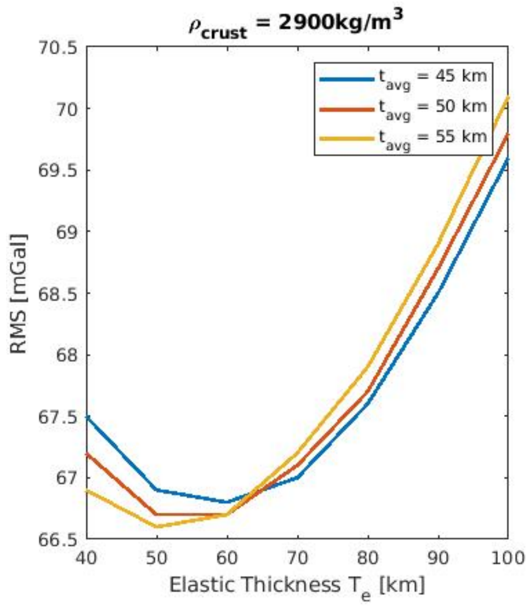

Figure 4.10: This figure reproduces Figure 4.9 using the same method and t_{avg}, T_e values, but with the results coming from the software created in this study.

Figures 4.11, 4.13, and 4.15 on the left show the observed gravity, the gravity of the best fitting model at a Te of 50km, and the residual of the two respectively. These plots were taken from Veldhuizen (2019). The 'best fitting model' from Rick is not explicitly stated: an average thickness is given as 30-100km. Figures 4.12, 4.14, and 4.16 on the right each correspond to the plots made by Veldhuizen (2019) and come from an equivalent model in this report. An average thickness of 55km was chosen based on the discussions given by Veldhuizen (2019).

A visual comparison of these six figures shows that any differences between them are very small and difficult to spot even with an identical colorbar. The most notable differences are found around Valles Marineris and Hellas basin in Figures 4.15 and 4.16. This supports the previously stated error source from the different layering structure used as input to the GSH, as these two features have significant negative topography. As a final check, the degree variance of the signals in the study of Veldhuizen (2019) and in this study will be compared.

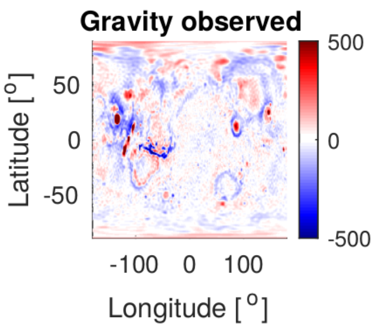

Figure 4.11: Gravity observations to benchmark the best fitting infinite plate model in the report of Veldhuizen (2019). The image comes from his report. Spherical hamonic degrees 6:110 were used to make this image.

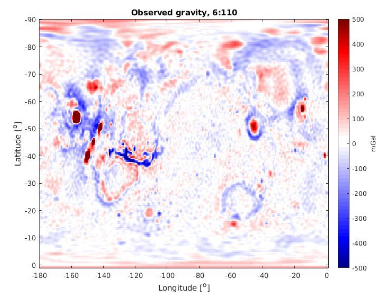

Figure 4.12: A gravity observation generated using the same parameters and colorbar as Veldhuizen (2019) in Figure 4.11.

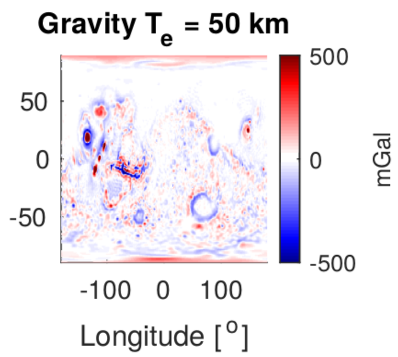

Figure 4.13: Results of the fitting infinite plate model in the report of Veldhuizen (2019). The image comes from his report. Spherical hamonic degrees 6:110 were used to make this image.

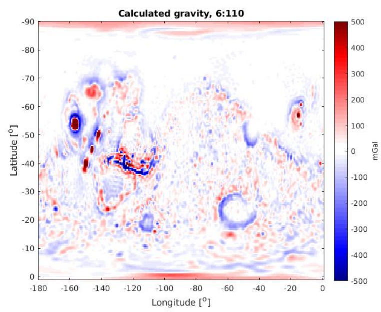

Figure 4.14: The results of a model generated using the same parameters and colorbar as Veldhuizen (2019) in Figure 4.13.

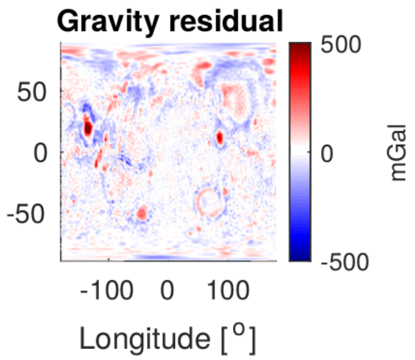

Figure 4.15: Residuals of the observations and the best fitting infinite plate model in the report of Veldhuizen (2019). The image comes from his report. Spherical hamonic degrees 6:110 were used to make this image.

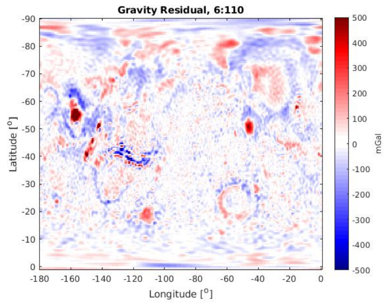

Figure 4.16: Residuals generated using the same parameters and colorbar as Veldhuizen (2019) in Figure 4.15.

Figure 4.17 shows the degree variance of several gravity signals from the study of Veldhuizen (2019). Figure 4.18 shows the degree variance of the same signals calculated in this study. Once more the two plots look very similar. In the low degrees the signals are identical execept for the extra low degrees plotted in this study. A small difference can be seen in the high degree terms. There is a small but noticeable divergence after about degree 60. These degrees correspond to small features in the spatial domain, and are once again evidence that the higher resolution topography used by Veldhuizen (2019) is a significant contributor to the differences between his results and the results from this study.

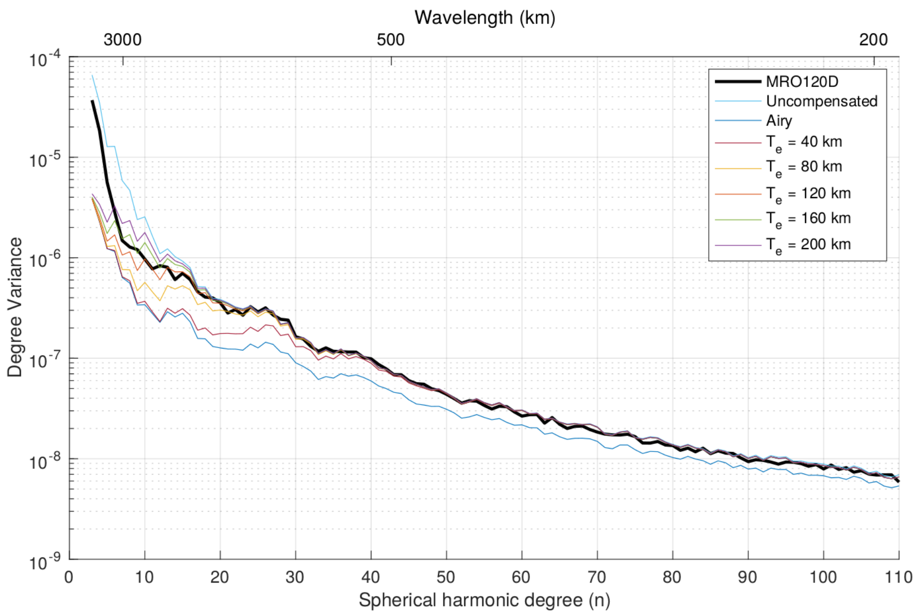

Figure 4.17: The degree variance of the observed, uncompensated, Airy, and various model output gravity signals in the study of Veldhuizen (2019). The models are infinite plate models with a T_e of 40 to 200km. All signals are plotted for a spherical harmonic range of 3 to 110.

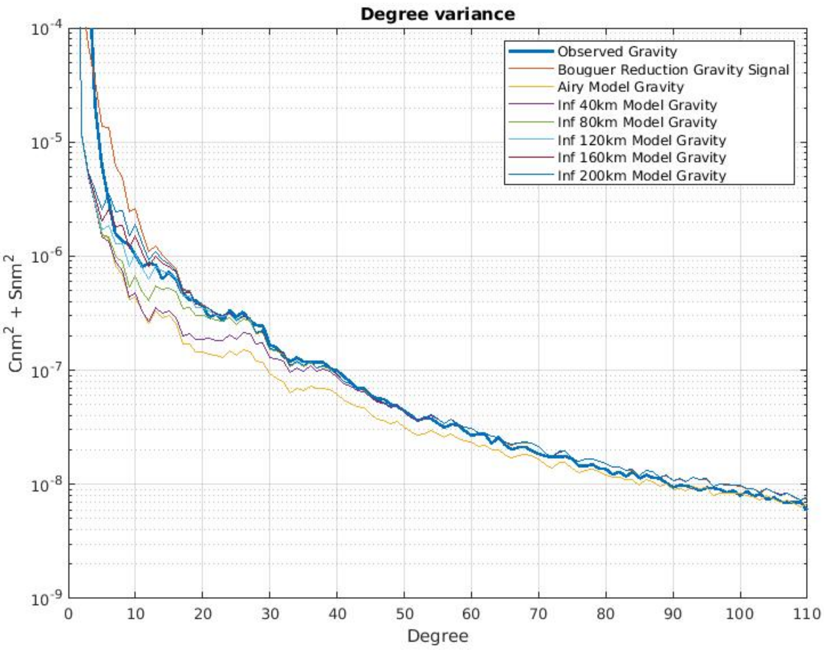

Figure 4.18: The calculated degree variance in this study of the same gravity signals as Figure 4.17.

The thin-shell model is difficult to validate with literature as there is no source which uses exactly the same methods in this study, as explained in Chapter 1. It is thus necessary to settle with studies that use similar methods and discuss the results of a comparison of that study and this one. These similar methods also use a thin shell model to calculate subsurface topography, but the type of thin shell model used is different.

Grott and Wieczorek (2012) presents a thin-shell model applied to a single volcano, Tyrrhena Patera. The thin shell model is the not the same as the one in this study and comes from Turcotte et al. (n.d.). The gravity dataset used in the study is taken from *Mars high resolution gravity fields from MRO, Mars seasonal gravity, and other dynamical parameters* (2011) and is a slightly older gravity model. The topography dataset is the same, but a significantly higher resolution version is used. A localization window is used to examine only the volcano, using the same method as this study. A difference in the window technique is that low degree terms are excluded by Grott and Wieczorek (2012) in their analysis of the volcano as they want to isolate the signal of the volcano.

Grott and Wieczorek (2012) calculates the lithosphere-asthenosphere boundary deflection caused by the weight of the volcano. Figure 4.19 shows a plot from Grott and Wieczorek (2012) of the topography h and the lithosphere-asthenosphere boundary deflection w averaged over concentric circles centered on Tyrrhena Patera. Figure 4.20 is a plot of the same values created using the models from this study.

It is clear that there are somewhat significant differences between the two figures. This is to be expected as the differences between the study of Grott and Wieczorek (2012) and this study are considerable. The topography signals match very well despite the differences in resolution, meaning that the load applied in both models is very similar. However, the difference between the two thin shell models used and the exclusion of lower spherical harmonic degrees by Grott and Wieczorek (2012) make it difficult to say much about the lithosphere-asthenosphere boundary deflection with much certainty. Trend in the deflection curve and the start and end points are very similar, suggesting that despite the differences the two models broadly agree with the trend in the subsurface deflection. It is also worth noting that the deflection curve from this study lies very close to the uncertainty limits of the deflection curve of Grott and Wieczorek (2012).

It is difficult to say that the thin shell model is validated by this comparison, but it is a sign that the results of the thin shell model in this study agree in general terms with the results of other thin shell models in literature. This is a good sign, as this is typically how results from different variations of similar models look when compared against each other (Wieczorek (2015)).

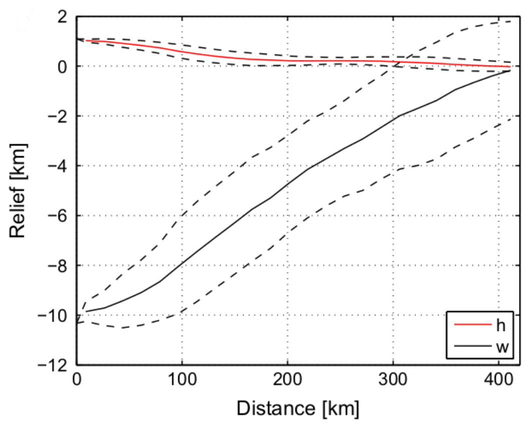

Figure 4.19: Plot of topography h and lithosphere-asthenosphere boundary deflection w averaged over concentric circles centered on Tyrrhena Patera. The dashed lines represent the uncertainty in the lithosphere-asthenosphere boundary deflection. The figure is from Grott and Wieczorek (2012).

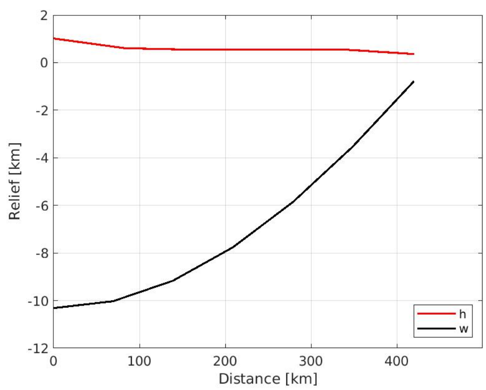

Figure 4.20: Plot of topography h and lithosphere-asthenosphere boundary deflection w averaged over concentric circles centered on Tyrrhena Patera. This figure was made with the thin-shell model presented in this study.

In order to validate the window functions described in Chapter 3 two sets of Airy models with and without windows e compared. First, a global Airy model is compared to an Airy model consisting of the two dichotomy regions as seen in Appendix A. Figure 4.21 shows an Airy model with a t_{avg} of 40km and a spherical harmonic bound of 1 to 90. Figure 4.22 shows an Airy model with the same parameters but using the two dichotomy masks. The difference between the two is minimal and only slightly visible at the boundary of the dichotomy windows. The difference in global RMS is 0.5mGal on a signal of 133mGal, which is under half a percent. This is a very acceptable amount of error to introduce into the result if it means that regional analyses are possible. This test was with only two regions. It is conceivable that adding more regions would increase this error.

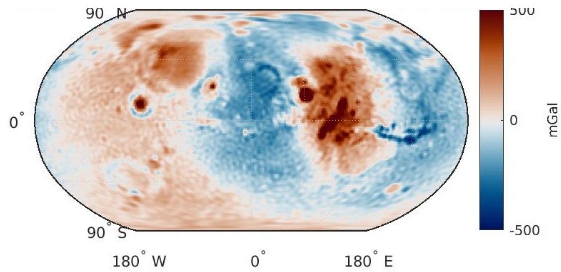

Figure 4.21: The residual map of a global Airy model with a $t_{avg} = 40km$ and a spherical harmonic bound of 1 to 90. The global RMS = 133.4mGal.

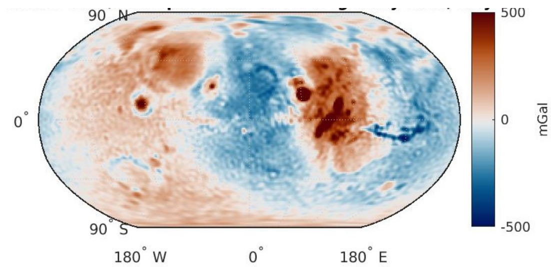

Figure 4.22: The residual map of an Airy model with two hemispheres set at identical values, $t_{avg} = 40km$ and the spherical harmonic bounds are 1 to 90. The global RMS = 133.9mGal.

A second test is performed with a global Airy model with a t_{avg} of 40km and an Airy model containing all regions as described in Appendix A. All other inputs to the model are kept unchanged for this comparison, meaning that the difference between the two should be minimal. Figure 4.23 shows an Airy model with a t_{avg} of 40km and spherical harmonic bounds 1 to 90. Figure 4.24 shows the results of the Airy model with all the regions having the same t_{avg}. Visually the two images are almost identical aside from some effects near the edge of regions, for example on the western edge of Utopia Planitia and around Elysium mons. The global RMS value of the non-regional Airy model is 133.4 mGal and that of the regional model is 134.0 mGal. That is a 0.5% error, which is not significant enough to affect the conclusions of this study. This shows that adding a relatively large number of regions into an Airy model does not introduce significant error.

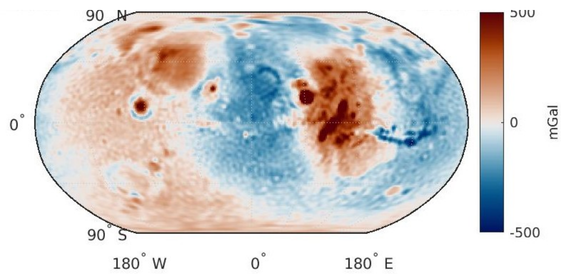

Figure 4.23: The residual map of a global Airy model with a $t_{avg} = 40km$ and spherical harmonic bounds 1 to 90. The global RMS = 133.4mGal

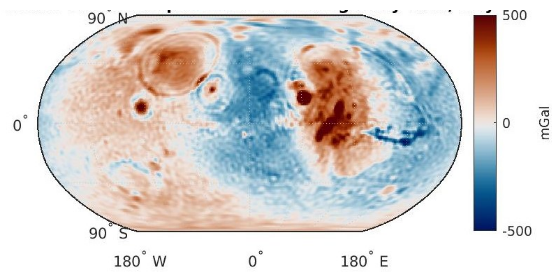

Figure 4.24: The residual map of an Airy model with all regions (as seen in Appendix A) having an average lithospheric thickness of 40km. The global RMS = 134mGal

5
Results

5.1. Bouguer model

The Bouguer anomaly serves as the observations for all the models in this study, and so requires some investigation. There will be six different spherical harmonic ranges used for analysis in this study, as said in Chapter 4. This requires six Bouguer anomalies to be used as observations. Figures 5.1 to 5.6 show the six Bouguer anomaly gravity signals for spherical harmonic bounds 2:90, 1:90, 2:10, 1:10, 2:20, and 1:20 respectively. The most notable feature in these plots is the effect of the dichotomy in the degree 1 term of the gravity field. It is also clear that taking only the lower spherical harmonic degrees smooths and removes detail from the signal. This is logical as the low degrees only capture the larger features on the planet. These significant differences between the plots show why it is necessary to vary the spherical harmonic range in flexural isostasy studies.

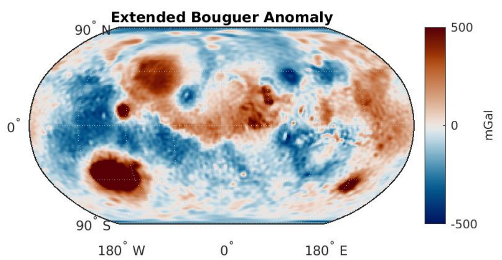

Figure 5.1: The extended Bouguer anomaly of Mars, using spherical harmonic degrees 2 to 90 and with $C_{2,0} = 0$.

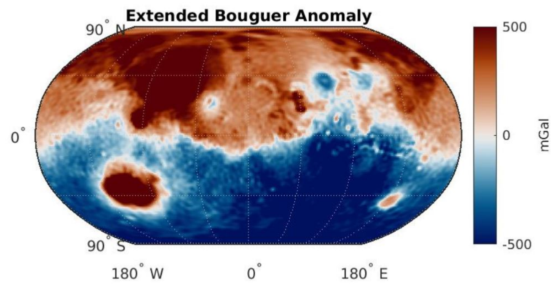

Figure 5.2: The extended Bouguer anomaly of Mars, using spherical harmonic degrees 1 to 90 and with $C_{2,0} = 0$.

Another notable feature visible in the 1:10 plots is that not all of the regions selected for analysis are visible, as some are too small. This is true of Argyre basin, Olympus mons, and especially Valles Marineris. Studies of those regions using degrees 1:10 will be done regardless, but the results may not be very useful. These features are visible in the 2:20 plots however, so their low degree signals can still be interpreted.

Some regions are also less affected by the exclusion of high degree signals than others. For example, Hellas basin is largely unchanged in all of the plots regardless of the spherical harmonic bounds chosen or the presence of the dichotomy signal. On the other hand, Elysium mons is smaller than Argyre basin, yet it is still visible (if only faintly) in all the plots. While most features become more homogeneous in the 1:10 plots, the Tharsis region retains its more chaotic appearance. This is likely partially because it is such a large area, but other large areas such as Hellas basin do not show this trend.

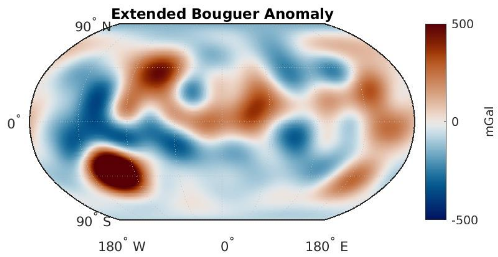

Figure 5.3: Extended Bouguer anomaly of Mars, using spherical harmonic degrees 2 to 10. $C_{2,0}$ is set to zero.

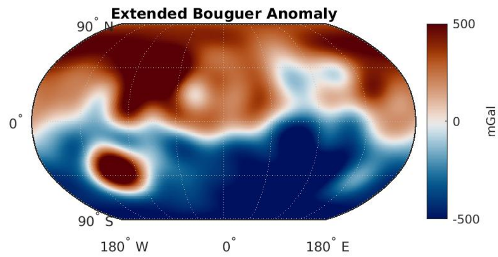

Figure 5.4: Extended Bouguer anomaly of Mars, using spherical harmonic degrees 1 to 10. $C_{2,0}$ is set to zero.

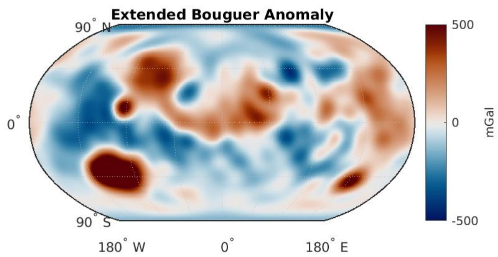

Figure 5.5: Extended Bouguer anomaly of Mars, using spherical harmonic degrees 2 to 20. $C_{2,0}$ is set to zero.

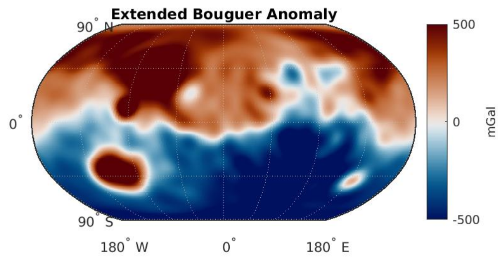

Figure 5.6: Extended Bouguer anomaly of Mars, using spherical harmonic degrees 1 to 20. $C_{2,0}$ is set to zero.

5.2. Airy based model

The first model to be tested is the Airy model as shown in Chapter 3. The calculated gravity signal of the model is subtracted from the Bouguer anomaly to obtain a residual signal. The residual signal and the RMS of the residual signal are used to interpret the results of the model.

Figure 5.7 shows the variance of the rms of the model residuals with the average lithospheric thickness used in the model. The Airy models are run for spherical harmonic bounds 2:90, 2:10, and 2:20 as explained in Chapter 4. In the figure, the best fitting Airy model still contains large anomalies for any spherical harmonic range. The best fit is for an average lithospheric thickness of 200km for the model using spherical harmonic degrees 2:90 and 2:20. For the model using degrees 2:10, the best fitting thickness shifts to 240km. The difference between three types of models increases as the lithospheric thickness increases. The fit is generally worse for models with a large SH band. Models using 2:20 have a 5-10% larger rms, and models using the full range of 2:90 have a 10-20% larger rms as compared to the 1:10 models.

Figures 5.8, 5.9, and 5.10 show the calculated gravity signals of the best-fitting model (t_{avg} = 200km) for spherical harmonic degrees 2:90, 2:10, and 2:20 respectively. In general, they look similar. For the full spectral range clear features are Hellas Basin, Tharsis, Elysium Mons, and Olympus Mons. As the spectral range is limited, only Tharsis and Hellas Basin remain as strong signals, although Elysium mons never disappears completely. Valles Marineris and Argyre basin drop out completely from the signal for the most limited spectral band. Isidis and Utopia planitias are not visible in any of the model results.

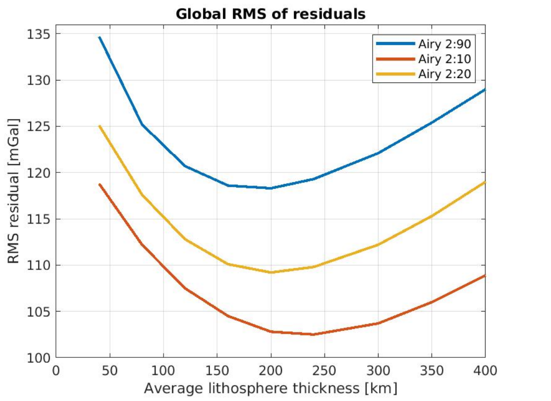

Figure 5.7: RMS variance of the Airy model residuals with a changing average lithospheric thickness.

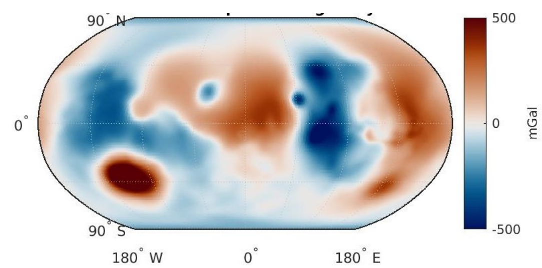

Figure 5.8: Calculated gravity signal an Airy model with t_{avg} = 200 km and $SH_{deg} = 2:90$.

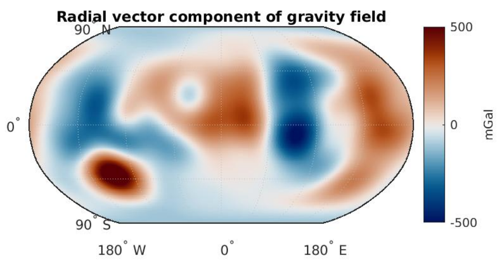

Figure 5.9: Calculated gravity signal of an Airy model with t_{avg} = 200 km and $SH_{deg} = 2:10$.

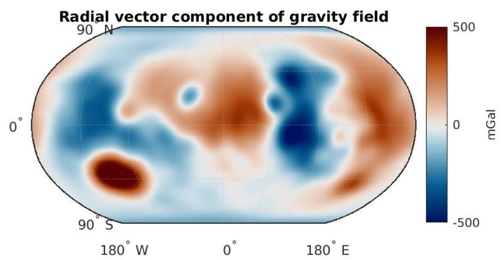

Figure 5.10: Calculated gravity signal of an Airy model with t_{avg} = 200 km and $SH_{deg} = 2:20$.

Figures 5.11, 5.12, and 5.13 show the residual of the best fitting Airy model with the corresponding Bouguer anomaly for spectral ranges of 2:90, 2:10, and 2:20 respectively. The magnitude of the signals are lower than for both the calculated Airy gravity and the Bouguer anomaly, with an RMS value of just over 100 mGal. The difference between the three figures lies mainly in the smaller features and finer detail, as these are not visible with low spectral bands. The RMS value of the 2:10 model is lower than that of the 2:20 model, which in turn is lower than that of the 2:90 model.

Compared to the full spherical harmonic range, the model using degrees 2:20 show relatively little change. In the model using degrees 2:10 there are many more changes visible. In general, geographically smaller anomalies have become weaker, while geographically large anomalies have become stronger. Areas of interest that are not visible in the full spectral range model, such as Alba mons, are also not visible in the limited range models. The Tharsis bulge loses detail, but its strength and extent remains largely unchanged across the three spectral ranges. Individual features in tharsis become less visible as the spectral range shrinks, but the signal of the bulge remains.

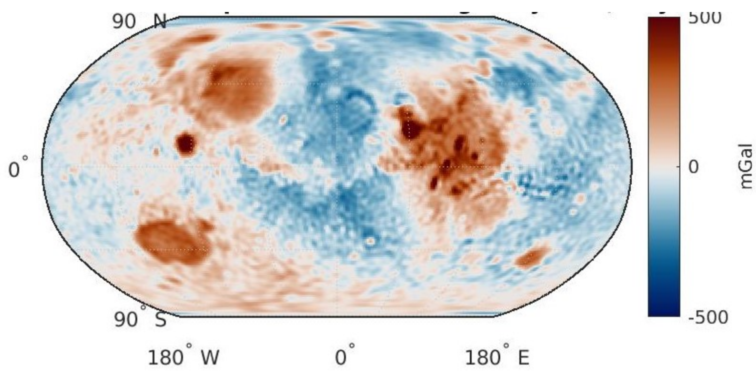

Figure 5.11: A residual plot of the best fitting Airy model, $t_{avg} = 200km$. $SH_{deg} = 2:90$. $RMS = 118.3[mGal]$.

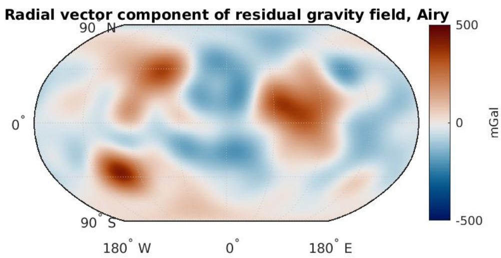

Figure 5.12: A residual plot of the best fitting Airy model with $t_{avg} = 200[km]$ and $SH_{deg} = 2:10$. $RMS = 102.8[mGal]$.

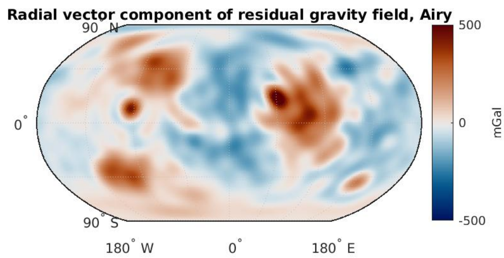

Figure 5.13: A residual plot of the best fitting Airy model with $t_{avg} = 200[km]$ and $SH_{deg} = 2:20$. $RMS = 109.2[mGal]$.

Figure 5.7 showed that the RMS value of the airy models vary significantly depending on the t_{avg} used. A low or high t_{avg} result in a higher RMS than a medium value. What the figure does not show is what the models look like at a low or high t_{avg}. This is investigated through the use of end members, which are the extremes of the models: a minimum and a maximum t_{avg}.

Figures 5.14 and 5.15 show residual plots of Airy models with the minimum and maximum t_{avg} values respectively. With a very low average depth, Figure 5.14 shows all the areas of interest except Hellas Basin and the dichotomy. Most areas of interest have a positive anomaly, with the exception of Valles Marineris. Meanwhile with a very high average depth, Figure 5.15 shows significant positive anomalies at Hellas Basin, Argyre Basin, Isidis Planitia, Utopia Planitia, and the Tharsis mountains. The Tharsis region's signal is significantly less strong in the high end member residual than in the low one. Elysium mons has a negative signal, while Valles Marineris is not visible. Many smaller topographical details are visible in the high end member residual.

To directly compare the two end members, Figure 5.16 shows the difference between the two end members. Almost all large and medium topographical features of Mars are visible in this plot. Valles Marineris, Hellas and Argyre basins, and Isidis planitia show strong negative signals. All other regions are strongly negative, with the exception of Utopia planitia which is not visible. The magnitude of the signal is significant, indicating that the choice of t_{avg} has a significant effect on the results of the model.

Figures 5.14 and 5.15 also look like the free air and the Bouguer anomaly, respectively. This is to be expected, as a very low and very high average lithospheric thickness effectively result in very high and very low compensation respectively. This is due to the proximity of the Moho to the terrain. This can also be observed in the fact that Figure 5.16 looks almost identical to the topography of Mars.

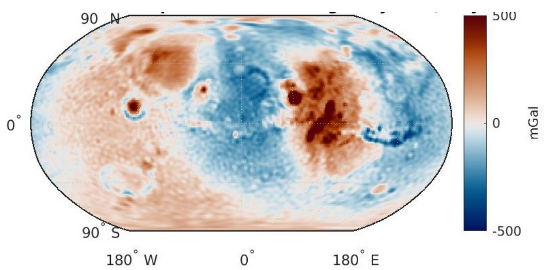

Figure 5.14: A residual plot of the Airy model with the minimum average depth. $t_{avg} = 40km$, $SH_{deg} = 2:90$.

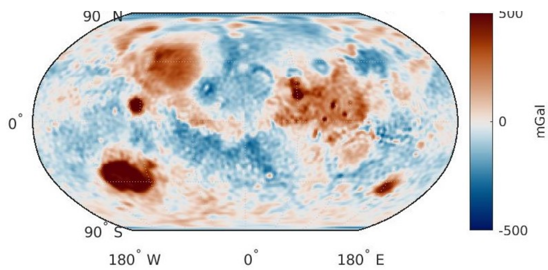

Figure 5.15: A residual plot of the Airy model with the maximum average depth. $t_{avg} = 400km$, $SH_{deg} = 2:90$.

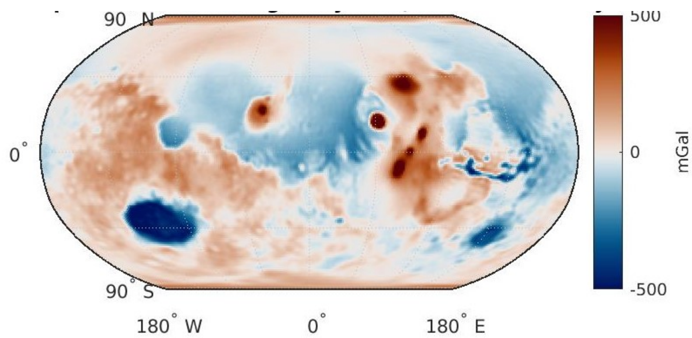

Figure 5.16: A difference plot of of the two Airy end members in Figures 5.14 and 5.15.

5.3. Infinite Plate

Figures 5.17, 5.18, and 5.19 show the variance of the RMS of the residuals of the infinite plate model with the Bouguer anomaly for spherical harmonic ranges of 2:90, 2:10, and 2:20 respectively. The global RMS of the spectral range 2:90 infinite plate model shows a minimum at an average lithospheric thickness of 200km and a lithospheric elastic thickness of 0km. The 2:10 model has a best fitting average thickness of 200km and a T_e of 0, 10, or 20km, while the 2:20 model, has a best fitting average thickness of 200km and a best fitting T_e of 0 to 10km. The magnitude of the best fit RMS decreases as the spectral range is limited, just as in the Airy results.

A lithospheric elastic thickness of zero results in an output identical to that of an Airy model. Thus, the best fitting infinite plate model is in fact an Airy model. For this reason, the best fitting infinite plate model plots are identical to those seen in Figures 5.8, 5.9, and 5.10. The same is true for the best fitting infinite plate residual plots, which are thus identical to Figures 5.11, 5.12, and 5.13.

Any flexure introduced by the infinite plate model worsens the results compared to the Airy model, although very low T_e values do not seem to affect the result. However, it must also be noted that the variance in RMS with both average lithospheric thickness and lithospheric elastic thickness is small near the best fitting value for models of all spherical harmonic bands. For example varying the average thickness from 200 km to 300 km or 120 km causes an RMS change of under 5% for all models, with the largest change happening for the spectral range 2:10. The same is true for the difference between a lithospheric elastic thickness of zero and one of 80 km. These are extremely large variations in the input parameters, yet the output is hardly effected.

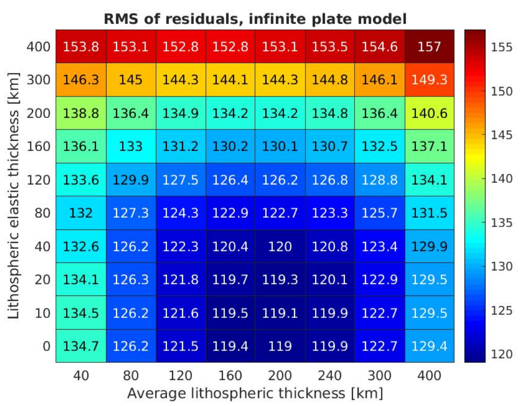

Figure 5.17: RMS variance of the infinite plate model residuals with a changing average lithospheric thickness and lithospheric elastic thickness, for a spectral range of 2:90

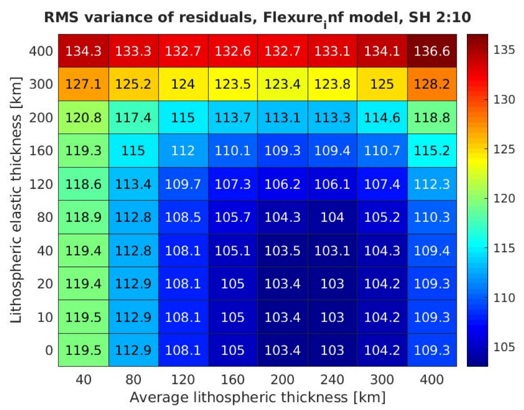

Figure 5.18: RMS variance of the infinite plate model residuals with a changing average lithospheric thickness and lithospheric elastic thickness, for a spectral range of 2:10.

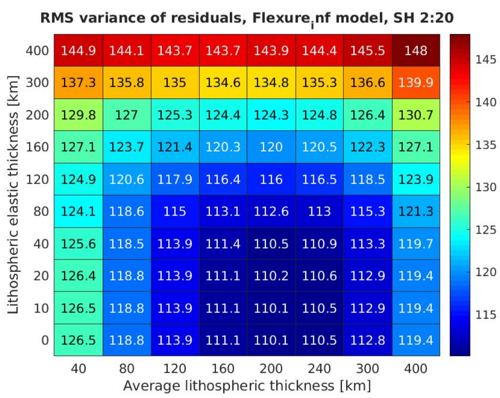

Figure 5.19: RMS variance of the infinite plate model residuals with a changing average lithospheric thickness and lithospheric elastic thickness, for a spectral range of 2:20

Figures 5.20 to 5.25 show the residual plots of the end members of the infinite plate model results for all spherical harmonic bands. To view all the end member plots individually please see Figure B.1. The end members for each parameter are created by varying one parameter while keeping the other constant. The constant parameter is a t_{avg} of 40km and a T_e of 40km. The t_{avg} is the lowest value possible, but for the T_e 40km is used instead of zero to include the flexure model in the end member, If a T_e of zero were used, then the t_{avg} end members would be identical to those of the Airy model for all models.

In the figures, the differences between plots of differing spherical harmonic bands is in the loss of small details and blurring of the signal. However, apart from that there are no real differences between the spherical harmonic bands. All areas of the planet seem to be treated equally be the smoothing effect of removing higher spherical harmonic terms. This indicates that the effects of varying t_{avg} and T_e are not dependent on the spherical harmonic band chosen for analysis. The magnitude of the effect of variations in t_{avg} is greater for the lower spherical harmonic bands as seen by the RMS of the plots. The 2:10 t_{avg} plots have a higher RMS value than the 2:20, which in turn has a higher RMS than the 2:90 plots. The opposite is true for the effect of T_e: lower spherical harmonic bands are less affected.

Comparing plots of the same spherical harmonic band shows that the effect of T_e is different from that of t_{avg}. Changes in T_e result in more small changes across the planet, especially around Tharsis, Valles Marinaris, and the dichotomy boundary. The effect is in general 'higher resolution' compared to the effect caused by varying t_{avg}. This is true for all spherical harmonic bands. In the 1:10 plot, the effect of T_e is more broken-up compared to the effect of t_{avg}. This is especially visible around the Tharsis region. Having said that, there are also many similarities between the changes caused by the two parameters. The general trend is the same for both of them: positive areas are positive in both and vice versa. The signal around all the areas of interest are consistent across the effects of both a parameters, for all spherical harmonic bounds.

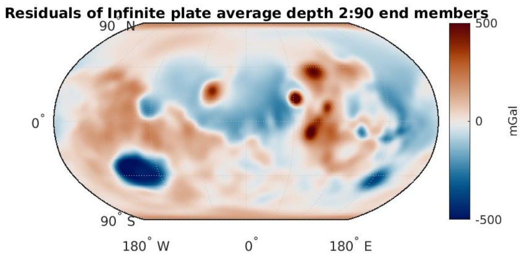

Figure 5.20: Difference plot of the two t_{avg} Infinite plate end members for a spectral range of 2:90. $RMS = 102.9$

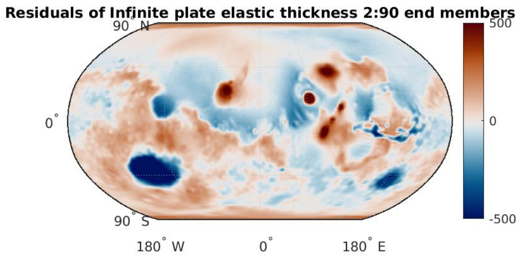

Figure 5.21: Difference plot of the two T_e Infinite plate end members for a spectral range of 2:90. $RMS = 127.6$

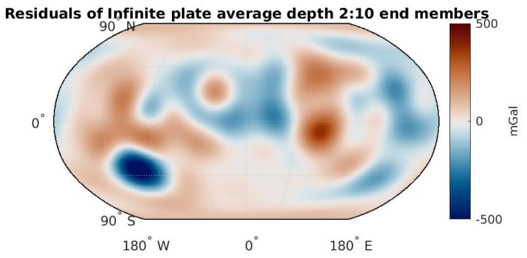

Figure 5.22: Difference plot of the two t_{avg} Infinite plate end members for a spectral range of 2:10. $RMS = 116.2$

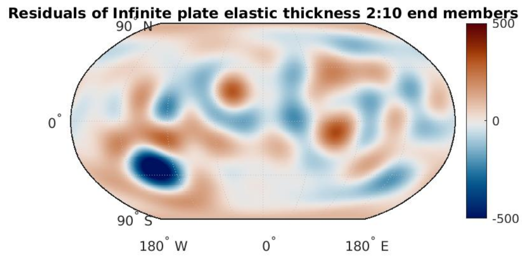

Figure 5.23: Difference plot of the two t_e Infinite plate end members for a spectral range of 2:10. $RMS = 101.6$

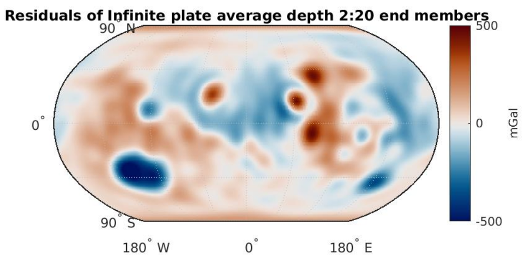

Figure 5.24: Difference plot of the two t_{avg} Infinite plate end members for a spectral range of 2:20. $RMS = 113.8$

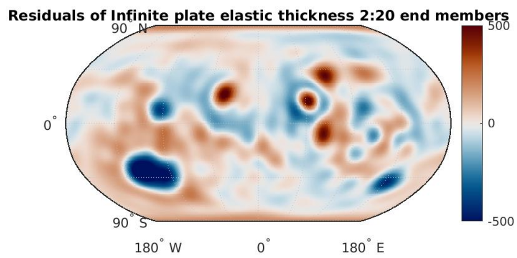

Figure 5.25: Difference plot of the two t_e Infinite plate end members for a spectral range of 2:20. $RMS = 119$

5.4. Thin shell

Figures 5.26, 5.28, and 5.27 show the RMS value of infinite plate models run for the full range of t_{avg} and T_e values. The results are similar to those found in the infinite plate model. The best fitting lithospheric elastic thickness is zero for all spherical harmonic bounds, meaning that the best fit model is an Airy model. The best fitting t_{avg} is 200km for all bounds. The 2:90 models have the lowest RMS value, followed by the 2:20 models, with the 2:10 models having the highest values. Unlike the infinite plate model, the RMS of all the thin shell models increases much faster with a higher T_e than with a higher or lower t_{avg}. Low values of T_e are strongly favored by the models, although very low values result in relatively little change in the RMS. The RMS of the thin shell models at high T_e values is higher than those of the infinite plate model at the same T_e values.

Plots of the best fitting thin shell models are identical to those of the best fitting Airy models. The result of the models can be seen in Figures 5.8, 5.9, and 5.10. The same is true for the best fitting infinite plate residual plots, which are thus identical to Figures 5.11, 5.12, and 5.13.

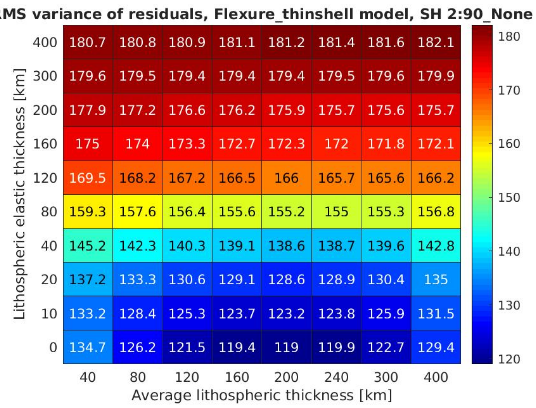

Figure 5.26: RMS variance of the thin shell model residuals with a changing average lithospheric thickness and lithospheric elastic thickness, for a spectral range of 2:90

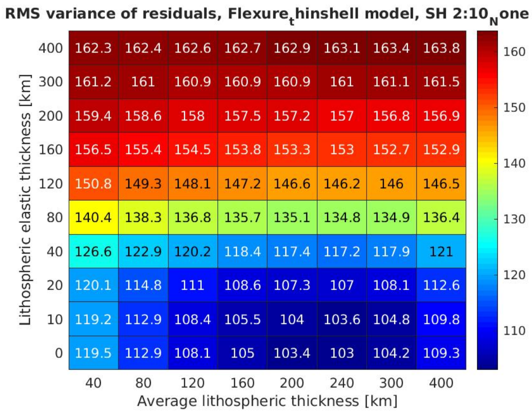

Figure 5.27: RMS variance of the thin shell model residuals with a changing average lithospheric thickness and lithospheric elastic thickness, for a spectral range of 2:10.

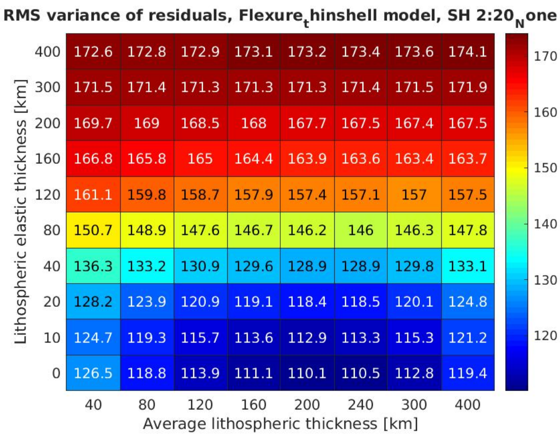

Figure 5.28: RMS variance of the thin shell model residuals with a changing average lithospheric thickness and lithospheric elastic thickness, for a spectral range of 2:20

Figures 5.29 to 5.34 show the difference of the end members for all spherical harmonic bounds and both parameters. To see all the thin shell end member plots, see Figure B.2. The effect of T_e on the thin shell model results is very significant, more so than in the infinite plate model. All spherical harmonic bands of T_e end member residual have RMS values around of 200mGal, with lower spherical harmonic bands having a lower RMS. The difference between the spherical harmonic bands is only the loss of detail and blurring in the T_e end members. The effect of t_{avg} on the thin shell model results is notably different to what was seen in the infinite plate model. The effect is of a similar magnitude, but lower spherical harmonic bands are more affected by the t_{avg} than higher bands. This is likely due to the much higher effect of T_e on the results, as the t_{avg} end members have to be performed at a certain T_e. If the T_e were zero, the results would not be interesting as they would not show the effect of flexure, but if the T_e is too high then the effect of t_{avg} cannot be seen. A T_e of 2 km was used for these difference plots, while a T_e of 40 km was used for the infinite plate difference plots.

All regions are clearly affected by varying the T_e of the thin shell model, especially in the 2:90 models. Almost all large and medium topography is visible at this full spherical harmonic range. For lower spherical harmonic ranges smaller features such as Argyre basin and Valles Marineris are no longer affected as they can no longer be resolved. Hellas basin and the Tharsis bulge are particularly affected with differences of over 500 mGal, while the rest of the surface of Mars is comparatively less affected with differences of a few hundred mGal at most.

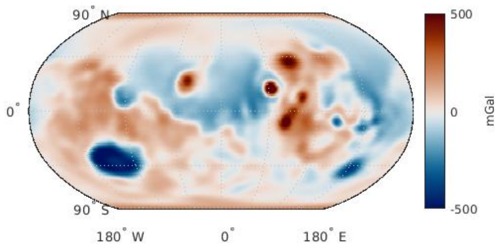

Figure 5.29: Difference plot of the two t_{avg} thin shell end members, SH_{deg} = 2:90. RMS = 119.7

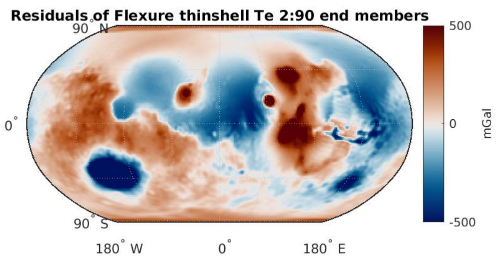

Figure 5.30: Difference plot of the two T_e thin shell end members, SH_{deg} = 2:90. RMS = 207.8

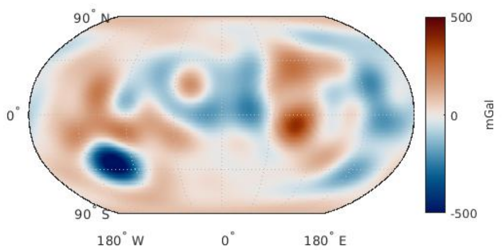

Figure 5.31: Difference plot of the two t_{avg} thin shell end members, SH_{deg} = 2:10. RMS = 103.2

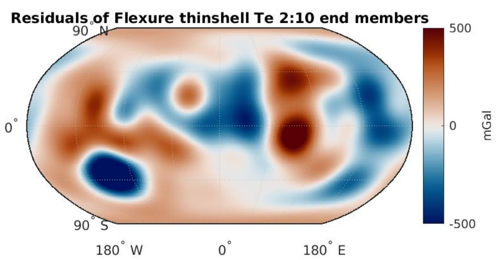

Figure 5.32: Difference plot of two T_e thin shell end members, SH_{deg} = 2:10. RMS = 190.8

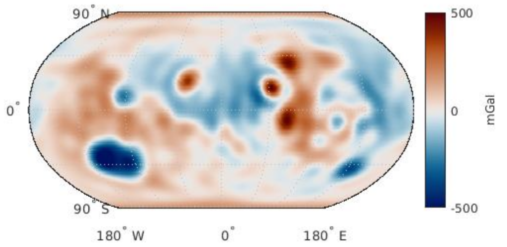

Figure 5.33: Difference plot of the two t_{avg} thin shell end members, SH_{deg} = 2:20. RMS = 115.7

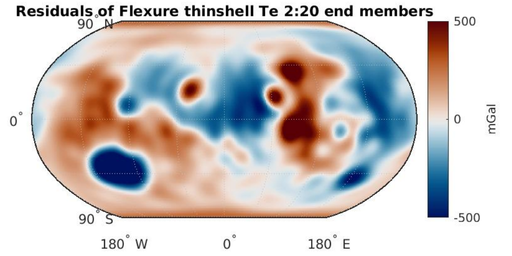

Figure 5.34: Difference plot of two T_e thin shell end members, SH_{deg} = 2:20. RMS = 202.2

5.5. Model Comparisons

The results of the models share some similarities, but also some key differences. This section will identify both of these in an attempt to fully characterize the models. The Bouguer anomaly are the observations that the models are compared against in order to find the best fit. However, the residual plots of the best fitting infinite plate and the thin shell models show a minimum RMS of 118.3 mGal for the full spherical harmonic range. Moreover, the best fitting models both have a T_e of zero, which means they are in fact the same model (an Airy model). In light of this, in order to better observe their differences the end members of the two models will be compared.

The most glaring similarity is that the Airy, infinite plate, and thin shell model all share the same best fit parameters, namely a T_e of zero and a t_{avg} of 200 for spherical harmonic bounds 2:90 and 2:20 or a t_{avg} of 240 for spherical harmonic bounds 2:10. The best fitting solution for the flexure models is thus no flexure.

A second similarity is the response of the RMS of the models to variations in T_e and t_{avg}. All models return the lowest RMS value for a certain combination of those parameters, and the RMS increases as the parameters are varied in any way. This can be seen in Figures 5.7,5.17, and 5.26. As seen in the figures, there are several combinations of parameters that can lead to the same RMS. Often a slightly lower or slightly higher t_{avg} results in the same RMS value of the model residuals. For example, at a T_e of 120 km, the infinite plate model with 2:90 spherical harmonic bounds shows a 0.5 mGal difference between t_{avg} values of 40 and 400 km .

In both the infinite plate and thin shell models, variations in T_e cause an increase of RMS two to four times larger than the increase caused by variations in t_{avg}. This shows that the models are much more sensitive to changes in T_e than changes in t_{avg}.

Similarly, the effect of variations in t_{avg} can be seen in the end members of the three models. Difference plots of the t_{avg} end members of all three models show that the effect is extremely similar both in magnitude (under 20 mGal) and in shape, by which it is meant that each area on Mars is affected equally by variations in t_{avg} for all models. As noted before, the effect looks strongly like the topography signal.

There are some key differences, however. The most notable difference is the very strong effect of T_e on the results of the thin shell model, as compared to the infinite plate model. This can be seen by comparing Figures 5.17 and 5.26. The RMS of the residuals of the thin shell model increase much faster than those of the infinite plate model as the T_e rises. This phenomenon is equally true for all spherical harmonic bounds. The T_e end members of the thin shell model show this clearly, in particular, Figure 5.30 and 5.21 have the same shape but the magnitude of the thin shell end member difference is 50% higher than that of the infinite plate.

A second difference is that the thin shell model generally shows higher RMS values for all non-zero values of T_e than the infinite plate model. This is also visible in Figure 5.30, where compared to the infinite plate plot, negative areas are more negative and positive areas are more positive.

The effect of T_e and t_{avg} on the infinite plate and thin shell model is generally similar: they both look like topography, but the effect caused by T_e variations shows more small scale features. One exception to this is at the Tharsis bulge, where the region is far more affected by the thin shell model. This is true across all spherical harmonic bands. The thin shell model generates a very strong, diffuse signal along the Tharsis montes. Meanwhile in the infinite plate model, the Tharsis montes are individually visible and there is no strong, diffuse signal.

5.6. Hemisphere Analysis

Two window functions were created to isolate each half of the dichotomy (see Chapter 4 and Appendix A). A series of Airy models was created with a certain southern lithospheric thickness and a thinner northern lithospheric thickness. The RMS of the residuals of those models can be seen in Figure 5.35. All of these models are run with a spherical harmonics bound of 1:90.

Figure 5.35 shows a minimum RMS value for a global lithospheric thickness of 120km. However, a southern lithospheric thickness of 240km and a northern lithosphere 5km thinner are very close to that, as are global thicknesses of 80, 160, and 200km. This is to be expected given the topography of the dichotomy. The best fit found with global Airy models falls within this range. Various combinations of lithospheric thicknesses yield similar results in this figure.

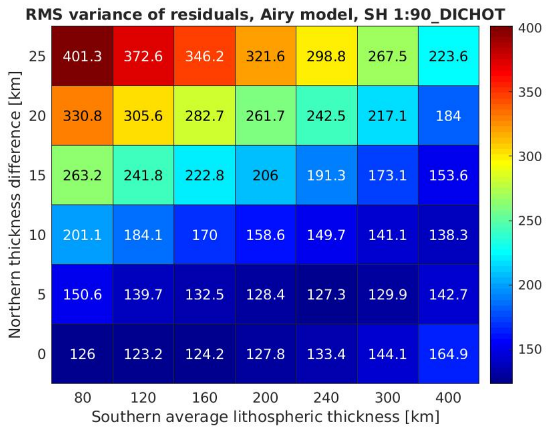

Figure 5.35: RMS of the residuals of Airy models with a southern lithospheric thickness and a thinner northern lithospheric thickness, SH_{deg} = 1:90.

Figure 5.36 shows a residual plot of a dichotomy Airy model with a southern lithospheric thickness of 240km and a northern thickness of 235km. The dichotomy signal is not visible in the figure, even though it was included in this model. This is an indication that the two Airy models in their respective window functions fit the dichotomy signal quite well. The northern RMS value is slightly higher than the southern value. In the south Hellas and Argyre basins stand out. Olympus mons has a strong signal, although Alba mons is barely visible. Isidis and Utopia planitia are clearly visible. Overall there are many strong positive signals but no strong negative signals.

5.7. Density variations

Lithosphere densities of 3100 kg/m^3 and 2700 kg/m^3 were investigated using the flexural isostasy models. The lithospheric density was used for the topography and for the lithosphere. However, the impact of changing the density was very small across all models. Figure 5.37 shows a plot of the residuals of the residuals of an Airy model (t_{avg} = 40 km) with a lithospheric density of 2700 kg/m^3 minus an Airy model of the same t_{avg} and

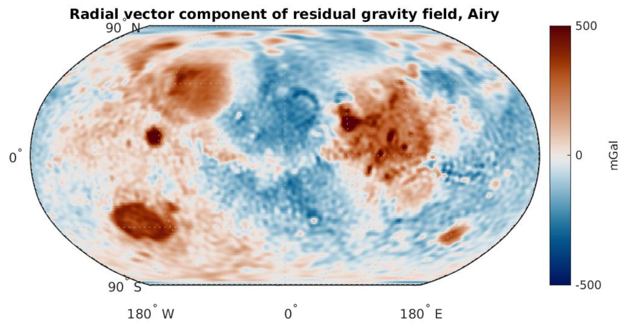

Figure 5.36: A residual plot of a dichotomy Airy model with a southern lithospheric thickness of 240km and a northern lithospheric thickness of 235km. The global RMS is 127.3, the northern RMS is 128.9, and the southern RMS is 126.0.

a lithospheric density of 3100 kg/m^3. The effect of the density on the observations (the Bouguer anomaly) is included in this figure. The RMS of this plot is 25.6 mGal, and overall the signal is very small. The effects of varying the lithospheric and load density are hardly visible in the model results.

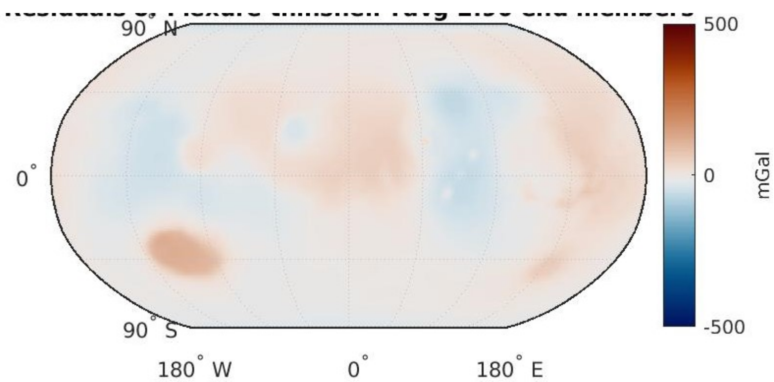

Figure 5.37: Residual of the residuals of a 2700kgm3 Airy model minus a 3100kgm3 model, 2:90. RMS = 25.6

5.8. Regional analysis

Each region selected for analysis in this study (see Chapter 4) was isolated with window functions and run through Airy, infinite plate, and thin shell models for the full range of T_e and t_{avg} values and for all spherical harmonic bounds. All regions are judged by their global RMS value and by their central point residual value. The best fitting parameters for each region and model were then combined into a series of global analyses for each of the models. An overview of the regions used can be found in Appendix A.

The full results of this regional analysis can be found in Appendix D. The best fitting values for each region and spherical harmonic band will be presented here, as well as some general remarks over the results and some specific observations about each region. After this the global analysis will be performed.

One notable result is that all regions have a manifold of best fit solutions. A region can be best fit, both by RMS and central point residual, by a number of different average thicknesses and lithospheric elastic thicknesses. This makes defining a single best fit value a matter of choosing one of the solutions. The best fitting solution chosen in this study is the one where the RMS or central point residual shows the best fitting value. This makes the chosen solution dependent on the search space used, as a finer or coarser mesh may result in a different solution. Figure 5.38 shows an example of this manifold of best fit values for Hellas basin. For a t_{avg} of 120km, there are solutions around 40 and 120 km that yield a central point residual of zero. This example is typical of what is seen in other regions.

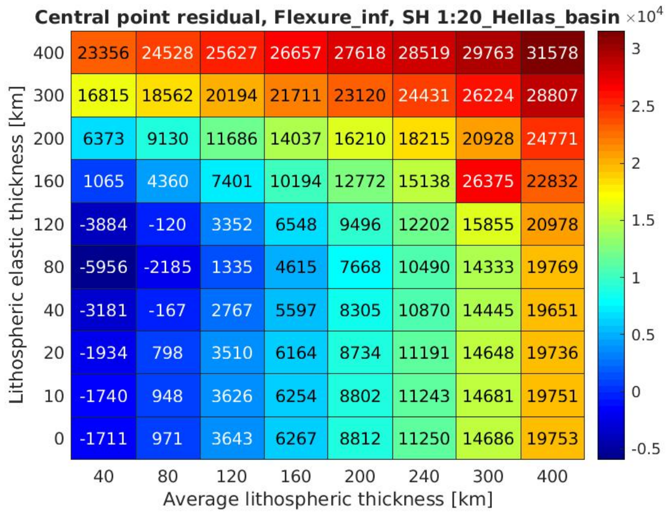

Figure 5.38: A heatmap of central point residual variance (mGal) of infinite plate model residuals of Hellas basin with a changing average lithospheric thickness and lithospheric elastic thickness, for a spectral range of 1:20

Another feature is that the differences between the infinite plate and the thin shell models observed in the global studies largely hold true for the regional studies. For example, the thin shell model is best fit by equal or lower T_e values than the infinite plate model, regardless of the region.

Tables 5.1, 5.2, and 5.3 show the best fitting models for each region by RMS and central point residual. The dichotomy windows do not have a central point residual as they are not centered on a topographic feature.

Hellas Basin: The RMS of Hellas basin is best fit by a low T_e and a low t_{avg}. This is true for all models and spherical harmonic bands. By central point residual, Hellas basin is best fit by an Airy model with a t_{avg} of 80km, an infinite plate model with a t_{avg} of 80km and a T_e of 120km, and a thin shell model with a t_{avg} of 80km and a T_e of 0 or 20km.

Argyre Basin: Argyre basin is best fit by a t_{avg} and a T_e of 400km, if the RMS value is used. This is true for all models and spherical harmonic bands. The best fit value of the RMS of Argyre basin is significantly higher than that of the other regions, meaning it is not well modelled. The central point residual value varies between models and spherical harmonic bounds, but in general a high T_e and high t_{avg} fits the region best. For the lowest spherical harmonic band the signal of Argyre is still visible, despite its relatively small size compared to the other regions.

Isidis Planitia: This region is best fit by a very low T_e and t_{avg} for all regions, spherical harmonic bounds, and choice of RMS or central point residual. The absolute value of both of these parameters are also higher than the other regions. Varying the spherical harmonic bounds hardly affects the RMS of this region, although the central point residual does vary.

Utopia Planitia: The results of utopia planitia share almost all of the same traits of the results of Isidis planitia. The differences are that neither the RMS nor the central point residual vary significantly with the spherical harmonic bound, and that all models prefer a very low t_{avg} and a small but non-zero T_e.

Elysium Mons: The RMS of Elysium mons is best fit by a both a low T_e and t_{avg}, but the central point residual is best fit by a high t_{avg} with a low to moderate T_e. The results do not vary significantly with the spherical harmonic bound. The magnitude of both the RMS and the central point residual are lower than that of the rest of the regions.

Olympus Mons: Olympus mons is best fit by an extremely high T_e and t_{avg}, often at the maximum for both by RMS. This is in contrast to the central point residual, which has an extremely large value for all models and spherical harmonic bands, but prefers a low T_e and t_{avg}. The RMS value of this region is relatively high, even for its best fit values.

Alba Mons: Although topographically similar to Olympus mons, Alba mons has a relatively low best fit RMS and is best fit by a medium to high t_{avg} and a low T_e. The central point residual values favor a low to medium t_{avg} and a low T_e. The RMS results do not vary significantly with spherical harmonic bound, but the central point results do.

Tharsis: The Tharsis region is best fit by a large manifold of T_e and t_{avg}. Almost all combinations of a high t_{avg} and a low T_e, moderate values or both, or a low t_{avg} and a high T_e are equally good fits for this region. The manifold of solutions is far larger and more pronounced in this region as compared to the others. The central point residual value is not very useful for this region, as Tharsis is very large and not centered on one topographical feature.

Valles Marineris: Just as with Tharsis, the central point residual value is not useful in this region. This is because the valley is long and thin while the region is circular, leading to most of the region being filled with non-valley area. The RMS values of this region favor moderately low values of both T_e and t_{avg}. The region has a relatively low best fit RMS value.

Region	1:90 rms	1:90 CP	1:20 rms	1:20 CP	1:10 rms	1:10 CP
North	120	-	120	-	120	-
South	120	-	120	-	120	-
Tharsis	200	400	200	400	160	400
Hellas	40	80	40	80	40	80
Argyre	400	200	400	400	400	400
Isidis	40	40	40	40	40	40
Utopia	40	40	40	40	40	40
Elysium	80	350	40	350	40	400
Olympus	400	400	400	400	400	400
Alba	200	150	240	175	400	400
Valles	80	40	40	40	40	40

Table 5.1: Best fitting average lithospheric thicknesses for Martian regions using an Airy model. Two best fitting values are given: the RMS best fit, and the CP (central point) best fit.

Region	1:90 rms	1:90 CP	1:20 rms	1:20 CP	1:10 rms	1:10 CP
North	-	-	-	-	-	-
South	-	-	-	-	-	-
Tharsis t_{avg}	200	400	200	400	200	400
Tharsis T_e	200	400	0	400	0	400
Hellas t_{avg}	40	80	80	80	40	80
Hellas T_e	0	0	0	120	0	40
Argyre t_{avg}	400	200	80	400	400	400
Argyre T_e	400	10	200	0	400	400
Isidis t_{avg}	40	40	40	40	40	40
Isidis T_e	0	40	0	0	0	0
Utopia t_{avg}	40	40	40	40	40	40
Utopia T_e	0	160	40	20	40	40
Elysium t_{avg}	80	300	40	300	40	400
Elysium T_e	40	40	40	120	0	400
Olympus t_{avg}	400	400	400	400	400	400
Olympus T_e	400	400	400	400	400	400
Alba t_{avg}	200	160	240	120	400	300
Alba T_e	0	0	0	80	40	200
Valles t_{avg}	40	40	40	40	40	40
Valles T_e	40	0	0	0	0	0

Table 5.2: Best fitting average lithospheric thicknesses and elastic lithospheric thicknesses (both in km) for Martian regions using an infinite plate model. Two best fitting values are given: the RMS best fit, and the CP (central point) best fit.

Region	1:90 rms	1:90 CP	1:20 rms	1:20 CP	1:10 rms	1:10 CP
North	-	-	-	-	-	-
South	-	-	-	-	-	-
Tharsis t_{avg}	200	400	200	300	160	80
Tharsis T_e	200	400	0	300	0	400
Hellas t_{avg}	40	80	80	80	40	80
Hellas T_e	0	0	0	20	0	10
Argyre t_{avg}	400	200	400	400	400	400
Argyre T_e	400	0	0	0	400	400
Isidis t_{avg}	40	40	40	40	40	40
Isidis T_e	0	10	0	0	0	0
Utopia t_{avg}	40	40	40	40	40	40
Utopia T_e	0	20	0	20	40	20
Elysium t_{avg}	80	400	40	300	40	400
Elysium T_e	0	400	40	0	0	400
Olympus t_{avg}	400	400	400	400	400	400
Olympus T_e	400	400	400	400	400	400
Alba t_{avg}	200	160	240	200	400	240
Alba T_e	0	0	0	0	0	40
Valles t_{avg}	80	40	40	40	40	40
Valles T_e	0	0	0	0	0	0

Table 5.3: Best fitting average lithospheric thicknesses and elastic lithospheric thicknesses (both in km) for Martian regions using a thin shell model. Two best fitting values are given: the RMS best fit, and the CP (central point) best fit.

The best fit values from Tables 5.1, 5.2, and 5.3 form a good starting point for multi-region models. The best fit as given by the global RMS value was taken. This is because the best fitting central point residual values vary significantly based on the model and spherical harmonic bound being applied, and often do not represent a better fit than the global RMS. Airy, infinite plate, and thin shell models were set up with all regions, with each region using the best fit as found in the tables above. The model resulted in impossibly large residuals, far too large to be physical. Further testing showed that variations in t_{avg} can not be larger than 5-10km without creating significant errors. Due to this, the best approach was to begin with a multi-region model with global parameters and manually adjust each region, visually inspect the output, and re-adjust the regions until the best fit solution is found. This is a qualitative analysis, but with nine regions and two parameters the search space is too large to search in this study.

Figure 5.39 shows a global Airy model with a t_{avg} of 120km. This was the starting point for the multi-region model. Figure 5.40 shows the result of the manual search for the best fitting multi-region Airy model. This model has an RMS value about 15% lower than the global model. Certain regions have a lower residual signal in this figure, such as Utopia planitia and the Tharsis bulge. Other regions are less affected, such as Hellas basin and Isidis planitia. The values of T_e and t_{avg} used in this figure can be found in Table 5.4. The t_{avg} of most regions has been reduced from the original 120. The RMS value of each region varies significantly, with regions like Hellas basin having an RMS of 75 and regions like Isidis planitia having an RMS of 220.

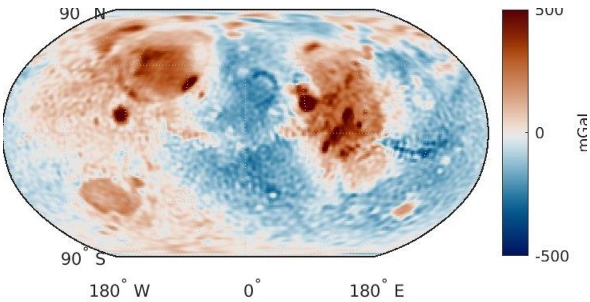

Figure 5.39: The residual map of an Airy model with all regions using an average lithospheric thickness of 120km. RMS = 125.9

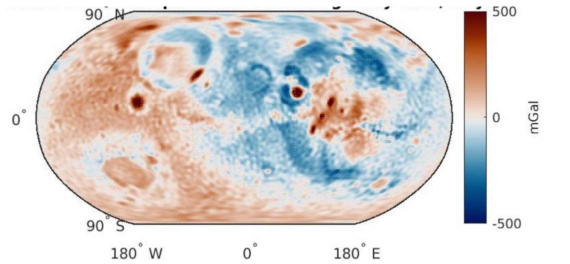

Figure 5.40: The residual map of the best fitting 3d Airy model starting from an average lithospheric thickness of 120km. Values used are in Table 5.4. RMS = 110.0

Region	Average lithospheric thickness [km]	RMS	CP residual [mGal]
Global	-	110.0	-
North	118	93.5	-
South	120	95.5	-
Tharsis	110	172.4	-
Hellas	115	74.8	133.3
Argyre	113	108.1	114.0
Isidis	115	217.7	566.2
Utopia	107	110.1	6.1
Elysium	115	128.3	0
Olympus	100	185.8	1067.4
Alba	103	170.3	-193.0
Valles	120	102.7	-85.0

Table 5.4: Average lithospheric thicknesses used per region for the best fitting Airy model in Figure 5.40. The RMS and central point residual of each region are also given.

The same procedure was carried out for the infinite plate model, except that the T_e was also varied. Figure 5.41 shows the result of the search for the infinite plate model. The RMS value of this model is, at 99.5, noticeably lower than that of the best fitting multi-region Airy model. The Tharsis region has no strong signals in this plot, and Elysium mons is hardly visible. There is a strong signal in a small region where Utopia planitia and Elysium mons overlap, this is one example of the errors that can occur at region boundaries.

Table 5.5 shows the values used in the best fitting multi-region infinite plate model. Most regions favored a T_e of either zero or the maximum (400km), although a few favored a moderately low value. The t_{avg} values are not too different from those used in the Airy model. As this is a flexure model, the RMS and central point residual values of the regions in the model are provided. The central point values for Elysium mons were removed as they varied wildly. Overall, the lower spherical harmonic bounds have a significantly lower RMS value than the full range.

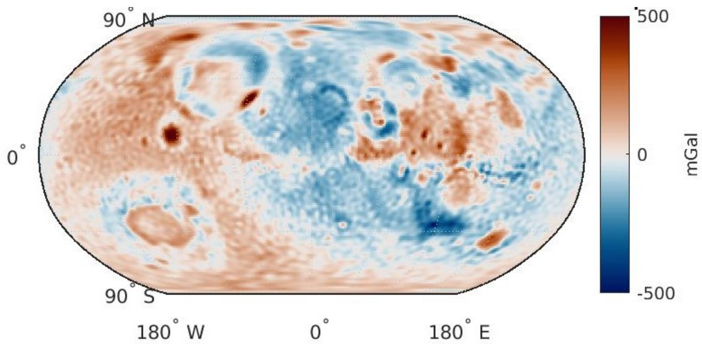

Figure 5.41: The residual map of the best fitting 3d infinite plate model starting from an average lithospheric thickness of 120km. 1:90. Values used are in Table 5.5. RMS = 99.5

Region	Average lithospheric thickness [km]	T_e [km]	1:90	1:20	1:10
Global	-	-	RMS:99.5	RMS:90.7	RMS:86.8
North South	118 120	0 0	RMS:86.4 RMS:89.5	RMS:75.4 RMS:84.9	RMS:76 RMS:83
Tharsis	110	400	RMS:148.9	RMS:139	RMS:127.3
Hellas	115	0	RMS:72.3 CP:102.0	RMS:53.0 CP:122.7	RMS:64.6 CP:177.8
Argyre	113	400	RMS:154.4 CP:308.8	RMS:83.7 CP:177.2	RMS:39.2 CP:-27.6
Isidis	115	400	RMS:214.7 CP:536.7	RMS:194.2 CP:314.3	RMS:209.9 CP:245.1
Utopia	107	40	RMS:111.2 CP:-7.7	RMS:104.3 CP:104.9	RMS:70.6 CP:-59.3
Elysium	115	0	RMS:136.6 CP:0	RMS:127.4 CP:0	RMS:87.7 CP:0
Olympus	100	400	RMS:149.2 CP:317.6	RMS:108.3 CP:-103.1	RMS:67 CP:-64
Alba	103	40	RMS:81.6 CP:-121.0	RMS:70.7 CP:-120.2	RMS:67.8 CP:-89.6
Valles	120	40	RMS:107.5 CP:-116.5	RMS:120.3 CP:-94.4	RMS:94.9 CP:-87.8

Table 5.5: Average lithospheric thicknesses used per region for the best fitting infinite plate model in Figure 5.41 for all spherical harmonic bounds. The RMS and central point residual of each region is provided.

The same process done for the thin shell model lead to Figure 5.42. This plot has a higher RMS value than the infinite plate model best fit. Overall, some regions stand out more in this figure, such as Alba and Olympus mons. On the other hand, Elysium mons and Utopia planitia do not have a distinct signal that stands out from the background.

Table 5.6 shows the values used for each region in this best fitting thin shell multi region model. Some changes are clear, like the reduction in T_e at the Tharsis bulge. This is unexpected, but a high T_e in Tharsis was worsening the fit of many features inside of Tharsis. The lower spherical harmonic bands show a significantly lower RMS in many regions than the full spectrum. This is not true for all regions: Isidis planitia has a higher RMS for the 1:20 signal than for the 1:10 signal. Some features benefit significantly from a reduces spherical harmonic band: the RMS of Olympus mons is 185 at 1:90, but only 108 at 1:10. The same trend is visible in Alba mons and Argyre basin. Some regions are relatively unaffected by the spherical harmonic band, such as Isidis planitia.

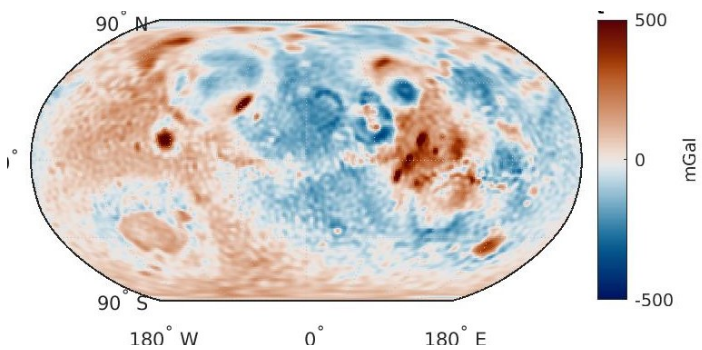

Figure 5.42: The residual map of the best fitting 3d thin shell model starting from an average lithospheric thickness of 120km. 1:90. Values used are in Table 5.6. RMS = 104.3

Region	Average lithospheric thickness [km]	T_e [km]	1:90	1:20	1:10
Global	-	-	RMS:104.3	RMS:95.9	RMS:89.6
North South	118 120	0 0	RMS:87.3 RMS:91.4	RMS:74.9 RMS:86.7	RMS:74.6 RMS:83.3
Tharsis	115	0	RMS:159.9	RMS:150.0	RMS:142.8
Hellas	115	0	RMS:63.7 CP:108.2	RMS:52.1 CP:109.8	RMS:66.1 CP:171.5
Argyre	113	400	RMS:166.2 CP:345.4	RMS:105.0 CP:214.0	RMS:26.3 CP:-12.8
Isidis	115	0	RMS:201.5 CP:539.9	RMS:177.9 CP:293.3	RMS:189.6 CP:223.2
Utopia	107	40	RMS:108.6 CP:-174.9	RMS:111.1 CP:-77.3	RMS:70.2 CP:-126.6
Elysium	115	0	RMS:143.1 CP:0	RMS:134.5 CP:0	RMS:95.3 CP:0
Olympus	100	400	RMS:184.9 CP:259.7	RMS:166.0 CP:-138.4	RMS:107.9 CP:-138.0
Alba	115	40	RMS:150.6 CP:-321.3	RMS:155.5 CP:-199.7	RMS:75.8 CP:32.6
Valles	120	40	RMS:127.0 CP:-120.8	RMS:115.2 CP:-87.4	RMS:107.8 CP:-58.2

Table 5.6: Average lithospheric thicknesses used per region for the best fitting thin shell model in Figure 5.42

6
Discussions

General remarks

There are several noteworthy elements of the results of the global models that require more interpretation. An Airy model is based entirely on topography, as seen in Equation 3.2. For this reason, the lithosphere thickness profile they generate looks almost exactly like the input topography, except it is inverted. This is translated into the gravity signal of the Airy models: for low t_{avg} models the gravity signal looks very much like a lower resolution topography signal. This is visible in Figures 5.8 and 5.11. The residuals of the Airy end members show this particularly well: Figure 5.16 looks nearly identical to the topography signal of Mars. As the flexure models are modifications of the Airy model, this trait is also passed to them. A very stiff lithosphere mitigates this effect by lessening the compensation in the subsurface. How well a region is fit by the Airy model or a high T_e flexure model can thus be a good source of information about the subsurface.

A region that does not appear in the residual of an Airy model can be said to be fully isostatically compensated. All of the topography is being compensated by the subsurface, meaning that the lithosphere is weak. A region that does not appear in a very high T_e flexure model is fully supported by the lithosphere, causing no compensation. This indicates that the lithosphere is very strong under the region. The history behind why the Martian lithosphere may be regionally strong or weak is not fully understood (Wieczorek (2015), Neumann et al. (2004)) and is not the focus of this study.

The best fit values for the global models vary but are generally found for a t_{avg} of around 200km and a very low T_e. This is supported by the Airy, infinite plate, and thin shell models. However, the lithospheric thickness value is significantly higher than those found in literature. Neumann et al. (2004) finds a global average lithospheric thickness above 45 km, with the southern hemisphere having average of 32 km and the northern hemisphere having an average of 58 km. Ding et al. (2019) used a value of 50 km, Thor (2016) calculated global thicknesses of under 100 km, Neumann et al. (2004) found no value higher than 125 km, and Veldhuizen (2019) calculated an average global thickness of 55 km. Some of the difference between the literature values and the value of this study can be explained due to the differing methods, spherical harmonic bounds, and datasets used by different studies, however, it is clear that this flexural isostasy method yields higher average lithospheric thickness values than the bulk of the literature would suggest.

Tying to the differences between this study and literature, in this study finding a global best fit is made complicated by the fact that many models, both global and regional, find a manifold of solutions which are very similar in terms of RMS. This can be seen in Airy and flexure models in this study, and is particularly strong in the regional analyses. Taking Figure 5.17 as an example, there are many combinations of T_e and t_{avg} that yield a global RMS value within 10% of the best fitting value. This makes it difficult to say that the model really finds a best fit, it is more accurate to say that the model suggests a range of T_e and t_{avg} as feasible.

One cause of this problem is that increasing the T_e and increasing the t_{avg} have a similar effect on the results of some models. This is seen in the end members of Chapter 5. An increase in the T_e reduces the amount of compensation in the subsurface, weakening the compensating gravity signal. An increase in t_{avg}

pushes the compensating gravity signal source farther away from the topography, effectively weakening the compensating gravity signal. The effects are not identical, but are similar enough that they contribute to the manifold of solutions found in this report. An extreme example of this is found in the end member residuals of the global thin shell model, where varying the t_{avg} has virtually no effect on the results once the T_e is high enough. The lithosphere has become so strong that there is essentially no compensation anymore. Thus, almost all values of t_{avg} are part of the manifold of solutions for that model.

Compounding this problem is that visual inspection of the best fitting model often raises questions about the quality of the fit. The global models all show a parabolic relationship between the T_e and t_{avg}, which is useful for finding a best fitting value. However, visual inspection of the end members reveals that the reason there is a parabolic fit is that at low values some regions show a high positive residual and some show a low negative residual, while at high values the same regions show the opposite residual. At moderate values all regions are fit equally well (or equally badly), leading to a best fitting model. The best fitting model is thus a compromise between modelling the various features of the Martian surface, and the best fitting values of T_e and t_{avg} do not necessarily say anything about the subsurface of the planet.

This issue also calls the usefulness of the global RMS into question. The global RMS value is used as an indicator of the quality of a model as the amount of models generated in this study is too high for a visual inspection of them all. Without any visual inspection however, the global RMS value would lead the reader to a best fitting value that is not very meaningful. This problem is smaller in the regional analyses as these often focus on a single feature, but even then there are still issues. The best fitting models of Hellas basin, for example, do not perfectly model the center of the basin because that would result in a very bad fit of the edges, crater walls, and the surrounding plateaus. The regions can always be made smaller, but this issue will always exist: are you modelling the top of Olympus mons, the slopes, or its foothills? Each area will have a different best fit, and the global RMS value will lead to a best fit that does not fit any of these areas best.

The central point residual value is a step forward, but is also not a solution to these problems. Firstly, the center of a region is not always the point of interest of the region being studied. Secondly, the relatively high resolution of the models used in this study sometimes cause the central pixel in the region to vary wildly in magnitude and sign, as seen in the regional analyses results of Chapter 5. Thirdly, the central point residual effectively picks one pixel that the model should fit. This is perhaps a more specific measurement than the central point RMS, but it still leads to the fitting of one part of the region while the model ignores the rest of it. This is why even with an RMS and central point residual value, visual inspection is necessary before any conclusions can be drawn from the results.

With this in mind, the fact that the thin shell model consistently has a higher RMS than the infinite plate model is not as conclusive as it previously seemed. Visual inspection of the residual plots in Chapter 5 shows that some regions are well-modelled by the thin shell model as well as the infinite plate model. In the multi-region studies it was also clear that some regions had a lower RMS in the thin shell model than in the infinite plate model. The best way to judge this would be to place the results of each region, from all models, side by side and compare them visually. This was not possible in this study due to time constraints, and it is doubtful that any future study will have the time to do this either.

Other differences between the infinite plate and thin shell models need discussing. The flexural response function of the thin shell model was seen to act more as a binary filter than an attenuation function as compared to the infinite plate model. This was shown in Figure 3.12. This can be explained physically by the fact that, compared to the infinite plate model, the thin shell model allows for a region to be supported by the curved shell around it. A curved shell provides more structural support than a flat plate, as can be seen in bridge design. A thin shell lithosphere is thus stronger and deflects less in response to loads than an infinite plate lithosphere. This supports the fact that the thin shell model favors lower T_e values than the infinite plate model for almost all regions, as a smaller thin shell model T_e has a similar effect as a larger infinite plate model T_e. This is also what lead to the end member residuals of the global thin shell model being virtually insensitive to changes in t_{avg}: all degrees higher than 10 were being completely blocked by the thin shell flexural response function. Previous studies of the infinite plate model focused on medium spherical harmonic degrees (Veldhuizen (2019)), this will only be possible with the thin shell model for very low values of T_e, regardless of the lithospheric thickness.

Both flexure models were found to be impacted much more strongly by variations in T_e than variations in t_{avg}. This is an encouraging sign for the use of flexure models and indicates that the strength of the lithosphere is much more important than its thickness when analyzing a region. A model that does not allow for variations in the flexural rigidity of the lithosphere would therefore miss a significant contributor to the subsurface structure.

Having said this, the global RMS values across all models show that spherical harmonic degrees 1:10 capture about 80% of the total RMS value of a model. This indicates that a major source of error for the models is the low degrees. However, these are the degrees who's signal is normally not attributed to flexure (Beuthe (2008)). This means that the main source of error in the flexural isostatic models in this study is actually not coming from a source related to flexural isostasy, and is an example of applying the wrong tool to a problem. Some authors attempt to mitigate this by including bottom loading in their studies, with successful results for some regions (Broquet and Wieczorek (2019)).

Regional discussions

The martian dichotomy is well modelled by this study. The dichotomy seems to be in isostatic equilibrium, as seen by the fact that its signal is visible in the topography signal but not in gravity signal. The Airy model used in this study can quite effectively remove its signal without any flexure models needing to be used. This also means that using window functions to isolate and model the dichotomy halves separately is not necessary. Judging by global RMS there is no clear best fit resulting from the dichotomy analysis, but this ties in to the previously discussed issues with the global RMS being used as a judge of quality. It is clear however that the dichotomy is best modelled by an Airy type model with no flexure.

In the regional studies, a large amount of models are required to explore the variable space of all the regions, making this the topic that most needs a reliable way of judging the quality of models without human visual inspection. Despite this, some conclusions can still be drawn from the regional results in this study. As discussed earlier, the thin shell model favors lower T_e values than the infinite plate model, and this was generally also true in the regional analyses. However, two notable exceptions to this are Argyre Basin and Olympus Mons, where the opposite is true. For those two regions the infinite plate and thin shell model both favored the maximum values of T_e and t_{avg}, which as discussed have similar effects on the model results. This indicates that these two regions have either extremely strong or extremely thick lithospheres (or both). The best fits of Argyre Basin and Olympus Mons are also generally the opposite of the best fits of other regions, which mostly prefer low or moderate values of T_e and t_{avg}. This is another sign that these two areas have different subsurface properties than the rest of the planet. For Olympus mons, the largest mountain in the solar system on one of the largest topographical features in the solar system, it is very believable that the lithosphere is thick and strong underneath it. For Argyre basin this is not the case, however, although what is causing this is not answerable by this study.

A relatively strong lithosphere under Olympus mons agrees with the results found in literature, for example in the admittance model of McGovern et al. (2004). Beuthe et al. (2012) reports a lower bound for the T_e of Olympus mons of 80 km, which is in line with what was found in this study. Belleguic et al. (2005) finds a value of $T_e = 90 \pm 40$ km. These values are a good bit lower than the 400 km found in this study. All three sources mentioned in this paragraph note that the crustal thickness of Olympus Mons is poorly constrained by admittance modelling. The same result was found in the thin shell model results of this study, where once T_e becomes high enough large changes in t_{avg} hardly affect the results. Similarly, Musiol et al. (2016) performs a flexural study of Olympus mons and concludes that the flexure has an overriding influence on the results, significantly larger than the other variables in the model.

The lithospheric elastic thickness found for Arygre basin by Ding et al. (2019) is 50 - 130 km, with a best fit of 90 km. This is half to a quarter of the value found by the Airy and infinite plate models and is most closely approximated by the thin shell model. It is notable that Argyre basin and Olympus mons are both best fit by the same parameters, as they are very different topographical features. This implies that the subsurface of Argyre basin is similar to that of Olympus mons, something which cannot be explained by isostasy or flexure alone.

Contrary to Olympus mons, Alba mons is very well modelled by this study. Its signal is not visible in many residual plots, including those of the multi-region models. It favors a low T_e and lithospheric thickness, although it is still relatively thick due to its position so close to the Tharsis bulge. This is supported by Heller and Janle (1999), where a non-flexure study concludes that the lithosphere under Alba mons is in the 150 - 200 km range. An estimate for the T_e of Alba mons is provided by Ding et al. (2019) as a range of 60 - 210 km with 75 km being the best fit. Once again, the thin shell model in this study produces the best fitting results at these literature values. Alba mons appears to be relatively isostatically compensated compared to the rest of the Tharsis mountains. An explanation for this could lie in its greater distance from Tharsis than the rest of the mountains.

Elysium mons is also very well in this study. This is particularly notable in the multi-region thin shell model, where there is almost no gravity signal around the volcano. All models show this sort of behaviour for Elysium mons, and are able to remove its signal with a T_e value of zero. This indicates that flexure is not needed to model this area, and that the volcano is likely isostatically compensated in an Airy like way. In literature, Neumann et al. (2004) agrees that Elysium is likely fully isostatically compensated and shows no signs of flexure. Ding et al. (2019) finds a small T_e value of 15 km for Elysium, but notes that the T_e value is highly dependent on the chosen loading type.

Also present on the Tharsis bulge, Valles marineris is unfortunately not well modelled: it's signal is visible in results from all models. This is is partially due to its shape not working well with the spherical caps in the pyshtools software, as any localization window will include large areas of the surrounding Tharsis region. However, this is likely also due to the effect of the relatively thin and long shape of the valley. Unlike for example Hellas basin, there is no large central depression in Valles marineris. This makes it much easier for the lithosphere to support its load even at very low T_e values, meaning that the valley would show a low T_e and a low amount of Moho deflection.

Hellas basin, contrary to Valles marineris, is relatively well modelled by a regular Airy model with a very low t_{avg}. The lithospheric thickness at Hellas basin seems to be only a few kilometers thick according to the results of this study. This indicates a very high level of isostatic compensation. Similar results are found by Neumann et al. (2004) and Wieczorek and Zuber (2004), validating the results of this study.

The same cannot be said of the nearby Isidis and Utopia planitias. These two features are similar in that they both lack a topography signal but posses a gravity signal. The two regions differ significantly in their results, however. Utopia planitia is not well modelled by the Airy or inifinite plate model as seen in the multi-region analyses. There is no combination of T_e and t_{avg} that makes its signal disappear. The thin shell multi region model however does a good job of modelling the region with the same input parameters as the infinite plate model. On the other hand, Isidis planitia has not been well modelled by a single model in this study, regardless of what parameters or spherical harmonic bounds are used. There is always a large residual at Isidis. This is certainly an indication of a mass anomaly, bottom loading, or some other anomaly in the subsurface, although details about this anomaly cannot be determined with the methods in this report. It is also unusual that the thin shell model better addresses Utopia planitia but not Isidis planitia, hinting that despite their superficial similarity the subsurface under the two plains may be quite different. Ding et al. (2019) finds a best fitting T_e value of 300 km for isidis planitia, but a value of 30 km for utopia planitia. This confirms the differences found in this study.

7 Conclusions

There are several conclusions that can be drawn from this study. The first is that better methods of judging the performance of models without human visual inspection of their results is necessary in order to realize the full potential of the flexural isostasy models presented in this study. The lack of suitable methods leads to a manifold of best fitting solutions for many of the problems modelled in this study, hindering firm conclusions about the subsurface of Mars.

Secondly, a global density of 2900 kg/m^3 and global average lithospheric values of 200 (Airy, infinite plate) to 240 km (thin shell) combined with very low effective lithospheric elastic thickness values of 0 to 40km are the best fit values found in this study. Regionally there are large variations, with some features being fully isostatically compensated, others being supported by locally strong lithospheres, and others resting on buried mass anomalies that cannot be explained with the models in this report. Globally the models in this study calculate a higher average lithospheric thickness than the majority of literature values, however, the multi-region analysis results in regional results which generally agree with literature.

In a dichotomy study, the best fitting values were found for a northern lithosphere zero to ten kilometers thinner than the southern lithosphere and a T_e of zero. Flexural isostasy methods are not needed to model the dichotomy, as pure isostasy fits the observations.

The thin shell model is much more sensitive to nonzero lithospheric elastic thickness values than the infinite plate model, providing very strong lithospheres at low elastic thicknesses. This is due to its aggressive flexural response function's filtering of higher spherical harmonic degree signals. Both flexural isostasy models are significantly more sensitive to variations in T_e than in t_{avg}, meaning that studies that do not include flexure could be missing an important piece of information.

Regionally, the thin shell model never performs worse than the infinite plate model while outperforming it in certain regions. Utopia planitia, Elysium, and many features in the Tharsis bulge are better modelled by the thin shell model. The topography of these regions is not similar, and so the fact that the thin shell model fits these areas better is a suggestion that similar processes are at work in the subsurface of these areas. Isidis planitia and Argyre basin are not fit well by any model, while Hellas basin and Alba mons are fit well by an Airy type model with no flexure. Several features in the Tharsis region, such as Olympus mons, require flexural isostasy models to be well fit. This suggests that the Tharsis region's subsurface may fit the thin shell model assumptions better than other regions on the planet.

Inspecting the spherical harmonic bands, 80% of the residuals in all models can be attributed to spherical harmonic degrees 1 to 10. These signals are likely not caused by flexural isostasy, and require the inclusion of other phenomena (for example bottom loading, mass anomalies, mantle plumes, etc) to fit the observations.

The research question of this study was stated in Chapter 1 as:

- *What is the impact of allowing for an anisotropic thin-shell, compared to a simpler infinite plate, in a topography loaded flexural isostatic model of Mars?*

The impact of using the thin shell instead of the infinite plate model can be summarized in three points:

- An increased sensitivity to variations in T_e, resulting in overall lower best fitting T_e values.
- Higher RMS value of model residuals in global analyses
- Results more closely matching the observations and literature in the Tharsis region and at Utopia planitia.

Notable is that, in the regional analyses, no region was worse modelled with the thin shell model than with the infinite plate model. This is largely due to the fact that outside of certain regions, the thin shell model results do not differ significantly from those of the infinite plate. This is a clear argument in favor of using the thin shell model. Care must be taken, however, in applying the thin shell model globally as the results are not necessarily more useful than those of the infinite plate model. The infinite plate model is best applied regionally, specifically to regions suspected to have a very thick or strong lithosphere as well as regions that the infinite plate model fails to explain.

A caveat to this conclusion is that several issues identified with the RMS and central point residual as a means of judging model performance. Globally, the infinite plate model outperformed the thin shell, but an thin shell anisotropic global model lead to a model with 15% lower residuals than an anisotropic global infinite plate model. Additionally, many regions in the model were visually better fit in the anisotropic model than in the global model.

8 Recommendations

My main recommendation to anyone using the methods in this report in any study is, unsurprisingly, to find a way to accurately judge the performance of models without human intervention. This issue is fundamentally limiting to any studies aiming to use these methods to their full potential. For every tools used to judge models it should be clear what it measures, what kind of model it will select as a best fitting one, and what implications this has for the research it is being applied to.

My second recommendation is to not write the thin shell model off as 'worse' than the infinite plate or Airy model. It is true that on a global scale it generally performs worse than the other models, but its reduction of the residuals of Utopia planitia to zero is a very promising feat. Many studies attribute the gravity signal in that region to a subsurface mass anomaly, but if the thin shell model can offer an alternative explanation then it will be a valuable contribution to the body of knowledge.

If the issue of non-human model judging is solved, I recommend that the future student spends less time making models and more time running them. The models in this study are very modular in their functioning, and it is possible to set up any number of experiments with them. In this study, the limiting factor in the real quality of this research was the time it took to create the code and then interpret the many many models I generated with it. I am certain much more information can be acquired using these models in their current form.

If the goal is to take the models one step further, I recommend investigating bottom loading. This will likely help explain features in the Tharsis area, at Isisids (and maybe Utopia) plantia, and possibly at Argyre basin, and generally add a whole lot of depth and complexity to your results and the possible interpretations of your work.

Bibliography

Belleguic, V., LognonnÃ©, P. and Wieczorek, M. (2005), 'Constraints on the martian lithosphere from gravity and topography data', *Journal of Geophysical Research: Planets* **110**(E11).

Beuthe, M. (2008), 'Thin elastic shells with variable thickness for lithospheric flexure of one-plate planets', *Geophysical Journal International* **172**, 817–841.

Beuthe, M., Le Maistre, S., Rosenblatt, P., Pätzold, M. and Dehant, V. (2012), 'Density and lithospheric thickness of the tharsis province from mex mars and mro gravity data', *Journal of Geophysical Research: Planets* **117**(E4).

Beuthe, M., Rosenblatt, P., Dehant, V., J.-P., B., M., P., B., H., A., K., S., L. M. and T., V. H. (2006), 'Assessment of the martian gravity field at short wavelength with mars express', *Geophysical Research Letters* **33**(3).
URL: *https://agupubs.onlinelibrary.wiley.com/doi/abs/10.1029/2005GL024317*

Breuer, D. and Spohn, T. (2003), 'Early plate tectonics versus single-plate tectonics on mars: Evidence from magnetic field history and crust evolution', *Journal of Geophysical Research: Planets* **108**(E7).
URL: *https://agupubs.onlinelibrary.wiley.com/doi/abs/10.1029/2002JE001999*

Breuer, D. and Spohn, T. (2006), 'Viscosity of the martian mantle and its initial temperature: Constraints from crust formation history and the evolution of the magnetic field', **54**, 153–169.

Broquet, A. and Wieczorek, M. A. (2019), 'The gravitational signature of martian volcanoes', *Journal of Geophysical Research: Planets* **124**(8), 2054–2086.

de Bakker, L. (2016), Seismic analysis of mars using gravitationa potential stresses - insight, Msc. thesis, Technical University Delft.

Ding, M., Lin, J., Gu, C., Huang, Q. and Zuber, M. (2019), 'Variations in martian lithospheric strength based on gravity/topography analysis', *Journal of Geophysical Research: Planets* **124**.

DiVenere, V. (2017), 'Evidence for internal earth structure and composition'. `http://www.columbia.edu/~vjd1/earth_int.htm`.

Fowler, C. M. (1993), 'The solid earth : an introduction to global geophysics / c. m. r. fowler', **10**.

Genova, A., Goossens, S., Lemoine, F. G., Mazarico, E., Neumann, G. A., Smith, D. E. and Zuber, M. T. (2016), 'Seasonal and static gravity field of mars from mgs, mars odyssey and mro radio science', *Icarus* **272**, 228 – 245.
URL: *http://www.sciencedirect.com/science/article/pii/S0019103516001287*

Grott, M. and Wieczorek, M. (2012), 'Density and lithospheric structure at tyrrhena patera, mars, from gravity and topography data', *Icarus* **221**(1), 43 – 52.
URL: *http://www.sciencedirect.com/science/article/pii/S0019103512002825*

Heller, D. and Janle, P. (1999), 'Lineament analysis and geophysical modelling of the alba patera region on mars', *Earth, Moon, and Planets* .

Kaban, M. K., Stolk, W., Tesauro, M., El Khrepy, S., Al-Arifi, N., Beekman, F. and Cloetingh, S. A. P. L. (2016), '3d density model of the upper mantle of asia based on inversion of gravity and seismic tomography data', *Geochemistry, Geophysics, Geosystems* **17**(11), 4457–4477.
URL: *https://agupubs.onlinelibrary.wiley.com/doi/abs/10.1002/2016GC006458*

Kieffer, H. and Zent, A. (1992), *Quasi-periodic climate change on Mars*, pp. 1180–1218.

Mangold, N., Allemand, P., Thomas, P. and Vidal, G. (2000), 'Chronology of compressional deformation on mars: evidence for a single and global origin', *Planetary and Space Science* **48**(12), 1201 – 1211. Mars Exploration Program.
URL: *http://www.sciencedirect.com/science/article/pii/S0032063300001045*

Mars high resolution gravity fields from MRO, Mars seasonal gravity, and other dynamical parameters (2011), *Icarus* **211**(1), 401 – 428.

McCollom, T. M. (2006), *The Habitability of Mars: Past and Present.*

McGovern, P. J., Solomon, S. C., Smith, D. E., Zuber, M. T., Simons, M., Wieczorek, M. A., Phillips, R. J., Neumann, G. A., Aharonson, O. and Head, J. W. (2004), 'Correction to "localized gravity/topography admittance and correlation spectra on mars: Implications for regional and global evolution"', *Journal of Geophysical Research: Planets* **109**.

Musiol, S., Holohan, E. P., Cailleau, B., Platz, T., Dumke, A., Walter, T. R., Williams, D. A. and Gasselt, S. (2016), 'Lithospheric flexure and gravity spreading of olympus mons volcano, mars', *Journal of Geophysical Research: Planets* **121**(3), 255–272.

NASA/JPL/USGS (2000), 'Mars orbiter laser altimiter (mola) globe'. `https://photojournal.jpl.nasa.gov/catalog/PIA02993`.

NASA/JPL/USGS (2019), 'Pds geosciences node data and services: Mgs mola'. `https://pds-geosciences.wustl.edu/missions/mgs/mola.html`.

NASA/JPL/USGS (2020), 'Planetary laser altimeter'. `https://tharsis.gsfc.nasa.gov/MOLA/index.php`.

Neumann, A. G., T., Z. M., A., W. M., J., M. P., G., L. F. and E., S. D. (2004), 'Crustal structure of mars from gravity and topography', *Journal of Geophysical Research: Planets* **109**(E8).
URL: *https://agupubs.onlinelibrary.wiley.com/doi/abs/10.1029/2004JE002262*

O'Neill, C., Jellinek, A. and Lenardic, A. (2007), 'Conditions for the onset of plate tectonics on terrestrial planets and moons', *Earth and Planetary Science Letters* **261**(1), 20 – 32.
URL: *http://www.sciencedirect.com/science/article/pii/S0012821X07003457*

Root, B., Novák, P., Dirkx, D., Kaban, M., van der Wal, W. and Vermeersen, L. (2016), 'On a spectral method for forward gravity field modelling', *Journal of Geodynamics* **97**, 22 – 30.

Thor, R. (2016), Mapping the thickness of the martian elastic lithosphere using maximum likelihood estimation, Msc. thesis, Technical University Delft.

Turcotte, D. L., Willemann, R. J., Haxby, W. F. and Norberry, J. (n.d.), 'Role of membrane stresses in the support of planetary topography', *Journal of Geophysical Research: Solid Earth* **86**(B5), 3951–3959.
URL: *https://agupubs.onlinelibrary.wiley.com/doi/abs/10.1029/JB086iB05p03951*

Veldhuizen, R. (2019), Regional isostasy model for the crust of mars, Bsc. thesis, Technical University Delft.

Watts, A. (2001), *Isostasy and Flexure of the Lithosphere*, Vol. 458.

Watts, A. B. and Moore, J. D. P. (n.d.), 'Flexural isostasy: Constraints from gravity and topography power spectra', *Journal of Geophysical Research: Solid Earth* **122**(10), 8417–8430.

Wieczorek, M. (2015), *Gravity and Topography of the Terrestrial Planets*, pp. 153–193.

Wieczorek, M. A. and Meschede, M. (2018), 'Shtools: Tools for working with spherical harmonics', *Geochemistry, Geophysics, Geosystems* **19**(8), 2574–2592.

Wieczorek, M. A. and Simons, F. J. (2005), 'Localized spectral analysis on the sphere', *Geophysical Journal International* **162**(3), 655–675.

Wieczorek, M. A. and Simons, F. J. (2007), 'Minimum-variance multitaper spectral estimation on the sphere', *Journal of Fourier Analysis and Applications* **13**, 665–692.

Wieczorek, M. and Zuber, M. (2004), 'Thickness of the martian crust: Improved constraints from geoid-to-topography ratios', **5714**.

Wild, F. and Heck, B. (2005), A comparison of different isostatic models applied to satellite gravity gradiometry, *in* C. Jekeli, L. Bastos and J. Fernandes, eds, 'Gravity, Geoid and Space Missions', Springer Berlin Heidelberg, Berlin, Heidelberg, pp. 230–235.

A

Regions

The list of regions and the map of the regions are repeated here for easy reference. Figure A.1 shows the locations of the regions, while the regions themselves are:

- **The dichotomy halves** are the largest feature of Mars. Both halves have their own clear gravity anomalies, pointing towards two different global subsurface structures or mass distributions.
- **A: Hellas Basin** is an extremely large positive anomaly. There is far more gravity here than topography can account for, giving evidence for a positive subsurface mass anomaly.
- **B: Argyre Basin**, for the same reason as Hellas Basin.
- **C: Isidis Planitia** also shows a large positive mass anomaly, but unlike the large basins has no corresponding topography, meaning that the mass anomaly is fully underground.
- **D: Utopia Planitia**, for the same reason as Isidis Planitia.
- **E: Elysium Mons** has a negative gravity anomaly but a positive topography, meaning there is less gravity than the volcano can account for.
- **F: Olympus Mons** is an extremely large volcano with a significant positive gravity anomaly. Due to its size it will be included as an area of interest.
- **G: Alba Mons** is a strong negative signal in the Bouguer anomaly, despite being a large volcano.
- **H: The Tharsis bulge** as a whole does not have a clear signal, but due to its size and many large features will be included as an area of interest.
- **I: Valles Marineris** is a very long but relatively narrow feature, which is strongly visible in the Bouguer anomaly.

Table A.1 shows the (lat,lon) position and radius of the $pyshtools.SHGrid.from_cap(radius, lat, lon, lmax)$ command used to create the region (Wieczorek and Simons (2007)). The $lmax$ parameter is the maximum spherical harmonic degree used in the creation of the cap and was set to 89 for all regions, as this yields a spatial domain resolution of 180x360. The (lat,lon) coordinates are given as shown in Figure A.1: the center of the plot is zero, 180W is -180, and 180E is 180 degrees of longitude. 90N is 90, the center is zero, and 90S is -90 degrees. Meanwhile, Figures A.2 to A.10 show plots of the mask of each region multiplied by the topography. All plots are in kilometers. The windows are all circles, although they appear distorted due the fact that a spherical planet's surface is being plotted as a rectangle.

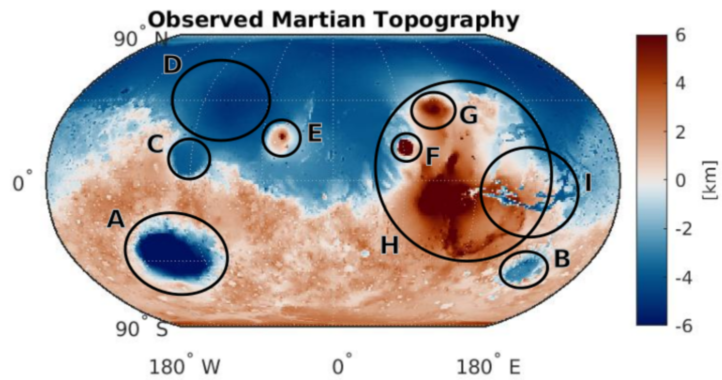

Figure A.1: Locations of the selected areas of interest on Mars. Each area will get a window function that isolates it for regional analysis.

Region	Radius (deg)	(lat, lon) (deg)
Hellas basin	30	(-40,-110)
Argyre basin	10	(-50,138)
Isidis planitia	12	(14,-93)
Utopia planitia	25	(45,-70)
Elysium mons	15	(23,-33)
Olympus mons	12	(19,46)
Alba mons	15	(44,70)
Tharsis	55	(5,85)
Valles marineris	33	(-10,120)

Table A.1: The (lat,lon) position and radius of the $pyshtools.SHGrid.from_cap(radius, lat, lon, lmax)$ command used to create the region (Wieczorek and Simons (2007)). The $lmax$ parameter is the maximum spherical harmonic degree used in the creation of the cap and was set to 89 for all regions, as this yields a spatial domain resolution of 180x360. The (lat,lon) coordinates are given as shown in Figure A.1: the center of the plot is zero, 180W is -180, and 180E is 180 degrees of longitude. 90N is 90, the center is zero, and 90S is -90 degrees.

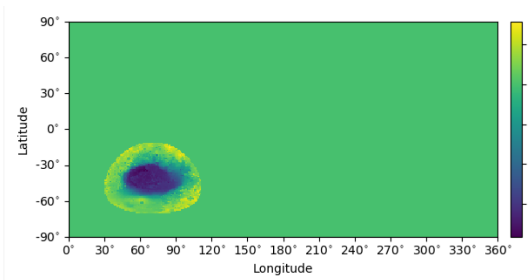

Figure A.2: A plot of the Hellas basin mask multiplied with the topography signal of Mars.

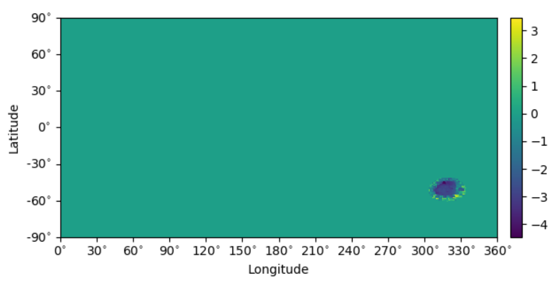

Figure A.3: A plot of the Argyre basin mask multiplied with the topography signal of Mars.

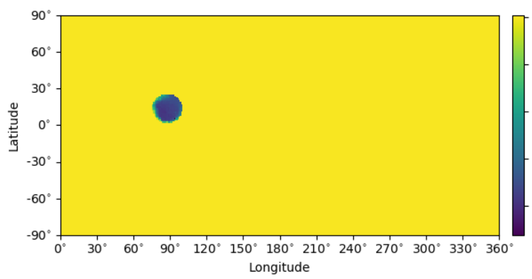

Figure A.4: A plot of the Isidis planitia mask multiplied with the topography signal of Mars.

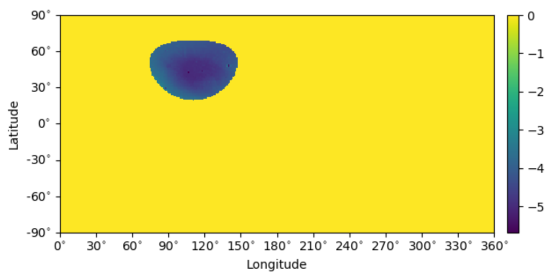

Figure A.5: A plot of the Utopia planitia mask multiplied with the topography signal of Mars.

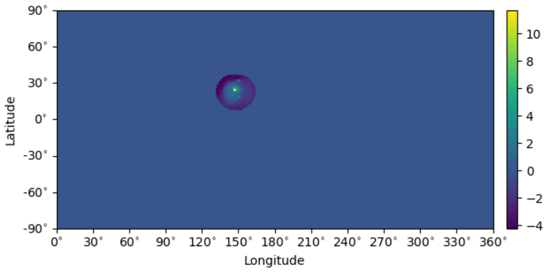

Figure A.6: A plot of the Elysium mons mask multiplied with the topography signal of Mars.

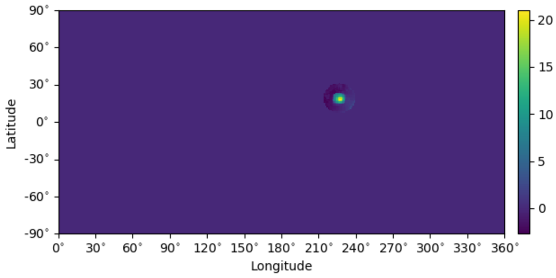

Figure A.7: A plot of the Olympus mons mask multiplied with the topography signal of Mars.

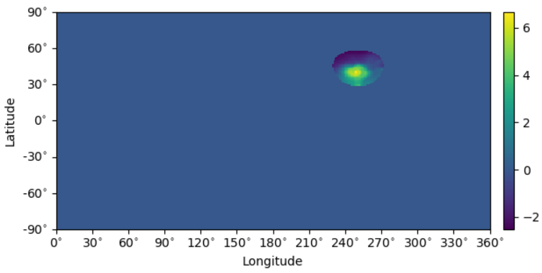

Figure A.8: A plot of the Alba mons mask multiplied with the topography signal of Mars.

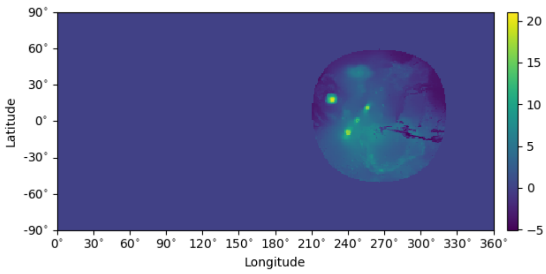

Figure A.9: A plot of the Tharsis mask multiplied with the topography signal of Mars.

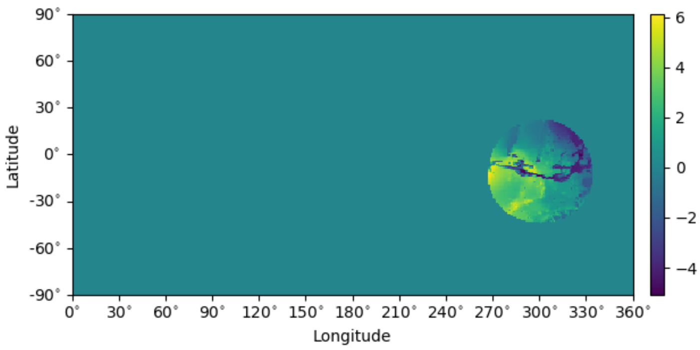

Figure A.10: A plot of the Valles Marineris mask multiplied with the topography signal of Mars.

The dichotomy masks are more elaborate to create. Many caps are created and added together to achieve the desired shape. The first step in the creation of the mask is to select all points on the topography map which are greater than zero. This creates a mask, but it is not a very good dichotomy representation. Table A.2 shows a list of the windows created and added to the initial mask. All of these windows are inverted before they are added to the mask. The lat,lon convention is the same as on the previous page. Figures A.11 and A.12 show the final windows.

Radius (deg)	(lat, lon) (deg)
30	(-40,-105)
20	(-40,10)
25	(-50,138)
45	(5, 90)
25	(-20,140)
35	(5,70)
15	(15,-125)
15	(-2,-154)
15	(-15,-160)
25	(-17,-70)
25	(22,0)
15	(25,-35)
15	(45,-120)
5	(0,20)

Table A.2: A list of the windows created and added to the initial mask. The initial mask is all the areas in which the topography signal is greater than zero. All of these windows are inverted before they are added to the mask. $lmax = 89$ for all windows as this yields a resolution of 180x360 in the spatial domain.

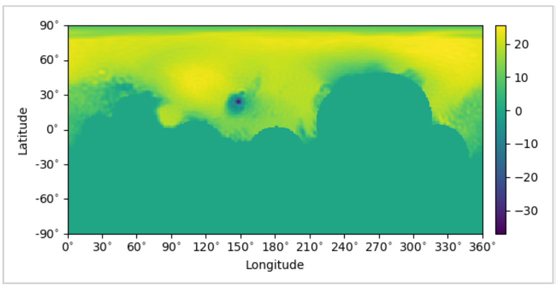

Figure A.11: The northern dichotomy mask applied to an arbitrary Airy lithospheric thickness profile. The signal is untouched in the northern half of the dichotomy, while the southern half is zero.

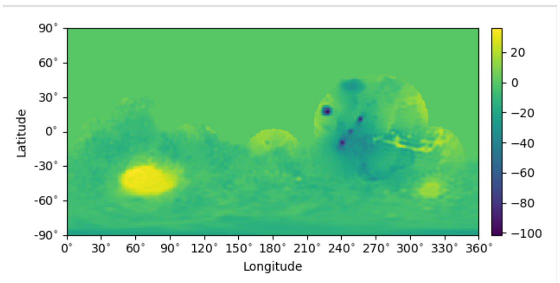

Figure A.12: The southern dichotomy mask applied to an arbitrary Airy lithospheric thickness profile. The signal is untouched in the southern half of the dichotomy, while the northern half is zero.

B
Extended model results

Model & Variable	$d_{avg} = 200[km]$ $T_e = 0$	Residual w.r.t. Bouguer	Endmember low	Endmember high
Infinite plate 2:90 T_e	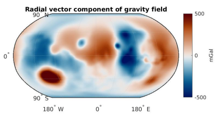	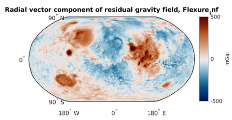	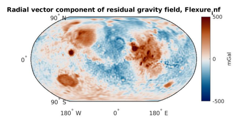	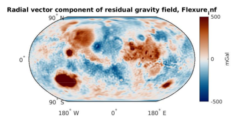
Infinite plate 2:10 T_e	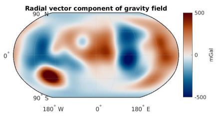	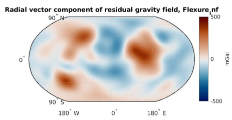	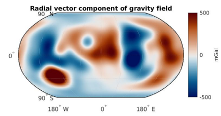	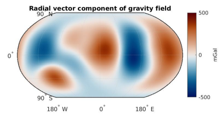
Infinite plate 2:20 T_e	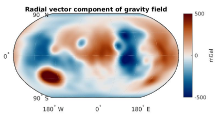	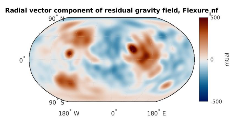	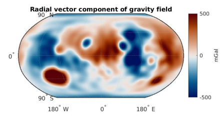	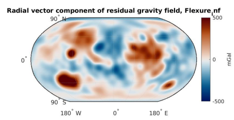
Infinite plate 2:90 t_{avg}	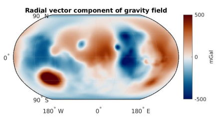	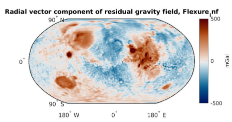	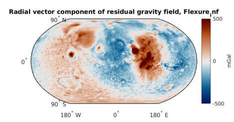	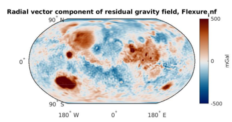
Infinite plate 2:10 T_{avg}	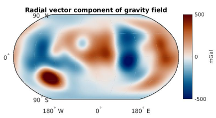	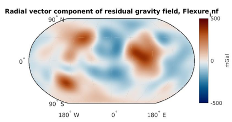	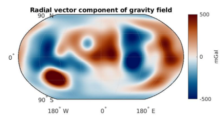	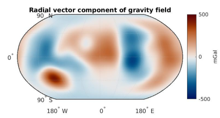
Infinite plate 2:20 t_{avg}	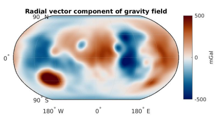	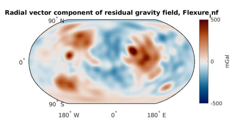	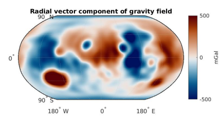	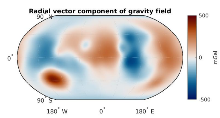

Figure B.1: Plots of the end members for all spherical harmonic bands, using both t_{avg} and T_e. The figure shows six groups of infinite plate models, each on their own row. The first column indicates the type of model, the spherical harmonic bounds of the model, and whether the t_{avg} or the T_e is being investigated. The second column shows the calculated gravity signal of the model with a d_{avg} of 200km and a T_e of zero. The third column shows the residual of the second column with respect to the corresponding Bouguer anomaly. The fourth column shows a residual plot of the low end member. The parameter lowered in the end member is the one in the first column, while the other parameter is kept constant. The last column shows the corresponding high end member.

Model & Variable	$d_{avg} = 200[km]$ $T_e = 0$	Residual w.r.t. Bouguer	Endmember low	Endmember high
Thin shell 2:90 T_e	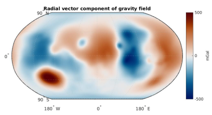	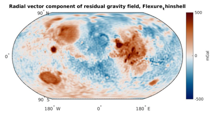	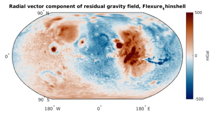	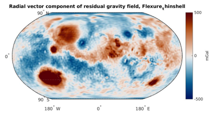
Thin shell 2:10 T_e	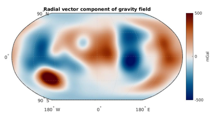	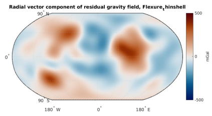	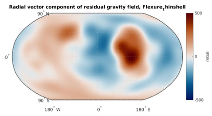	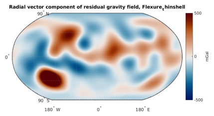
Thin shell 2:20 T_e	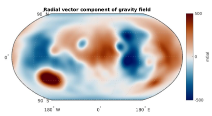	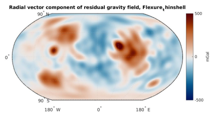	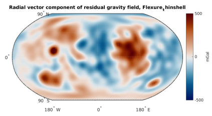	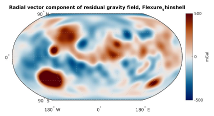
Thin shell 2:90 t_{avg}	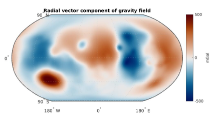	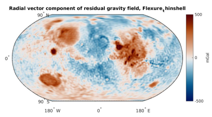	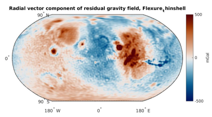	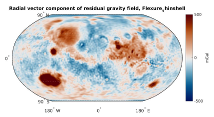
Thin shell 2:10 T_{avg}	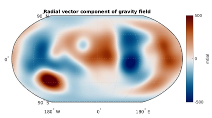	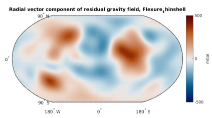	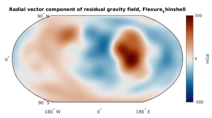	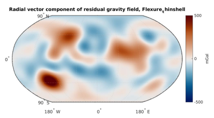
Thin shell 2:20 t_{avg}	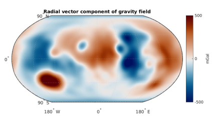	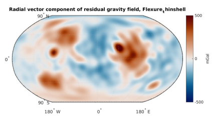	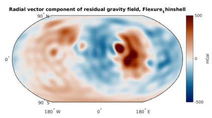	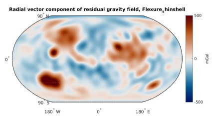

Figure B.2: Plots of the end members for all spherical harmonic bands, using both t_{avg} and T_e. The figure shows six groups of thin shell models, each on their own row. The first column indicates the type of model, the spherical harmonic bounds of the model, and whether the t_{avg} or the T_e is being investigated. The second column shows the calculated gravity signal of the model with a d_{avg} of 200km and a T_e of zero. The third column shows the residual of the second column with respect to the corresponding Bouguer anomaly. The fourth column shows a residual plot of the low end member. The parameter lowered in the end member is the one in the first column, while the other parameter is kept constant. The last column shows the corresponding high end member.

C

Software Settings

Each run of the software requires a settings file to provide a variety of inputs. An example settings file is shown in Figure C.1. Most values have been treated in Chapter 3, but a few need more explanation.

The parameter **verbose** is a binary value that determines whether plots are shown during the runtime of the software. **synthesis_nmax** is the maximum spherical harmonic degree used when a spherical harmonic signal is converted to the spatial domain. **comp_height** is the altitude at which the analysis takes place, with zero being the surface of the planet. **C20** is a binary value that determines whether the C20 spherical harmonic coefficient is set to zero (0) or not (1). **multi** is a binary parameter that should be 1 when multiple windows are being combined in the run, and 0 otherwise.

The parameters **E**, **nu**, **Te**, **base_compensation_depth**, **rho_m**, and **rho_c** are the physical parameters of the lithosphere which can be varied in this software. **mask** is a string containing the filepath of an arbitrary window, generated with the localization functions presented in Chapter 3.

```
base_compensation_depth        = -400
Te                             = 40000
rho_c                          = 2900
SH_bounds                      = [2 20]
verbose                        = 0
topo_filepath                  = Data/gmt_files/Topography_only.gmt
layer_thickness                = 25
rho_m                          = 3500
GM_mars                        = 4.2621e+13
R_mars                         = 3396200.0
synthesis_nmax                 = 179
LatLim                         = [-89.5 89.5 1]
LonLim                         = [-180 179 1]
comp_height                    = 0
C20                            = 0
mask                           = Data/Masks/None.mat
E                              = 1e11
nu                             = 0.25
g_mars                         = 3.711
multi                          = 0
```

Figure C.1: An example settings file for the software used in this study.

D

Extended Regional Results

Hellas Basin

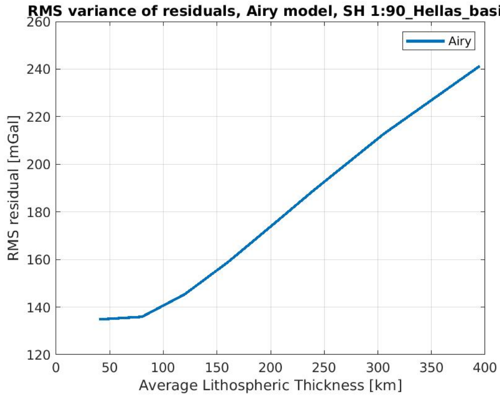

Figure D.1: RMS variance of the Airy model residuals with a changing average lithospheric thickness for a spectral range of 1:90.

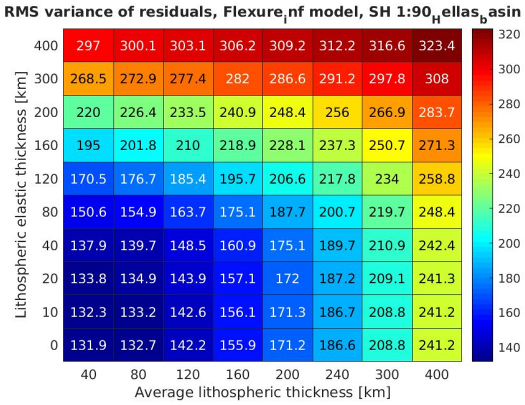

Figure D.2: RMS variance of the infinite plate model residuals with a changing average lithospheric thickness and lithospheric elastic thickness, for a spectral range of 1:90

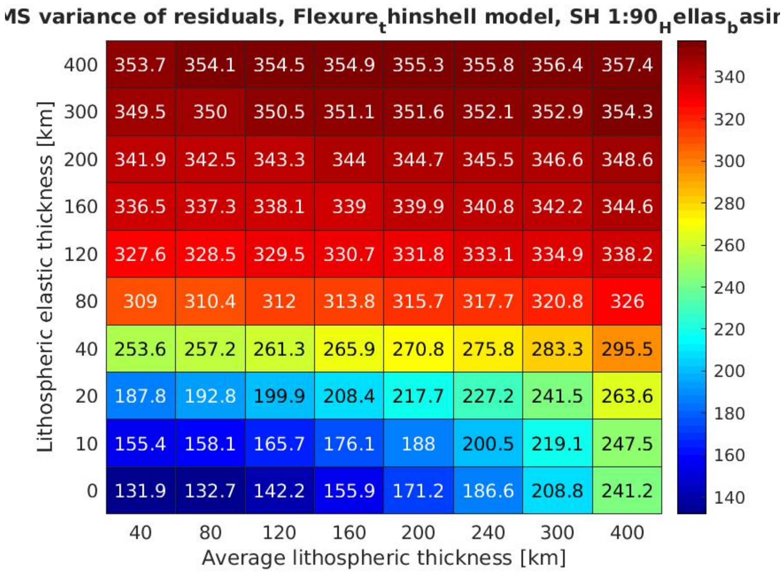

Figure D.3: RMS variance of the thinshell model residuals with a changing average lithospheric thickness and lithospheric elastic thickness, for a spectral range of 1:90

Figure D.4: Central point residual variance of the Airy model residuals with a changing average lithospheric thickness for a spectral range of 1:90.

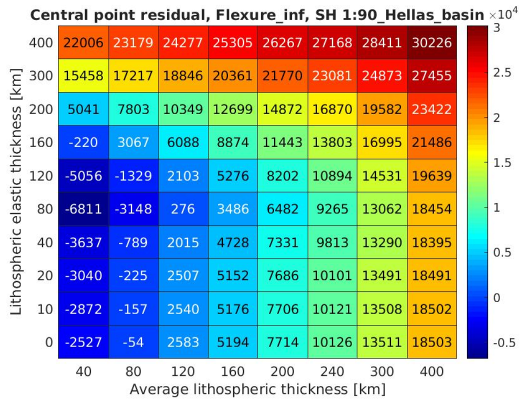

Figure D.5: Central point residual variance of the infinite plate model residuals with a changing average lithospheric thickness and lithospheric elastic thickness, for a spectral range of 1:90

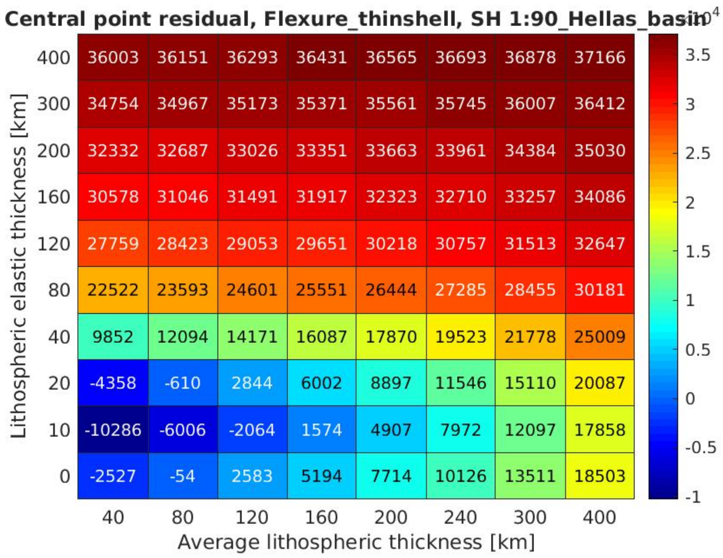

Figure D.6: Central point residual variance of the thinshell model residuals with a changing average lithospheric thickness and lithospheric elastic thickness, for a spectral range of 1:90

Argyre Basin

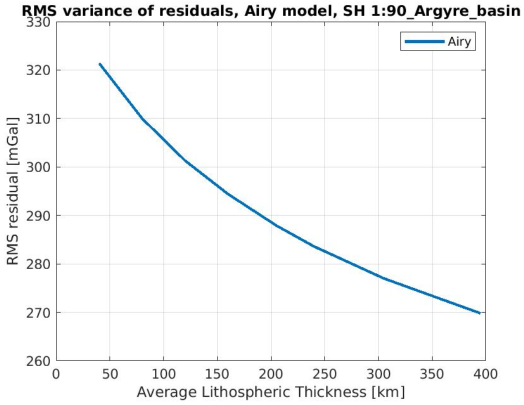

Figure D.7: RMS variance of the Airy model residuals with a changing average lithospheric thickness for a spectral range of 1:90.

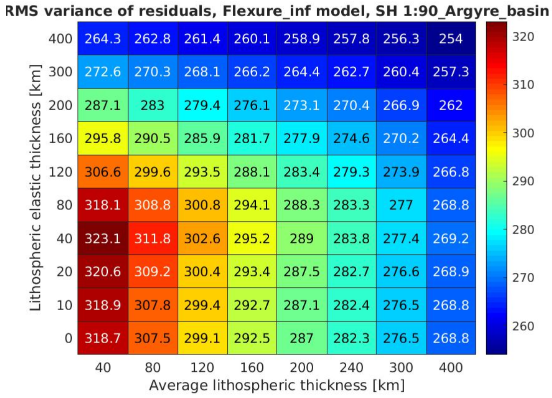

Figure D.8: RMS variance of the infinite plate model residuals with a changing average lithospheric thickness and lithospheric elastic thickness, for a spectral range of 1:90

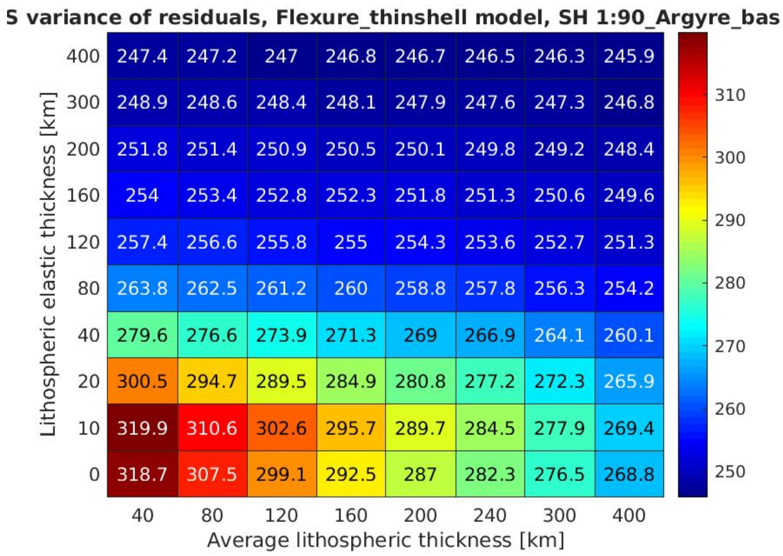

Figure D.9: RMS variance of the thinshell model residuals with a changing average lithospheric thickness and lithospheric elastic thickness, for a spectral range of 1:90

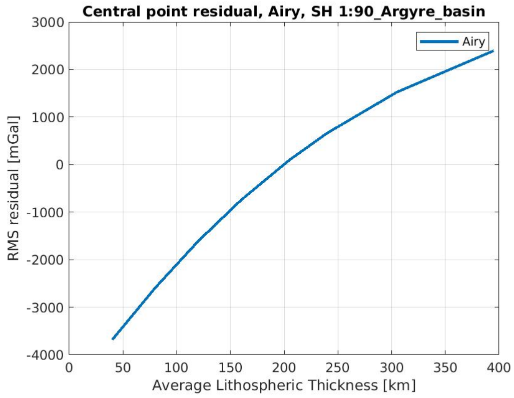

Figure D.10: Central point residual variance of the Airy model residuals with a changing average lithospheric thickness for a spectral range of 1:90.

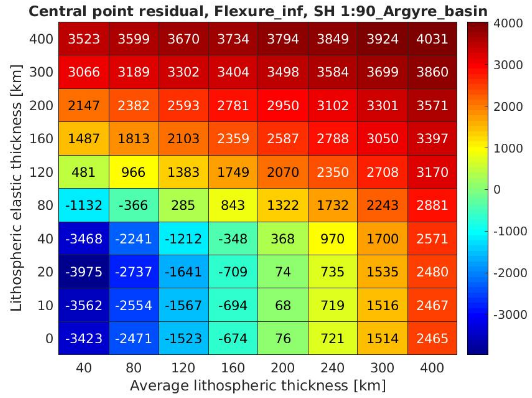

Figure D.11: Central point residual variance of the infinite plate model residuals with a changing average lithospheric thickness and lithospheric elastic thickness, for a spectral range of 1:90

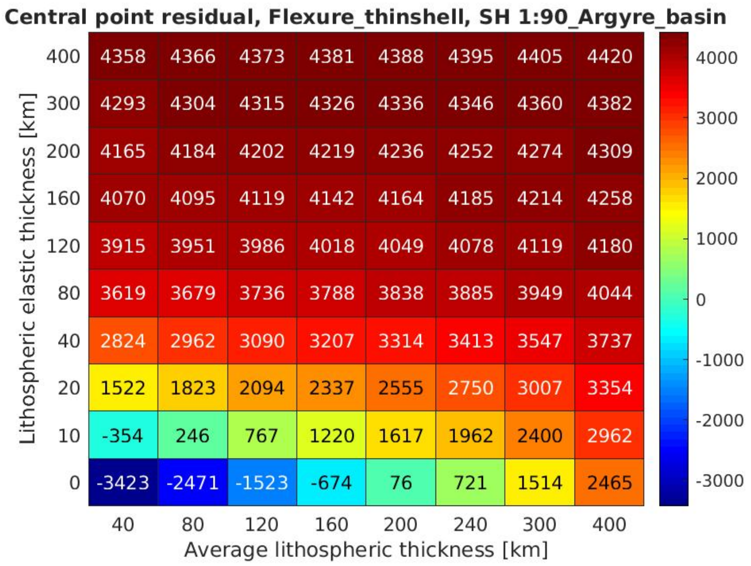

Figure D.12: Central point residual variance of the thinshell model residuals with a changing average lithospheric thickness and lithospheric elastic thickness, for a spectral range of 1:90

Isidis Planitia

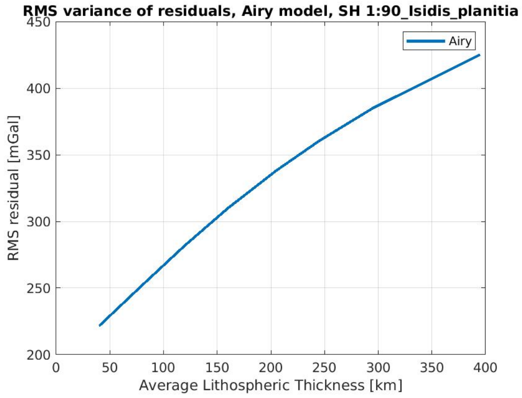

Figure D.13: RMS variance of the Airy model residuals with a changing average lithospheric thickness for a spectral range of 1:90.

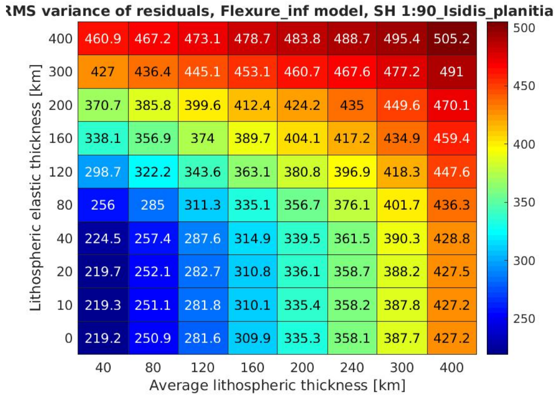

Figure D.14: RMS variance of the infinite plate model residuals with a changing average lithospheric thickness and lithospheric elastic thickness, for a spectral range of 1:90

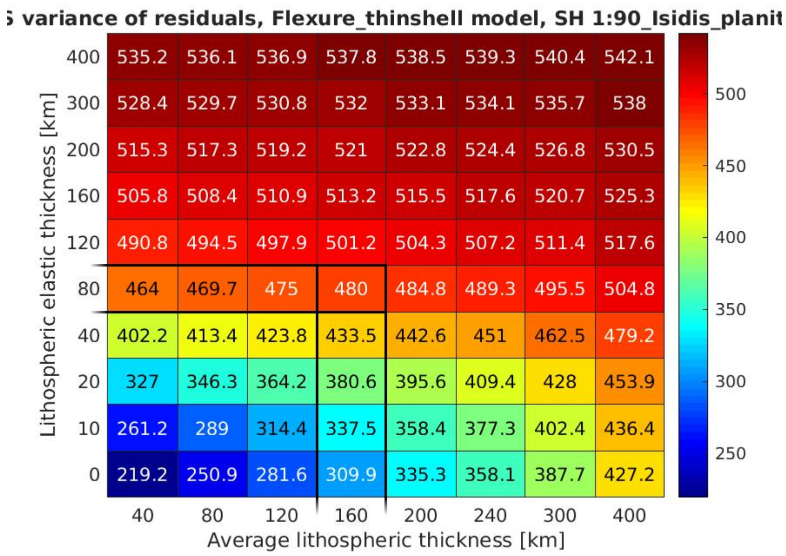

Figure D.15: RMS variance of the thinshell model residuals with a changing average lithospheric thickness and lithospheric elastic thickness, for a spectral range of 1:90

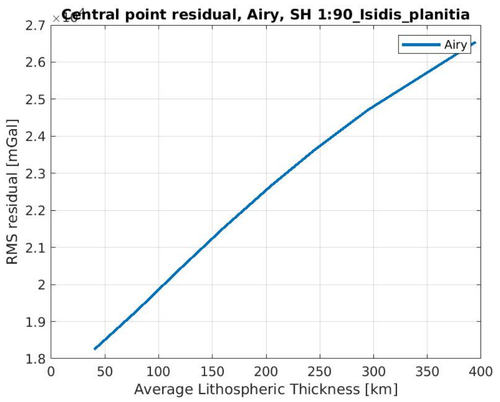

Figure D.16: Central point residual variance of the Airy model residuals with a changing average lithospheric thickness for a spectral range of 1:90.

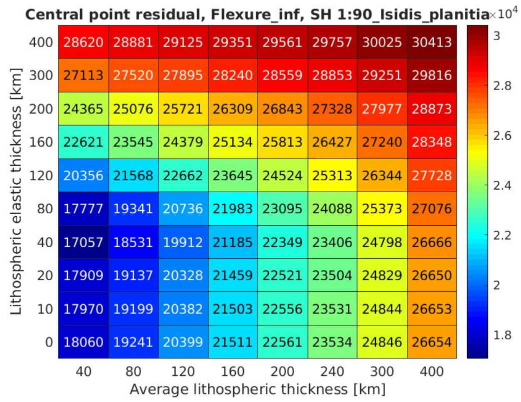

Figure D.17: Central point residual variance of the infinite plate model residuals with a changing average lithospheric thickness and lithospheric elastic thickness, for a spectral range of 1:90

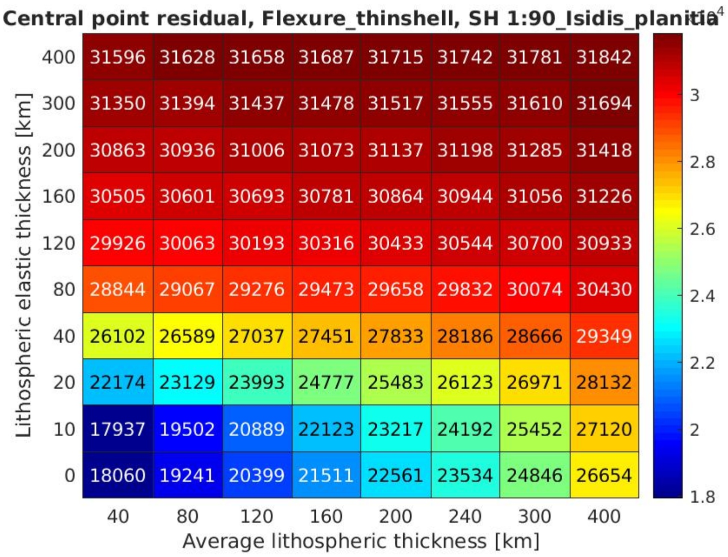

Figure D.18: Central point residual variance of the thinshell model residuals with a changing average lithospheric thickness and lithospheric elastic thickness, for a spectral range of 1:90

Utopia Planitia

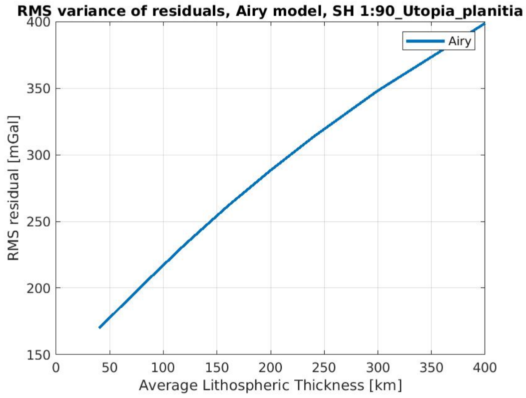

Figure D.19: RMS variance of the Airy model residuals with a changing average lithospheric thickness for a spectral range of 1:90.

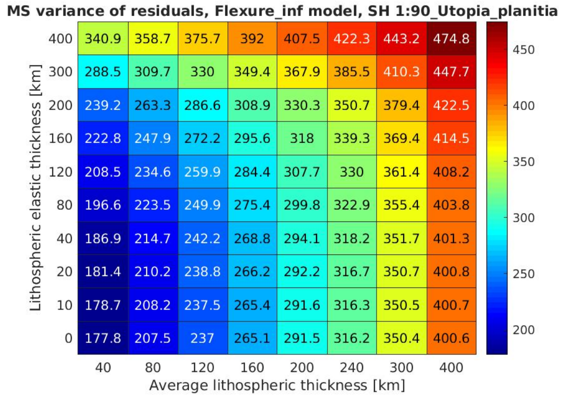

Figure D.20: RMS variance of the infinite plate model residuals with a changing average lithospheric thickness and lithospheric elastic thickness, for a spectral range of 1:90

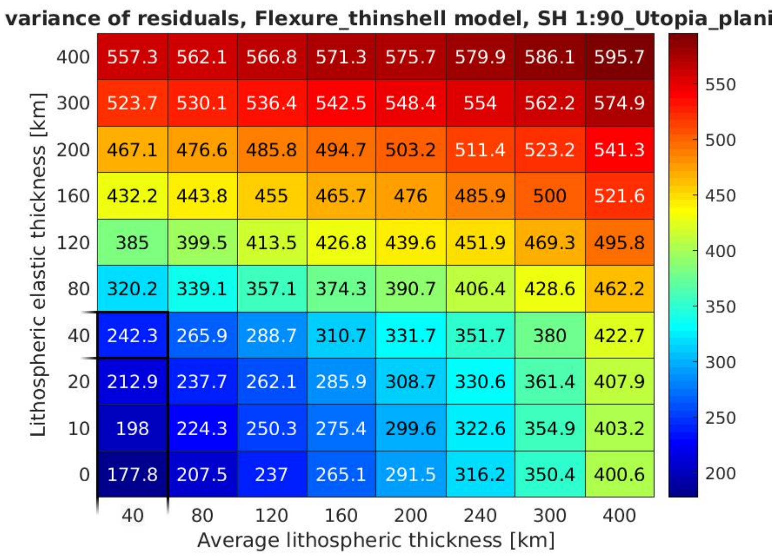

Figure D.21: RMS variance of the thinshell model residuals with a changing average lithospheric thickness and lithospheric elastic thickness, for a spectral range of 1:90

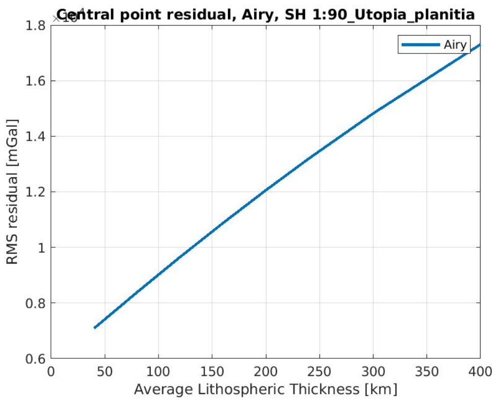

Figure D.22: Center point residual variance of the Airy model residuals with a changing average lithospheric thickness for a spectral range of 1:90.

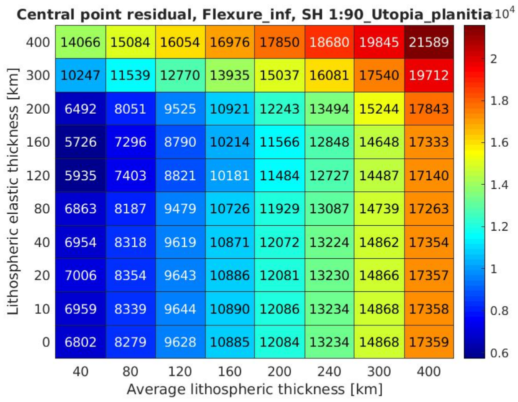

Figure D.23: Center point residual variance of the infinite plate model residuals with a changing average lithospheric thickness and lithospheric elastic thickness, for a spectral range of 1:90

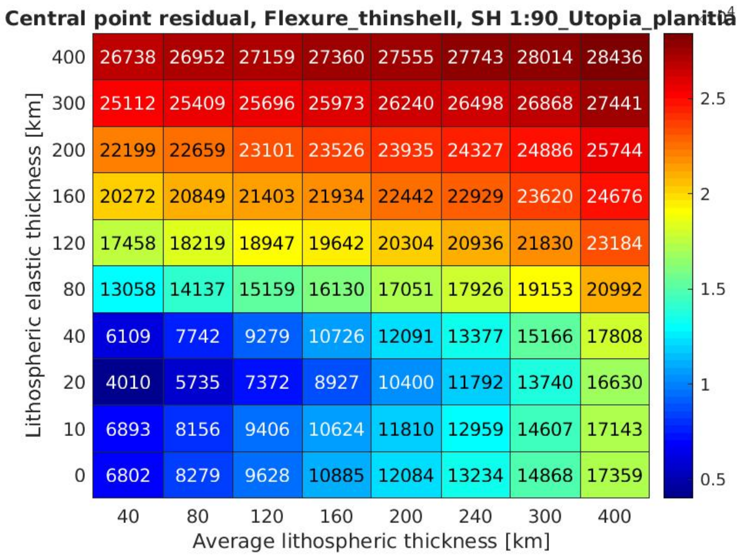

Figure D.24: Center point residual variance of the thinshell model residuals with a changing average lithospheric thickness and lithospheric elastic thickness, for a spectral range of 1:90

Elysium Mons

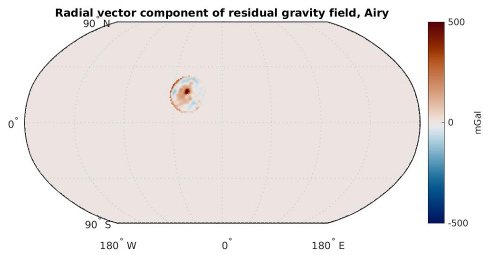

Figure D.25: Residuals of an Airy model with an average lithospheric thickness of 40km, SH1:90

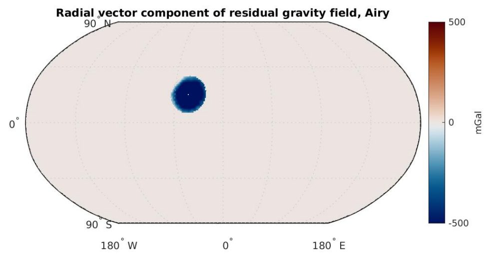

Figure D.26: Residuals of an Airy model with an average lithospheric thickness of 400km, SH1:90

1:90

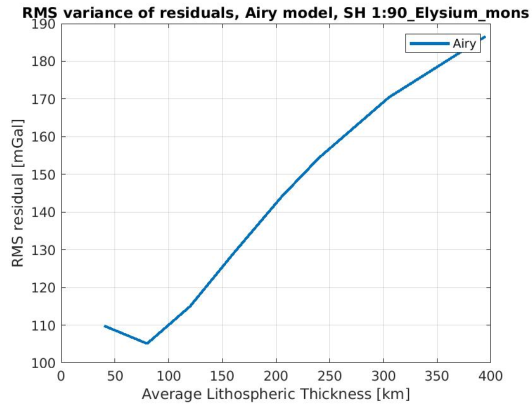

Figure D.27: RMS variance of the Airy model residuals with a changing average lithospheric thickness for a spectral range of 1:90.

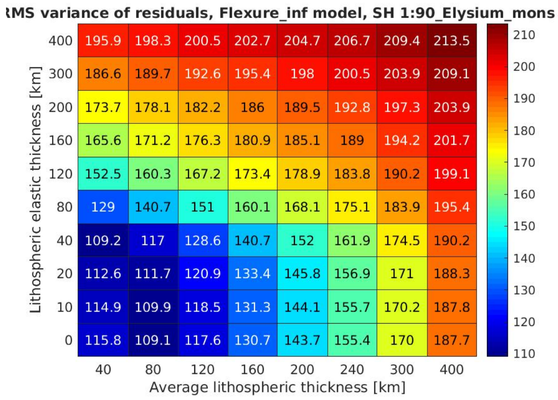

Figure D.28: RMS variance of the infinite plate model residuals with a changing average lithospheric thickness and lithospheric elastic thickness, for a spectral range of 1:90

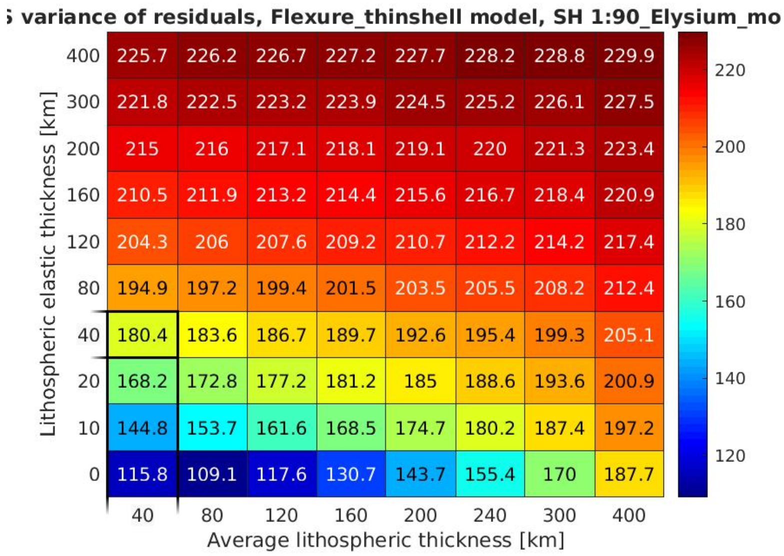

Figure D.29: RMS variance of the thinshell model residuals with a changing average lithospheric thickness and lithospheric elastic thickness, for a spectral range of 1:90

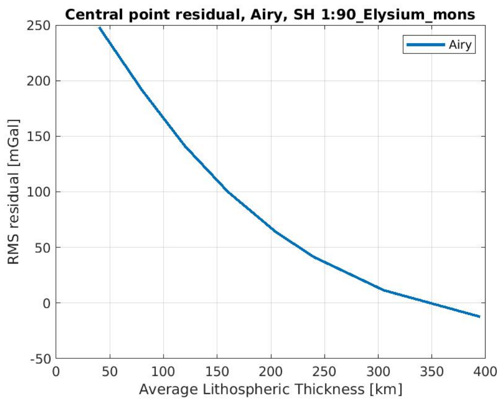

Figure D.30: Center point residual variance of the Airy model residuals with a changing average lithospheric thickness for a spectral range of 1:90.

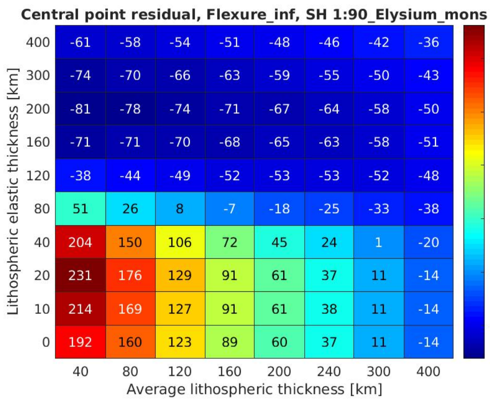

Figure D.31: Center point residual variance of the infinite plate model residuals with a changing average lithospheric thickness and lithospheric elastic thickness, for a spectral range of 1:90

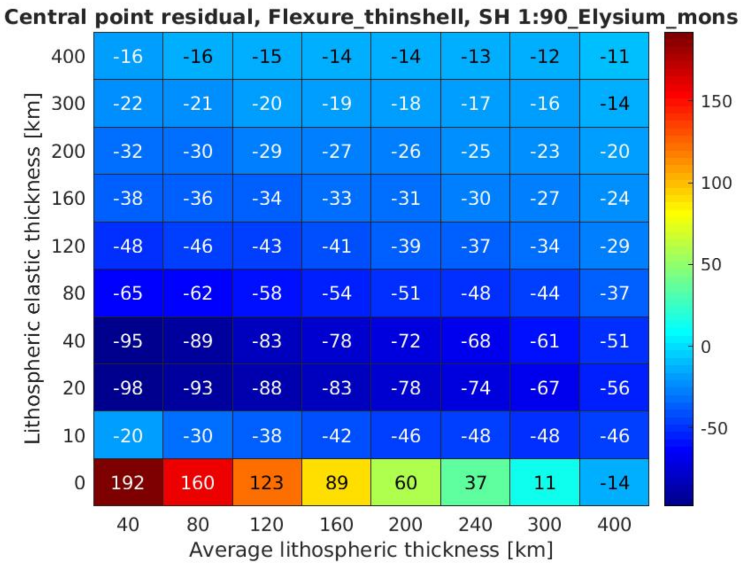

Figure D.32: Center point residual variance of the thinshell model residuals with a changing average lithospheric thickness and lithospheric elastic thickness, for a spectral range of 1:90

Olympus Mons

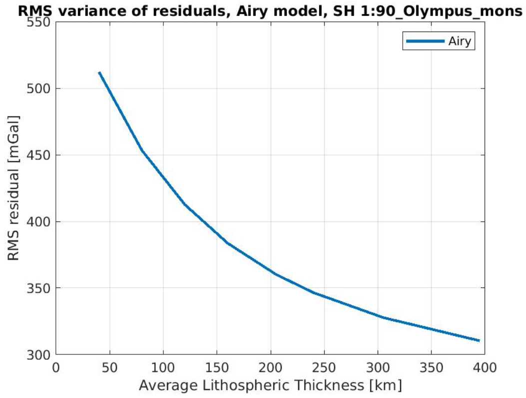

Figure D.33: RMS variance of the Airy model residuals with a changing average lithospheric thickness for a spectral range of 1:90.

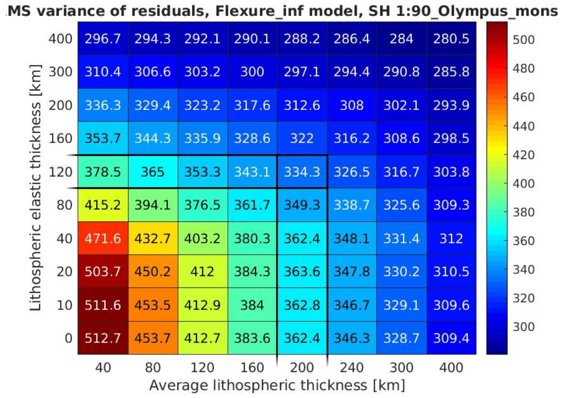

Figure D.34: RMS variance of the infinite plate model residuals with a changing average lithospheric thickness and lithospheric elastic thickness, for a spectral range of 1:90

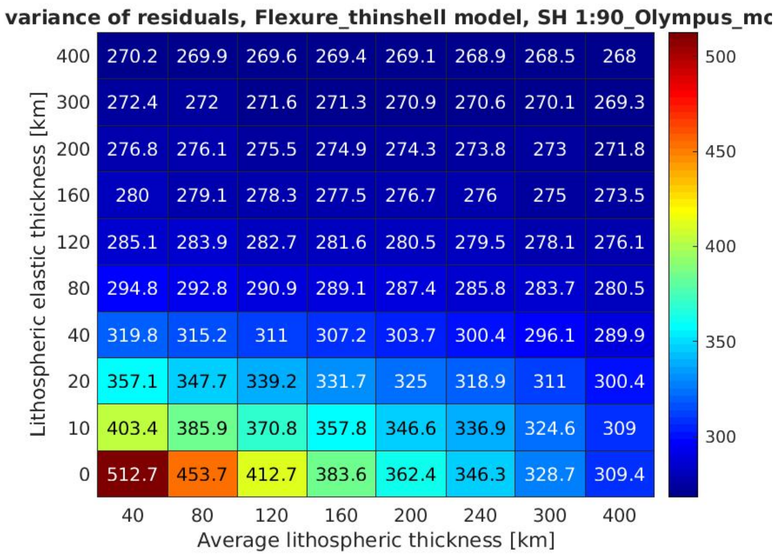

Figure D.35: RMS variance of the thinshell model residuals with a changing average lithospheric thickness and lithospheric elastic thickness, for a spectral range of 1:90

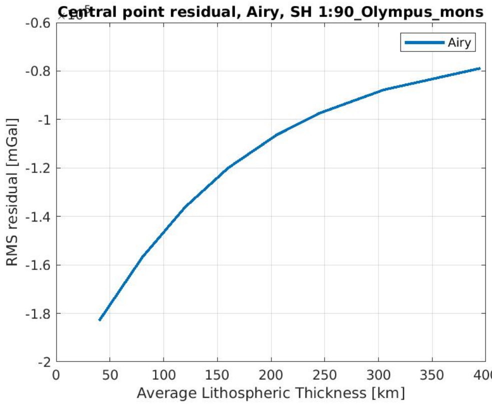

Figure D.36: Center point residual variance of the Airy model residuals with a changing average lithospheric thickness for a spectral range of 1:90.

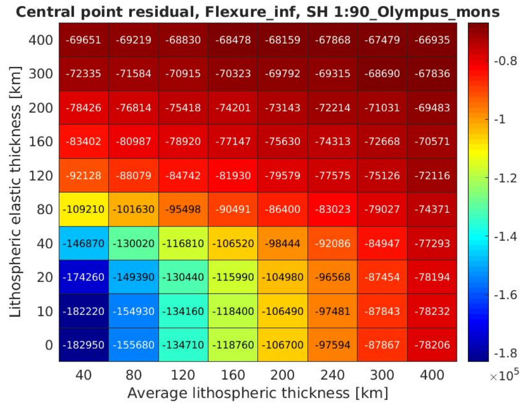

Figure D.37: Center point residual variance of the infinite plate model residuals with a changing average lithospheric thickness and lithospheric elastic thickness, for a spectral range of 1:90

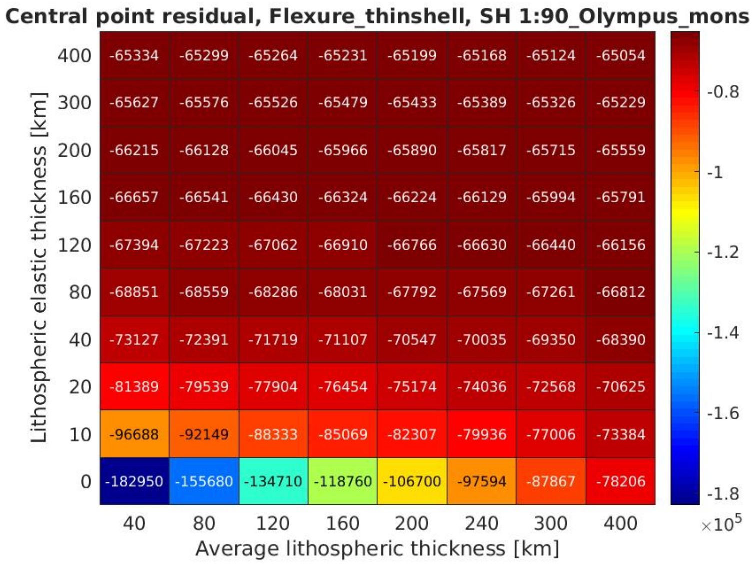

Figure D.38: Center point residual variance of the thinshell model residuals with a changing average lithospheric thickness and lithospheric elastic thickness, for a spectral range of 1:90

Alba Mons

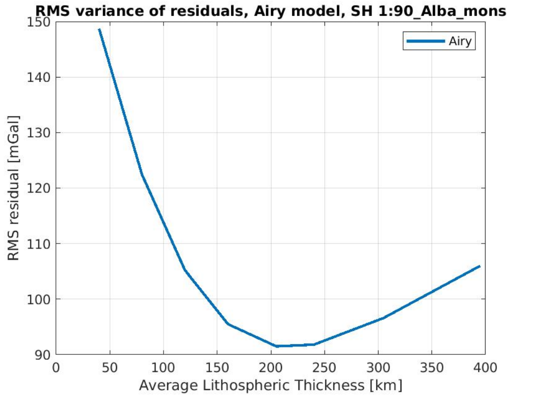

Figure D.39: RMS variance of the Airy model residuals with a changing average lithospheric thickness for a spectral range of 1:90.

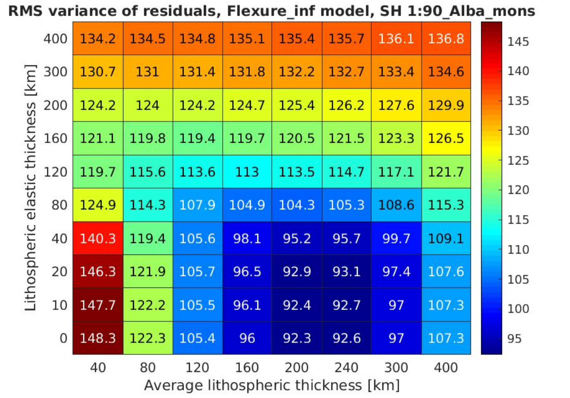

Figure D.40: RMS variance of the infinite plate model residuals with a changing average lithospheric thickness and lithospheric elastic thickness, for a spectral range of 1:90

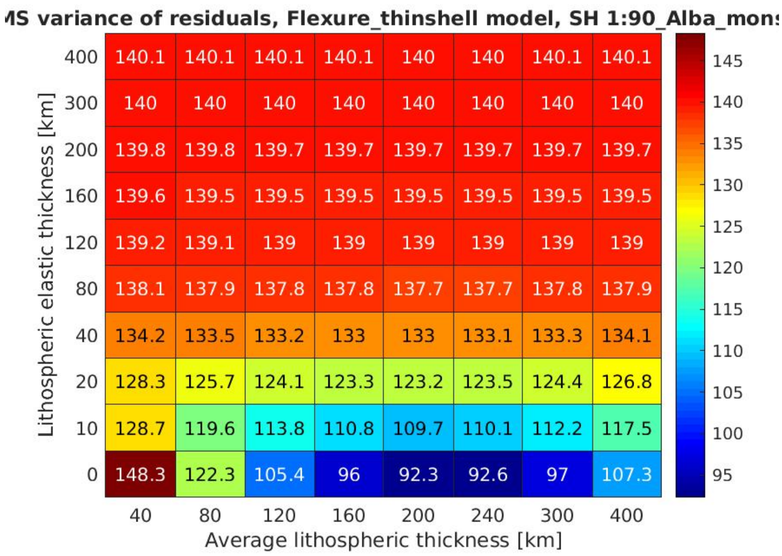

Figure D.41: RMS variance of the thinshell model residuals with a changing average lithospheric thickness and lithospheric elastic thickness, for a spectral range of 1:90

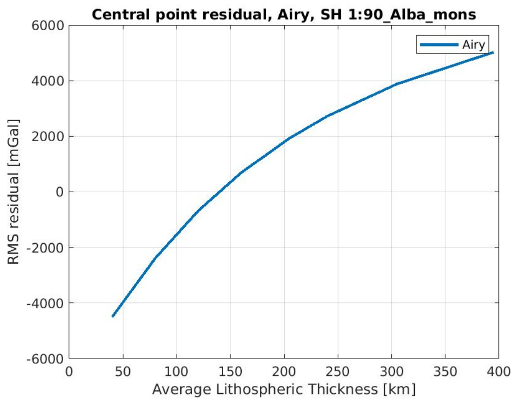

Figure D.42: Center point residual variance of the Airy model residuals with a changing average lithospheric thickness for a spectral range of 1:90.

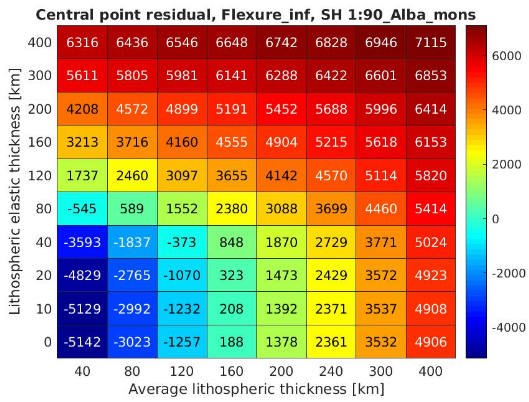

Figure D.43: Center point residual variance of the infinite plate model residuals with a changing average lithospheric thickness and lithospheric elastic thickness, for a spectral range of 1:90

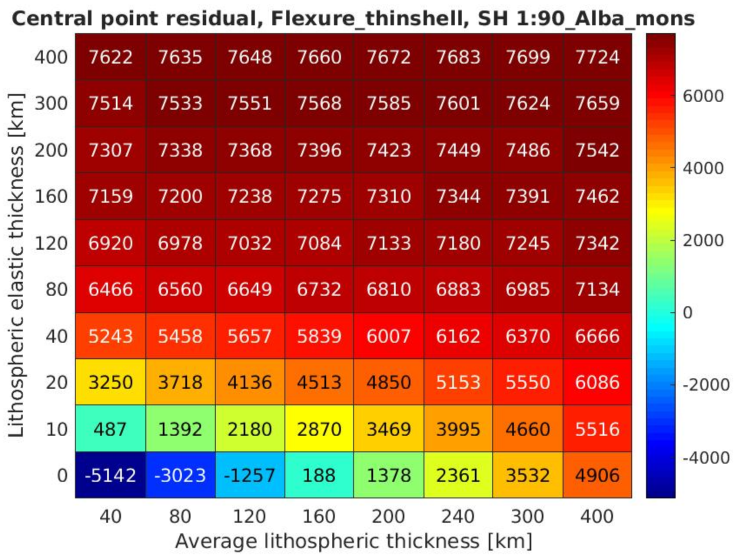

Figure D.44: Center point residual variance of the thinshell model residuals with a changing average lithospheric thickness and lithospheric elastic thickness, for a spectral range of 1:90

Tharsis

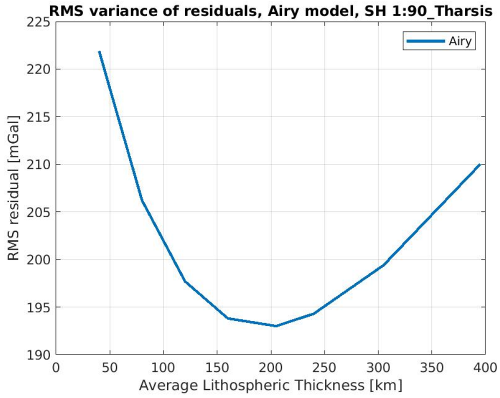

Figure D.45: RMS variance of the Airy model residuals with a changing average lithospheric thickness for a spectral range of 1:90.

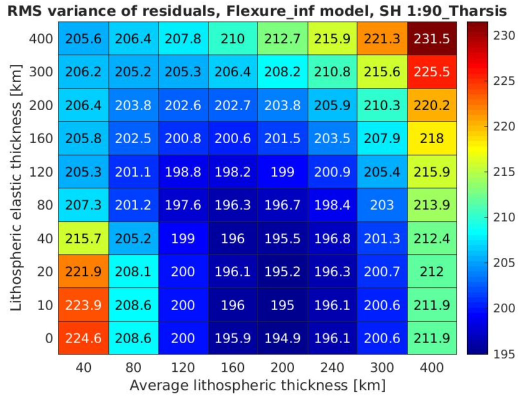

Figure D.46: RMS variance of the infinite plate model residuals with a changing average lithospheric thickness and lithospheric elastic thickness, for a spectral range of 1:90

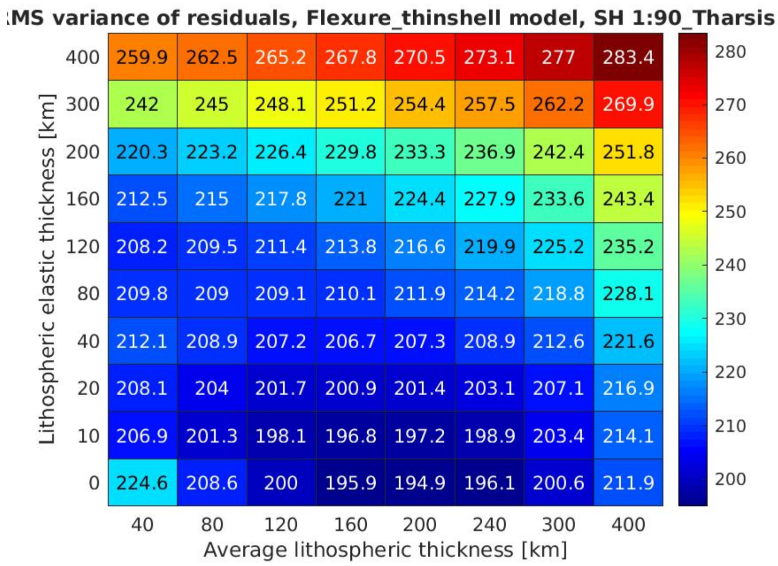

Figure D.47: RMS variance of the thinshell model residuals with a changing average lithospheric thickness and lithospheric elastic thickness, for a spectral range of 1:90

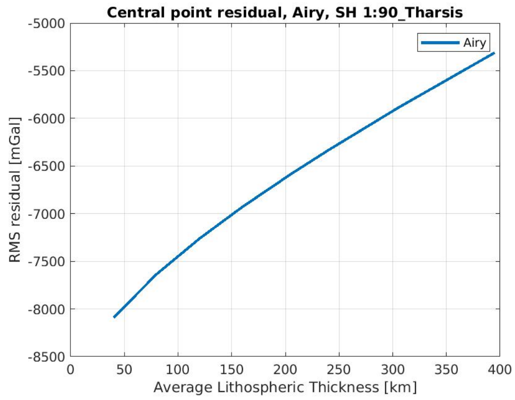

Figure D.48: Center point residual variance of the Airy model residuals with a changing average lithospheric thickness for a spectral range of 1:90.

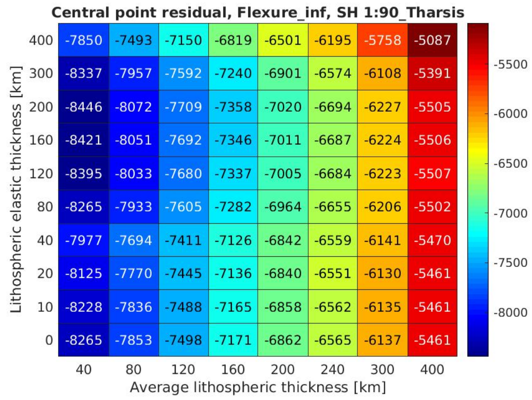

Figure D.49: Center point residual variance of the infinite plate model residuals with a changing average lithospheric thickness and lithospheric elastic thickness, for a spectral range of 1:90

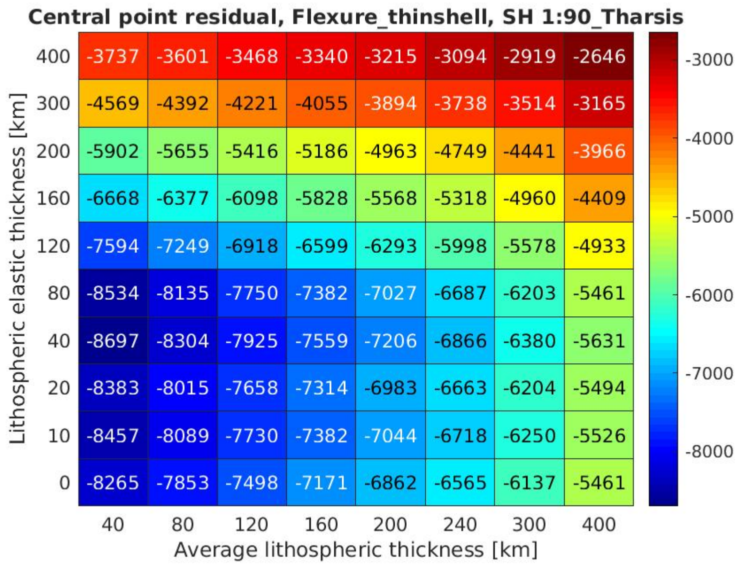

Figure D.50: Center point residual variance of the thinshell model residuals with a changing average lithospheric thickness and lithospheric elastic thickness, for a spectral range of 1:90

Valles Marineris

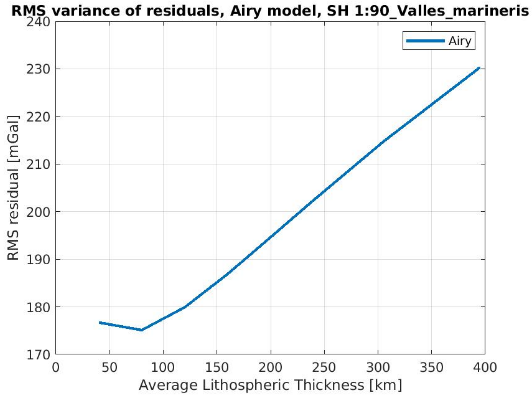

Figure D.51: RMS variance of the Airy model residuals with a changing average lithospheric thickness for a spectral range of 1:90.

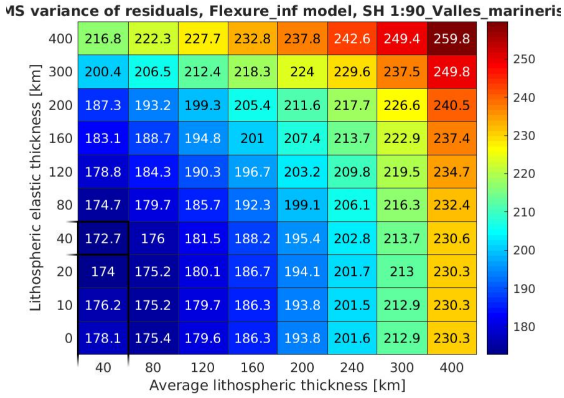

Figure D.52: RMS variance of the infinite plate model residuals with a changing average lithospheric thickness and lithospheric elastic thickness, for a spectral range of 1:90

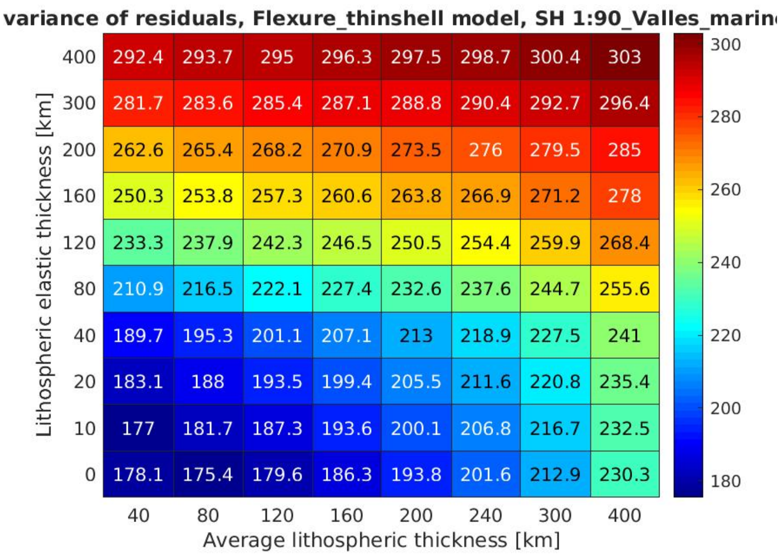

Figure D.53: RMS variance of the thinshell model residuals with a changing average lithospheric thickness and lithospheric elastic thickness, for a spectral range of 1:90

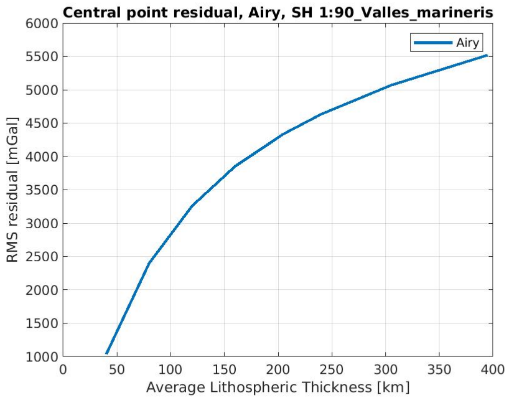

Figure D.54: Center point residual variance of the Airy model residuals with a changing average lithospheric thickness for a spectral range of 1:90.

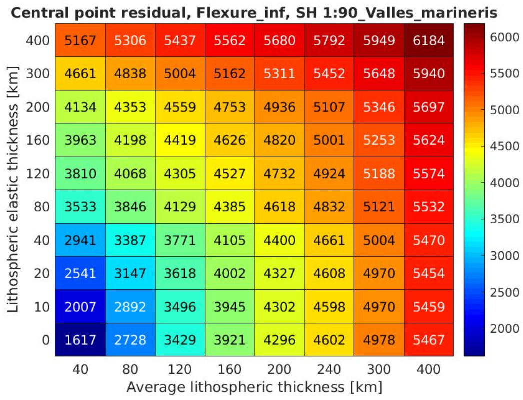

Figure D.55: Center point residual variance of the infinite plate model residuals with a changing average lithospheric thickness and lithospheric elastic thickness, for a spectral range of 1:90

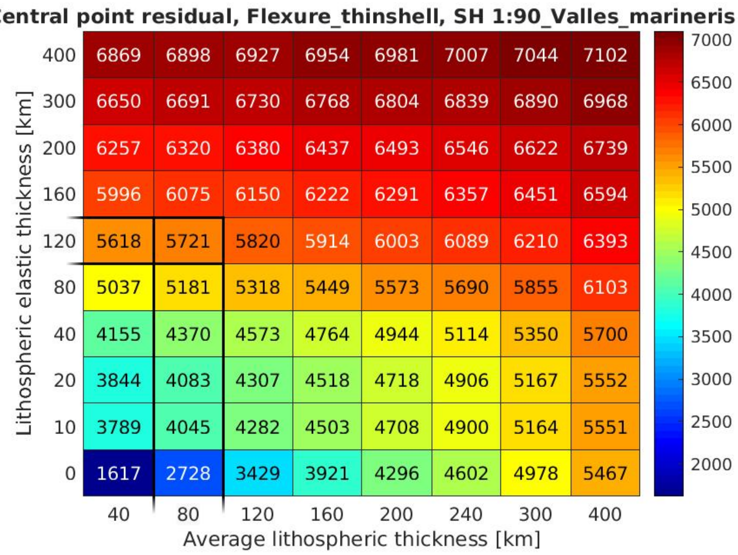

Figure D.56: Center point residual variance of the thinshell model residuals with a changing average lithospheric thickness and lithospheric elastic thickness, for a spectral range of 1:90